Inaugural - Dissertation

zur

Erlangung der Doktorwürde

der

Naturwissenschaftlich-Mathematischen Gesamtfakultät

der

Ruprecht-Karls-Universität

Heidelberg

vorgelegt von

Arash Rashidi, MSc. Energy Systems

aus

Shiraz, Iran

Tag der mündlichen Prüfung: 4. Februar 2011

CFD Simulation of Biomass Gasification Using Detailed Chemistry

Gutachter: Prof. Dr. Uwe Riedel

PD Dr. Nikolaus Dahmen

Abstract

The use of biomass as a CO_2-neutral renewable fuel and the only carbon containing renewable energy source is becoming more important due to the decreasing resources of fossil fuels and their effect on global warming. The projections made for the Renewable Energy Road Map [1] suggested that in the EU, the use of biomass can be expected to double, to contribute around half of the total effort for reaching the 20 % renewable energy target in 2020 [2]. To achieve this goal, efficient processes to convert biomass are required.

At the Karlsruhe Institute of Technology (KIT), Germany, a two-stage process called bioliq® [3], for the conversion of biomass into synthetic fuel, is being developed. In this process, straw or other abundant lignocellulosic agricultural by-products are converted to syngas through fast pyrolysis and subsequent entrained flow gasification. After gas cleaning and conditioning, the syngas is converted into different chemicals via known processes such as direct methanol synthesis or Fischer-Tropsch synthesis.

The prime goal of this thesis was the modeling and simulation of the gasification of biomass-based pyrolysis oil-char slurries in an entrained flow gasifier, which is an important step of the bioliq® process. Computational Fluid Dynamics (CFD), as a powerful tool for modeling and simulation of fluid flow processes, was utilized in this thesis.

A lab scale entrained flow gasifier, located at KIT, was simulated using the CFD code ANSYS FLUENT 12.0. Due to the turbulent nature of the flow, the realizable k-ε model was used to model the turbulence. The discrete phase model (DPM) was employed to describe the fluid phase, consisting of char particles suspended in

ethylene glycol. Ethylene glycol served as non-toxic model fuel for pyrolysis oil, mainly because of its similar C/H/O-ratio and its similar physical properties to biomass derived liquid pyrolysis products.

A detailed reaction mechanism for high temperature oxidation of ethylene glycol was implemented in the CFD code. The mechanism comprised of 43 chemical species and 629 elementary reactions. The use of detailed chemistry enables one to have a deeper insight into the gasification process. Turbulence-chemistry interactions were modeled with the eddy dissipation concept (EDC). The in-situ adaptive tabulation (ISAT) procedure was employed to dynamically tabulate the chemistry mappings and reduce computer time for the simulation. The effect of the thermal radiation was taken into account by using the discrete ordinates model (DOM). The radiative properties of the gas were described with the weighted sum of gray gases model (WSGGM).

The simulation results were compared with the experimental measurements wherever possible, with good agreement. The simulations depicted the importance of the recirculation zone in entrained flow gasification. Furthermore, the main reaction path of ethylene glycol gasification could be observed and analyzed.

In order to study the effect of boundary conditions on the gasification process, a series of simulations were done to perform sensitivity analysis. Four parameters were varied, namely: oxidizer and fuel inlet temperatures, the oxidizer composition, the air-fuel ratio and the operating pressure of the gasifier. Effects of the parameter variations on the gasification efficiency and the composition of the product gas were studied. Three different chemistry models (i.e. equilibrium chemistry, flamelet model and EDC) were studied in this thesis. Their relative advantages and disadvantages for the simulation of gasification processes were examined. The EDC model proved to be the better choice for entrained flow gasifiers with recirculation zones.

The slurry gasification simulations were performed to study the effects of the mass fractions of the char particles on the process. With the aid of the detailed chemistry model, sub-processes could be analyzed and suggestions for the improvement could be made.

The simulations performed in this work help to better understand the gasification process inside entrained flow gasifiers and considerably reduce the number of experiments needed to characterize the system. The simulations produced spatial and temporal profiles of different system variables that are sometimes impossible to measure or are accessible only by expensive experiments. However, more experimental

measurements help to validate and optimize the CFD model. The sensitivity analyses performed in this study are considered as a basis to find optimized operating conditions and assist the successful scale-up of entrained flow gasifiers.

Zusammenfassung

Die Nutzung von Biomasse als CO_2-neutraler Energieträger und einzige kohlenstoffhaltige erneubare Energiequelle, gewinnt wegen schwindenden fossilen Energieträgern und deren Einfluss auf den Klimawandel zunehmend an Bedeutung. Der Fahrplan für erneubare Energien [1] enthält das Ziel, bis zum Jahr 2020 den Anteil erneuerbarer Energien am Gesamtenergieverbrauch in der EU auf 20 % zu steigern. Der Anteil von Biomasse am Energiemix soll sich im Rahmen dieses Plans verdoppeln [2]. Hierfür sind effiziente Prozessen zur Umwandlung von Biomasse erforderlich.

Am Karlsruher Institut für Technologie (KIT) wurde das zweistufige bioliq®- Verfahren konzipiert [3], in dem aus trockener Restbiomasse durch dezenterale Schnellpyrolyse und zenterale Flugstrom-Druckvergasung Synthesegas erzeugt wird. Aus dem gereinigten und konditionierten Synthesegas können z.B. durch Fischer-Tropsch- oder Methanol-Synthese neben Synthesekraftstoffen auch eine Vielzahl von chemischen Grundstoffen erzeugt werden.

Schwerpunkt dieser Arbeit ist die Modellierung und numerische Simulation des Vergasungsprozesses von biomassestämmigen Öl-Koks-Slurrys in einem Flugstromvergaser nach dem bioliq®-Verfahren. Numerische Strömungssimulation (Computational Fluid Dynamics - CFD) wurde im Rahmen dieser Arbeit als eine effiziente Methode zur Modellierung reaktiver Strömungen verwendet.

Die Simulation eines Versuchsreaktors des KIT wird in der vorliegender Arbeit mit der CFD-Simulationssoftware ANSYS FLUENT 12.0 durchgeführt. Für die Beschreibung des turbulenten Strömungsfeldes wird das "realizable" k-ε-Modell verwendet. Zur Modellierung der diskreten Phase (flüssiges Ethylenglykol und Kokspar-

tikel) wurde das Discrete-Phase-Modell (DPM) verwendet. Ethylenglykol diente aufgrund vergleichbarer physikalischer Eigenschaften sowie ähnlichem C/H/O-Verhältnis als Modellsubstanz für Pyrolyseöl.

Im Rahmen dieser Arbeit wurde ein detaillierter Reaktionsmechanismus zur Beschreibung der Oxidationsreaktionen von Ethylenglykol verwendet, der aus 43 Spezies und 629 Elementarreaktionen besteht. Die Verwendung eines detaillierten Reaktionsmechanismus ermöglicht die Einsicht in chemische Vorgänge der Vergasung. Für die Kopplung von detaillierter Reaktionskinetik und Turbulenzeffekten wird das Eddy Dissipation Concept (EDC) Modell verwendet. Die Verwendung des In-Situ Adaptive Tabulation (ISAT) Ansatzes zur Tabellierung des Reaktionsforschritts reduziert die Rechenzeit deutlich. Das Modell der Diskreten Ordinaten (DOM) wurde als thermisches Strahlungsmodell verwendet. Die Strahlungseigenschaften des Gases werden mittels dem *Weighted Sum of Gray Gases* Modell (WSGGM) berechnet.

Vergleiche von simulierten und experimentellen Werten (sofern möglich) zeigten akzeptable Übereinstimmungen. Die Simulationen haben zusätzlich die Wichtigkeit von Rezirkulationszonen in der Flugstromvergasung dargestellt. Darüber hinaus wurden die haupt Reaktionspfade der Ethylenglykolvergasung veranschaulicht.

Um die Auswirkungen der Randbedingungen auf die Zusammensetzung des Synthesegases und den Vergasungswirkungsgrad zu untersuchen, wurden Parameterstudien mit verschiedenen Randbedingungen durchgeführt. Vier Parameter nämlich die Luft- und Brennstoffeintrittstemperaturen, der Sauerstoffgehalt des Zerstäubungsmediums, die Luftzahl und der Vergaserdruck wurden variiert. Außerdem wurden drei unterschiedliche Chemie-Modelle (Gleichgewichts-Modell, Flamelet-Modell und EDC-Modell) untersucht und deren Vor- und Nachteile miteinander verglichen. Das EDC Modell erwies sich für die Modellierung von Vergasungsvorgängen in Flugstromvergasern mit Rezirkulationszonen als gut geeignet.

Die CFD-Simulationen der Slurryvergasung wurde durchgeführt, um den Einfluss von Massenanteilen der Kokspartikel in dem Slurrygemisch zu untersuchen. Mit Hilfe der verwendeten detaillierten Chemie konnten einige Teilprozesse analysiert werden und Verbesserungsvorschläge gemacht werden.

Durch die Computersimulationen lässt sich die Zahl von zeit- und kostenintensiven Experimenten reduzieren. Zudem erhält man eine zeitliche und/oder örtliche Auflösung der Teilprozesse des Gesamtsystems und kann Prozessgrößen charakterisieren, die mit experimentellen Methoden nicht, oder nur unter erheblichen Aufwand, zu bestimmen sind. Um jedoch die Verlässlichkeit der CFD-Simulationen zu gewährleisten, müssen jedoch auch mehr Validierungsexperimente durchgeführt werden. Die

in dieser Arbeit durchgeführten Sensitivitätsanalysen können als eine Basis für die Festlegung von optimierten Betriebsbedingungen verstanden werden und können bei der Skalierung des Flugstromvergasers unterstützend eingesetzt werden.

Acknowledgement

A dissertation does not just appear out of nowhere, and although it is supposed to be a contribution by one person for a PhD, there are still a lot of people behind it who have helped and inspired me during my doctoral study.

I would like to express my heartfelt gratitude to my supervisor Prof. Dr. Uwe Riedel for letting me do my PhD in his group, for creating the research environment, and for supproting me both financially and scientifically during this period. I would like to thank my co-advisor Dr. Nicolaus Dahmen for his guidance and efforts in this project.

The current thesis is a part of the collaborative project *Synthesegaserzeugung durch Flugstromvergasung von Öl/Koks-Slurrys aus Biomasse - Grundlagen zur Prozessoptimierung* supported by the German Federal Ministry of Education and Research (BMBF). I would like to acknowledge them for their support under Grant 03SF0320D. I also thank the project partners in Karlsruhe Institute of Technology (KIT) for providing relevant data.

Many thanks go to my friends and colleagues in *reactive flows* group in IWR who made my time in Heidelberg joyful. Special thank goes to Dr. Simon Hafner for all the technical and nontechnical discussions we had, his teamwork as well as his helps in editing my German texts. I would also like to thank Ingrid Hellwig for her perfect administration helps and Joachim Simon and Jürgen Moldenhauer for providing IT assistance wherever required.

My deepest gratitude goes to my family for their unflagging love and support throughout my life. My parents, Soghra Gholami and Ahmad Rashidi, raised me up with a love for science and supported me unconditionally in all my pursuits. They

deserve far more credit than I can ever give them. My sister, Afsoon Rashidi, was always there with her encouragement and care. Thank you all!

Last but not least, a very special thank to my lovely Mareike Heitner for her unlimited support and delicious cakes, without which I could not find enough power to work. Danke!

Arash Rashidi

Heidelberg, December 2010

Contents

1. Introduction

The use of biomass as a CO_2-neutral renewable fuel and the only carbon containing renewable energy source is becoming more important due to the decreasing resources of fossil fuels and their effect on global warming. Hence, it is expected that biomass substitutes gradually a fraction of fossil fuels. In the EU, around 5 % of final energy consumption is from bio-energy. The projections made for the Renewable Energy Road Map [1] suggested that the use of biomass can be expected to double, to contribute around half of the total effort for reaching the 20 % renewable energy target in 2020 [2]. Efficient biomass conversion processes are required to achieve this goal. Biomass as a source of energy and the different conversion methods are discussed briefly in section 1.1. These methods are divided in two main groups, i.e. the biochemical and the thermochemical conversion methods. One advantage of thermochemical conversion is that it is typically faster than the biochemical conversion [4]. At the Karlsruhe Institute of Technology (KIT), Germany a two-stage process -bioliq® [3]- for biomass conversion into synthetic fuel is being developed based on a thermochemical conversion path. In this process, straw or other abundant lignocellulosic agricultural by-products are converted to syngas through fast pyrolysis and subsequent entrained flow gasification. After gas cleaning and conditioning, the syngas is converted into different chemicals via known processes such as direct methanol synthesis or Fischer-Tropsch synthesis. The bioliq® process will be discussed in more detail in section 1.2.

Through the entrained flow gasification as the second step in the bioliq® process, the biomass-based liquid slurry is converted into syngas. The goal of this study is the modeling and simulation of the gasification process inside an entrained flow gasifier and parametric studies to improve the knowledge on the biomass gasification process

as well as to design entrained flow gasifiers. Computational Fluid Dynamics (CFD), as a powerful tool for modeling and simulation of fluid flow processes, is utilized in this work. CFD simulations are nowadays easy to perform, and when sufficiently validated through experimental data, become a powerful design and optimization tool. As far as industrial applications are concerned, accurate simulation tools can be utilized for the scale-up of devices.

1.1 Biomass Gasification

Not long ago, humans' basic survival depended in whole or in part on the availability of biomass as a source of food and as an energy source for heating and cooking. Civilization began its energy use by burning biomass. The use of fossil fuels as a major energy source dates back to the recent centuries. According to United Nations Framework Convention on Climate Change (UNFCCC) [5], biomass is defined as

> non-fossilized and biodegradable organic material originating from plants, animals and micro-organisms. This shall also include products, by-products, residues and waste from agriculture, forestry and related industries as well as the non-fossilized and biodegradable organic fractions of industrial and municipal wastes.

Based on this definition, one can divide biomass into two basic groups:

- Virgin biomass which includes wood, plants and leaves (ligno-cellulose); and crops and vegetables (carbohydrates).
- Waste which includes municipal solid wastes, sewage, animal and human wastes and gases derived from landfilling, etc.

These two groups of biomass with their subclassifications are listed in Table 1.1 [6].

A major part of the virgin biomass and forestry and industrial wastes are ligno-cellulosic material whose major constituents are cellulose, hemicellulose and lignin. Smaller amounts of pectin, protein, extractives and ash are also part of biomass [7].

Table 1.2 shows the composition of some selected biomass sources. The composition can vary from one type to another and also inside the type due to different factors such as climate and time of harvest.

The ligno-cellulosic biomass is not a part of the human food chain and has a good potential for being used in bioenergy production. There are two major pathways

Virgin	Terrestrial biomass	Forest biomass
		Grasses
		Energy crops
		Cultivated crops
	Aquatic biomass	Algae
		Water plants
Waste	Municipal waste	Sewage
		Biosolids
		Landfill gas
	Agricultural solid waste	Livestock and manures
		Agricultural crop residue
	Forestry residues	Bark, leaves, floor residues
	Industrial waste	Demolition wood, sawdust
		Waste oil or fat

Table 1.1: Two major groups of biomass

for biomass conversion (Figure 1.1); i.e. biochemical conversion and thermochemical conversion. The biochemical conversion is subdivided to aerobic and anaerobic digestion and fermentation. Details about the biochemical conversion path can be found in [6] and [8]. The second path, the thermochemical conversion, has three important subdivisions, i.e. combustion, pyrolysis, and gasification.

Combustion involves high-temperature conversion of biomass in excess air into carbon dioxide and steam. Large amounts of heat are produced in this process. Combustion processes are available for conversion of virgin and waste biomass feed stocks to heat, steam, and electric power in advanced combustion systems.

Biomass pyrolysis can be described as the direct thermal decomposition of the organic components in biomass, in the absence of oxygen, to yield liquid and solid derivatives and fuel gases. In this process, large hydrocarbon molecules of biomass are broken into smaller hydrocarbon molecules. The amount of liquid, solid and gas products depends on pyrolysis operating conditions like temperature, pressure, heating rate and residence time inside the reactor. Unlike combustion, pyrolysis is not an exothermic process.

	Cellulose (%)	Hemicellulose (%)	Lignin (%)
Willow	50	19	25
Larch	26	27	35
Switchgrass	45	32	12
Corn cobs	45	35	15
Wheat straw	30	50	15

Table 1.2: Composition of some biomass sources [6, 7]

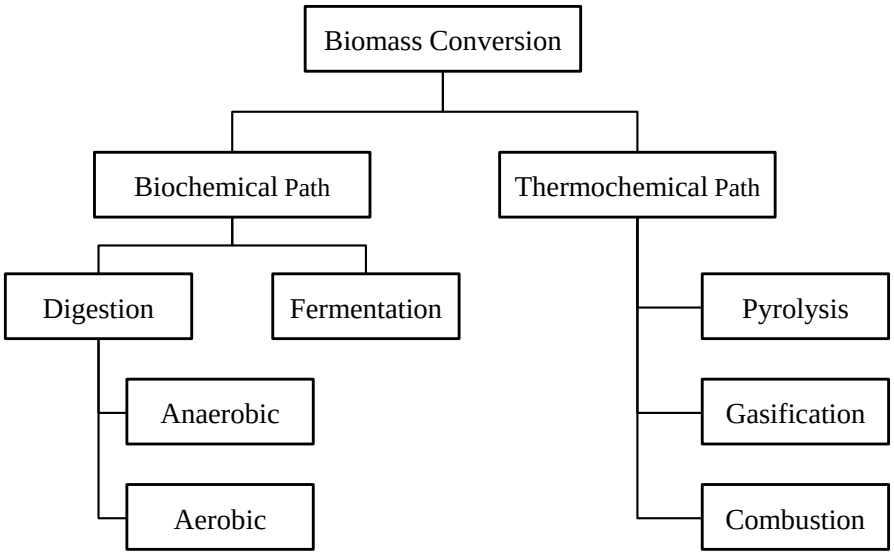

Figure 1.1: Pathways of biomass conversion (adapted from [6])

Gasification, which is the focus of this study, converts fossil or non fossil fuels into useful gases. It requires a medium for reaction, which can be gas or supercritical water [6]. Gaseous media include air, oxygen, steam, or a mixture of these. The gasifying agents react with solid carbon and (heavier) hydrocarbons to convert them into low-molecular-weight gases like CO and H_2. The product gases (syngas) can then be converted on catalysts into various products like Fischer-Tropsch (FT) diesel, olefins, methanol, ethanol, dimethyl ether (DME), hydrogen or other chemicals as can be seen in figure 1.2.

There are some major differences between gasification and combustion. Gasification packs energy into chemical bonds while combustion releases it. The gasification process takes place in reducing (oxygen-deficient) environments requiring heat, but in case of combustion the environment is oxidizing. In contrary to product gases from gasification, combustion product gases do not have a useful heating value.

Gasifiers are classified mainly on the basis of their gas-solid contact-mode and gasifying medium. Based on the gas-solid contact-mode, there are three major types of gasifiers used in industry [9]:

1. Moving or Fixed Bed Gasifiers
    - Updraft gasifiers
    - Downdraft gasifiers
    - Crossdraft gasifiers
2. Fluidized Bed Gasifiers (FBG)
    - Bubbling FBG
    - Circulating FBG
3. Entrained Flow Gasifiers (EFG)
    - Down Flow EFG
    - Up Flow EFG

In the fixed bed gasifiers, the solid fuel is supported in a fixed bed (grate) through which the gasifying medium flows in counter-current (updraft), co-current (downdraft) or cross-current (crossdraft) configurations. In the fluidized bed gasifiers, the fuel is fed to a suspended (bubbling) or circulating hot solid bed. The bed is kept in a fluidized condition by passing the gasifying medium at appropriate velocities through it. These and other types of gasifiers such as indirect gasifiers, cyclone gasifiers and heat pipe gasifiers are discussed in [9] in detail.

The gasifier used for this study is of entrained flow type. Entrained flow gasifiers normally use fuel in the form of gas, powder, or slurry and are widely used for large scale gasification of coal, petroleum coke, and refinery residues and are also a good choice for biomass-based slurry gasification. These gasifiers are characterized by fuel particles dragged along with the gas stream. This generally means short residence times, high temperatures, and small fuel particles [10]. The fuel is mixed with the oxidizing agent and gasified in a powder flame at high temperatures generally exceeding 1200 °C. This allows production of a gas rich in CO and H_2 that is nearly tar-free and has a very low methane content. A properly designed and operated entrained flow gasifier can have a carbon conversion rate close to 100 % [6]. Another advantage of this type of gasifier is that the high temperatures and pressures result in a leach resistance molten slag.

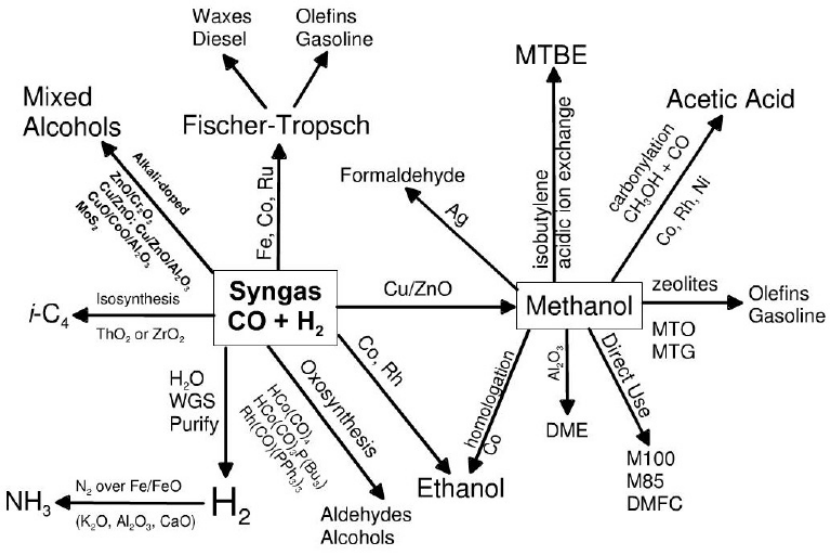

Figure 1.2: Pathways of syngas to chemicals [11]

1.2 The bioliq® Process

About 30 million tons of dry straw and wood residues from forestry are available in Germany per year for energetic usages [12]. This is about 43 % of the total amount of biomass produced in Germany. But the bulky and inconvenient form of biomass is a major barrier to industrial utilization of this energy source. Unlike gas or liquid, biomass cannot be handled, stored, or transported easily. This provides a major motivation for the conversion of solid biomass into liquid and gaseous fuels, which can be achieved through one of two major paths: (1) biochemical (fermentation) and (2) thermochemical (pyrolysis, gasification).

Based on the thermochemical conversion path, a two step pyrolysis/gasification process called bioliq® (biomass liquefaction) is developed at the Karlsruhe Institute of Technology (KIT), Germany [13]. In the first stage of the process, straw or other abundant lignocellulosic agricultural by-products are liquefied by fast pyrolysis at 500 °C and atmospheric pressure in an inert atmosphere using a twin screw reactor [3]. The purpose of fast pyrolysis is to gain as much liquid pyrolysis oil as possible with low yield of char and gas. The pyrolysis oil is then mixed with the char to prepare a slurry with up to 90 % of the original biomass energy content [3]. The slurries prepared in decentral facilities are transported by rail to a large central plant for gasification and fuel production.

The gasification process is performed by utilizing an entrained flow gasifier using technical O_2 as oxidizing agent. The gasification temperature and pressure are high, usually above 1200 °C and 30 bar [13], to achieve a tar-free syngas with low methane

content. After gas cleaning and adjustment of the H_2/CO ratio with the water gas shift reaction and CO_2 removal, the pure syngas can be converted on catalysts into various products like Fischer-Tropsch (FT) diesel, methanol, dimethyl ether (DME), olefins, hydrogen or other chemicals [14].

Figure 1.3 shows the process steps of bioliq®. After fast pyrolysis of biomass and slurry preparation in regional plants, the slurry is transported to large central plants for gasification, gas cleaning and fuel synthesis steps.

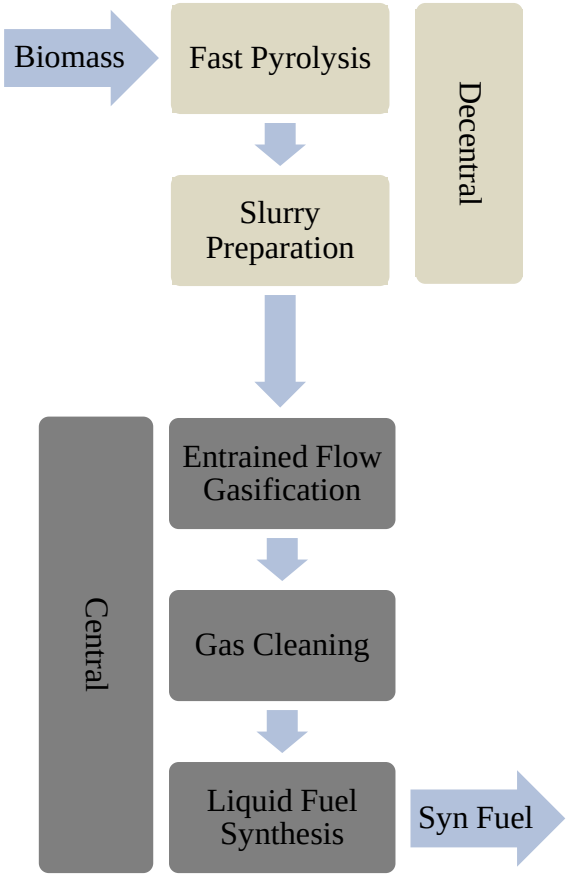

Figure 1.3: The bioliq® process steps (adapted from [15])

1.3 Computational Fluid Dynamics Modeling

Combustion and gasification have been a very important part of the energy conversion processes and remain key technologies for the foreseeable future. Effective and economic usage of energy resources as well as protecting the environment by producing less CO_2 and other pollutants during thermochemical processes need the employment of efficient conversion processes. Significant efforts have been focused

on the development of numerical models of thermochemical reactors (such as combustors, boilers and gasifiers). Due to availability of efficient computer systems nowadays, the numerical modeling techniques such as Computational Fluid Dynamics (CFD) methods are used in industry as well as in academia. CFD simulations help to optimize the system design and operation and understand the physical and chemical processes inside a reactor. They give the necessary predictive capacity for designing such systems. CFD modeling has established itself as a powerful tool for the development of new ideas and technologies. A good mathematical model can find optimum operating conditions, identify areas of concern or danger in operation, provide information on extreme operating conditions (high temperature, high pressure) where experiments are difficult to perform and helps to better interpret experimental results. Last but not least, modeling can address scale-up problems from one successfully operating size to another and from one feedstock to another.

Commercial software such as ANSYS CFX, ANSYS Fluent and CFD2000, as well as non-commercial codes, are available for CFD simulations. A review and comparison of these codes is given in [16] and [17]. ANSYS FLUENT 12.0 software is used in the framework of this study.

In the field of biomass combustion and gasification modeling, one still faces significant challenges due to complexity of the biomass composition. Many CFD studies have been performed for different biomass to energy conversion systems such as combustion [18, 19] or gasification systems [20, 21]. Through such simulations, the number of experiments needed to characterize the system can be considerably reduced. The simulations produce spatial and temporal profiles of different system variables that are either impossible to measure or are accessible only by expensive experiments.

1.4 Scope of this Thesis

This thesis is a part of the project "Synthesegaserzeugung durch Flugstromvergasung von Oel/Koks-Slurrys aus Biomasse - Grundlagen zur Prozessoptimierung" (Syngas generation by entrained flow gasification of biomass-based slurry - basics of process optimization) utilizing the bioliq® process. Within the framework of the project, the gasification process inside a lab scale entrained flow gasifier [22] is modeled and the CFD simulation is done using the commercially available software ANSYS FLUENT 12.0.

In order to perform a CFD simulation of a flow, the governing partial differential equations need to be solved numerically. These equations comprise the mass con-

servation equation, the momentum conservation equation, the energy conservation equation and - for reactive flows - the chemical species conservation equations, which will be discussed in Chapter 2.

Due to the turbulent nature of the flow and the high temperatures inside an entrained flow gasifier, proper techniques are required to model turbulence and thermal radiation, which, in addition to the methods for simulating fuel particle motion, will be discussed in Chapter 3.

Chapter 4 concentrates on the chemistry of gasification and the models for turbulence-chemistry interactions. The detailed chemical reaction mechanism used in this work will be introduced here. Models based on equilibrium chemistry, flamelet, and the eddy dissipation concept approaches will also be discussed in this chapter.

The governing equations and the additional physical and chemistry models are generally in the form of partial differential equations, the solution of which requires numerical methods. This thesis uses the finite volume method which will be discussed in Chapter 5 in more detail.

The CFD simulation results are presented in Chapter 6 along with the parameter studies conducted to identify the effect of different operating parameters such as inlet temperatures, oxidizer composition, air-fuel ratio, and pressure on the gasification process. Furthermore, the effect of the turbulence-chemistry coupling model - discussed in chapter 4 - are studied here. At the end of this chapter, the results of the slurry gasification simulation are presented.

In Chapter 7, the important results and findings are summarized and the perspective for future work and a few improvement propositions are given.

2. Governing Equations

The basic set of equations for continuous phase flow computation comprises the mass conservation equation, the momentum conservation equation and the energy conservation equation. The governing equations set for a general 3-dimensional fluid flow is known as Navier-Stokes equations. The equations describe both laminar and turbulent flows. In case of a chemically reacting flow, the system at each point can be completely described by specifying temperature, pressure, density and the velocity of the flow as well as the concentration of each species [23]. The latter is computed from corresponding chemical species conservation equations.

In this chapter the conservation equations are presented. Additional equations for modeling turbulence, chemistry, the discrete phase, and radiation are discussed in the following chapters.

2.1 Mass Conservation Equation

The general form of the mass conservation equation, also known as the continuity equation, is written as follows:

$$\frac{\partial \rho}{\partial t} + \nabla \cdot (\rho \vec{v}) = S_{\mathrm{m}} \tag{2.1}$$

The source S_{m} is the mass added to the continuous phase from the dispersed second phase (e.g., due to vaporization of liquid droplets).

2.2 Momentum Conservation Equation

The momentum equation, based on the Newton's laws of motion, relates the sum of the forces acting on a fluid element to its acceleration which is the rate of change of momentum in the direction of the resultant force [24].

The momentum conservation equation can be written in the following form [25]:

$$\frac{\partial}{\partial t}(\rho\vec{v}) + \nabla \cdot (\rho\vec{v}\vec{v}) = -\nabla p + \nabla \cdot (\bar{\tau}) + \rho\vec{g} + \vec{F} \tag{2.2}$$

where p is the static pressure, $\rho\vec{g}$ and $\vec{F}$ are the gravitational body force and external body forces (e.g., that arise from interaction with the dispersed phase [26]), respectively.

The stress tensor $\bar{\tau}$ in Equation 2.2 is defined by:

$$\bar{\tau} = \mu\left[(\nabla\vec{v} + \nabla\vec{v}^T) - \frac{2}{3}(\nabla \cdot \vec{v}I)\right] \tag{2.3}$$

where I is the unity matrix and $\vec{v}^T$ is the transpose of $\vec{v}$.

2.3 Energy Conservation Equation

Based on the first law of thermodynamics, stating that the internal energy gained by a system must be equal to the heat absorbed by the system minus work done by the system, one can obtain the equation of conservation of energy in the general form as follows:

$$\frac{\partial}{\partial t}(\rho E) + \nabla \cdot (\vec{v}(\rho E + p)) = \nabla \cdot \left(\lambda_{\text{eff}}\nabla T - \sum_{j=1}^{N} h_j\vec{J}_j + (\bar{\tau} \cdot \vec{v})\right) + S_{\text{h}} \tag{2.4}$$

where λ_{eff} is the effective thermal conductivity which will be defined in Chapter 3. The first three terms of the right hand side of the Equation 2.4 represent heat flux due to conduction according to the Fourier law of conduction, species diffusion and viscous dissipation due to normal shear stresses, respectively. The source term accounts for heat of chemical reactions, radiation and interaction with the dispersed phase [26](see chapters 3 and 4).

In the above equation,

$$E = h - \frac{p}{\rho} + v^2/2 \tag{2.5}$$

where the enthalpy h is defined as

$$h = \sum_{j=1}^{N} Y_j h_j, \tag{2.6}$$

with Y_j being the mass fraction of species j and

$$h_j = \int_{T_{\text{ref}}}^{T} c_{\text{p},j}\, \mathrm{d}T. \tag{2.7}$$

In the case of nonpremixed combustion (Section 4.2), assuming unity Lewis number ($Le = 1$), the following equation for the total enthalpy is solved

$$\frac{\partial}{\partial t}(\rho H) + \nabla \cdot (\rho \vec{v} H) = \nabla \cdot \left(\frac{\lambda_t}{c_{\text{p}}} \nabla H \right) + S_{\text{H}} \tag{2.8}$$

where the total enthalpy H is defined as

$$H = \sum Y_j H_j \tag{2.9}$$

and

$$H_j = \int_{T_{\text{ref}}}^{T} c_{\text{p},j}\, \mathrm{d}T + h_j^0(T_{\text{ref}}) \tag{2.10}$$

with $h_j^0(T_{\text{ref}})$ being the enthalpy of formation of species j at the reference temperature.

The Lewis number which quantifies the ratio of thermal diffusivity to mass diffusivity is defined as

$$Le = \frac{\lambda}{\rho c_{\text{p}} D_{i,\text{m}}}. \tag{2.11}$$

2.4 Species Conservation Equation

For each chemical species i, a convection-diffusion conservation equation is to be solved to calculate the corresponding species mass fraction (Y_i). This equation known as species mass conservation equation has the following general form

$$\frac{\partial}{\partial t}(\rho Y_i) + \nabla \cdot (\rho \vec{v} Y_i) + \nabla \cdot \vec{J}_i = R_i + S_i \tag{2.12}$$

where R_i is the rate of production of species i due to chemical reactions (see chapter 4) and S_i is any other source term. The diffusion flux $\vec{J}_i$ of the species i is given by

$$\vec{J}_i = -\left(\rho D_{i,\mathrm{m}} + \frac{\mu_\mathrm{t}}{Sc_\mathrm{t}}\right)\nabla Y_i - D_{\mathrm{T},i}\frac{\nabla T}{T}. \tag{2.13}$$

The diffusion flux term consists of the regular mass diffusion term according to the Fick's law and a thermal diffusion term according to the Soret effect [23]. Sc_t and μ_t are the turbulent Schmidt number and viscosity (discussed in chapter 3) respectively.

In turbulent flows it is not generally required to specify detailed laminar diffusion properties as the turbulent properties overwhelm the laminar ones [26]. $D_{\mathrm{T},i}$ is called coefficient of thermal diffusion which is only important for light species and low temperature [23].

When the system consists of N species, the equation 2.12 needs to be solved for $N-1$ species as according to the definition of Y_i the sum of mass fractions of all species is unity. Therefore for the last species the mass fraction is calculated as one minus the sum of $N-1$ solved mass fractions [26].

2.5 Reynolds- and Favre-Averaging

Full numerical solution of Navier-Stokes equation is a very difficult task for most engineering applications. In such flow problems with turbulent nature, the information of interest is limited usually to determine the mean values of quantities of interest, some measures for the extend of fluctuation and some measure to correlate these various quantities.

The idea of averaging consists in neglecting the whole set of flow details and consider that the flow can be described as the superposition of the mean field and a fluctuating field defined as the difference between the instantaneous and the mean field [25].

In Reynold averaging (also called time averaging), each quantity ϕ is composed of a mean and fluctuating value.

$$\begin{aligned} \phi &= \bar{\phi} + \phi', \\ \bar{\phi} &= \frac{1}{t_\phi}\int_0^{t_\phi} \phi(t)dt, \\ \bar{\phi'} &= 0, \end{aligned} \tag{2.14}$$

where t_ϕ is a large enough time to average out the fluctuations in ϕ.

Substituting expressions of this form for the flow variables into the instantaneous Navier-Stokes equations and taking a time (or ensemble) average, one gets the so called Reynolds-averaged Navier-Stokes equations (RANS).

Another form of averaging the equations is the Favre averaging (density-weighted average), in which all fluid mechanical quantities except pressure are mass averaged. Thus for a quantity ϕ,

$$\begin{aligned} \phi &= \tilde{\phi} + \phi'', \\ \tilde{\phi} &= \frac{\overline{\rho\phi}}{\bar{\rho}}, \\ \overline{\rho\phi''} &= 0. \end{aligned} \tag{2.15}$$

In equations 2.14 and 2.15, the bar indicates the Reynolds time averaging whereas the tilde denotes mass averaging. A double prime indicates the fluctuation about the mass-averaged mean and prime sign shows fluctuations for time averaging method.

Favre averaging has considerable advantages in simplifying the formulation of the averaged Navier-Stokes equations in variable density flows. In the momentum equations, but also in the balance equations for energy and the chemical species, the convective terms are dominant in high Reynolds number flows. Since these contain products of the dependent variables and the density, Favre averaging is the method of choice [27].

Conservation equations obtained by Favre averaging are identical in form to the RANS equations for constant density flow, making Favre averaging only a mathematical formalism [28, 29].

Reynolds averaged equations for mass and momentum conservation (equations 2.1 and 2.2) are as follows:

$$\frac{\partial \rho}{\partial t} + \nabla \cdot (\rho \bar{\vec{v}}) = \overline{S}_\mathrm{m}, \tag{2.16}$$

$$\frac{\partial}{\partial t}(\rho \bar{\vec{v}}) + \nabla \cdot (\rho \bar{\vec{v}} \bar{\vec{v}}) = -\nabla \bar{p} + \nabla \cdot (\bar{\tau}) - \nabla \cdot (\rho \overline{\vec{v}' \vec{v}'}) + \rho \vec{g} + \overline{\vec{F}}. \tag{2.17}$$

Applying Favre averaging to equations 2.1 and 2.2 one obtains

$$\frac{\partial \bar{\rho}}{\partial t} + \nabla \cdot (\bar{\rho} \tilde{\vec{v}}) = \widetilde{S}_\mathrm{m}, \tag{2.18}$$

$$\frac{\partial}{\partial t}(\bar{\rho}\tilde{\vec{v}}) + \nabla \cdot (\bar{\rho}\tilde{\vec{v}}\tilde{\vec{v}}) = -\nabla \bar{p} + \nabla \cdot (\bar{\tau}) - \nabla \cdot (\bar{\rho}\widetilde{\vec{v''}\vec{v''}}) + \bar{\rho}\vec{g} + \tilde{\vec{F}}. \tag{2.19}$$

Equations 2.17 and 2.19 are similar to Equation 2.2 except for the third term on the right hand side ($\nabla \cdot (\rho\overline{\vec{v'}\vec{v'}})$ and $\nabla \cdot (\bar{\rho}\widetilde{\vec{v''}\vec{v''}})$) due to the fluctuation in turbulent flows. These unknown correlation terms need to be modeled to close the equation system (see Section 3.1).

3. Physical Models

In this chapter, physical models are described that, in addition to the governing equations discussed in chapter 2, are required for the simulation of the fluid flow inside an entrained flow gasifier. These models take into consideration the effect of turbulence, thermal radiation and the interaction of the gas phase with the liquid fuel phase. The standard k-ε turbulence model will be introduced together with an improved version of it, called realizable k-ε model, which is used in this thesis for the modeling of turbulent fluid flow in the gasifier. The discrete ordinates model will be discussed in section 3.2 which is used to solve the thermal radiation transfer equation. In section 3.3, the discrete phase model (DPM), which utilizes the Euler-Lagrange approach to model the liquid fuel phase, will be discussed in detail.

3.1 Turbulence

Hinze [29] has defined a turbulent fluid motion as an irregular condition of flow with random spatio temporal variation of various quantities so that statistically distinct average values can be discerned. Turbulence causes an enhancement in mixing and accounts for the flow regime in most of the combustion applications.

As already discussed in section 2.5, each quantity is defined as a sum of an averaged value and a fluctuating part. The averaging method introduces additional unknown terms in the momentum equation. These terms are called Reynolds Stresses, defined as

$$Re_{ij} = \rho\overline{u_i' u_j'} \tag{3.1}$$

which stem from the momentum transfer by fluctuating velocity field. To model these stresses, the Boussinesq assumption [29] is used stating that

$$-\rho\overline{u_i'u_j'} = \mu_\mathrm{t}\left(\frac{\partial u_i}{\partial x_j}+\frac{\partial u_j}{\partial x_i}\right)-\frac{2}{3}\left(\rho k+\mu_\mathrm{t}\frac{\partial u_k}{\partial x_k}\right)\delta_{ij} \tag{3.2}$$

where μ_t is called turbulent (eddy) viscosity which, unlike the molecular viscosity, is not a property of the fluid. The closure problem is solved by expressing the turbulent viscosity in terms of known or calculable quantities. There are different methods to model turbulence, based on the number of transport equations solved to calculate μ_t, such as zero-equation models, one-equation models and two-equations models. The zero-equation model is nowadays obsolete [23]. In the one-equation models, as the name suggests, only one additional differential equation is solved to calculate the turbulent viscosity. k-ε and k-ω models are nowadays common types of turbulence models, which belong to the two-equation models category. The k-ε model, which defines the turbulent viscosity as a function of turbulent kinetic energy k and its dissipation rate ε, is used in the current work. The k-ω model solves two transport equations for turbulent kinetic energy k and specific dissipation ω, which can be thought as the ratio of ε to k [30].

3.1.1 Standard k-ε Model

The standard k-ε model was first proposed by Launder and Spalding [31] and is one of the most used turbulence models in computational fluid dynamics due to its robustness and reasonable accuracy for a wide range of flows. It is a semi empirical model based on transport equations for turbulent kinetic energy k and its dissipation rate ε. In the derivation of the model it is assumed that the flow is fully turbulent, and the effects of molecular viscosity are negligible [26]. Therefore it is valid only for fully turbulent flows.

The transport equations for turbulent kinetic energy and its dissipation rate are defined as

$$\frac{\partial}{\partial t}(\rho k)+\frac{\partial}{\partial x_i}(\rho k u_i)=\frac{\partial}{\partial x_j}\left[(\mu+\frac{\mu_\mathrm{t}}{\sigma_\mathrm{k}})\frac{\partial k}{\partial x_j}\right]+G_\mathrm{k}-\rho\varepsilon+S_\mathrm{k} \tag{3.3}$$

$$\frac{\partial}{\partial t}(\rho \varepsilon)+\frac{\partial}{\partial x_i}(\rho \varepsilon u_i)=\frac{\partial}{\partial x_j}\left[(\mu+\frac{\mu_\mathrm{t}}{\sigma_\varepsilon})\frac{\partial \varepsilon}{\partial x_j}\right]+C_{1\varepsilon}\frac{\varepsilon}{k}G_\mathrm{k}-C_{2\varepsilon}\rho\frac{\varepsilon^2}{k}+S_\varepsilon \tag{3.4}$$

where S_k and S_ε are the source terms for k and ε, respectively and G_k is the term for the production of turbulent kinetic energy due to the mean velocity gradients. The

	$C_{1\varepsilon}$	$C_{2\varepsilon}$	C_1	C_2	σ_k	σ_ε	C_μ
Standard k-ε	1.44	1.92	—	—	1.0	1.3	0.09
Realizable k-ε	—	—	Eq. 3.9	1.9	1.0	1.2	Eq. 3.12

Table 3.1: Values of constants for k-ε models ([26, 32])

empirical values for k and ε Prandtl numbers (σ_k and σ_ε) as well as the constants $C_{1\varepsilon}$ and $C_{2\varepsilon}$ are listed in Table 3.1.

The term G_k is defined as

$$G_\mathrm{k} = \mu_\mathrm{t} S^2 \tag{3.5}$$

with S being the modulus of the mean rate-of-strain tensor defined as

$$S = \sqrt{2 S_{ij} S_{ij}}. \tag{3.6}$$

The turbulent viscosity is computed from

$$\mu_\mathrm{t} = \rho C_\mu \frac{k^2}{\varepsilon} \tag{3.7}$$

where C_μ has a constant value as listed in Table 3.1.

3.1.2 Realizable k-ε Model

The standard k-ε model has some deficiencies such as anomaly about the spreading rate of planar and round jets [32]. To overcome these problems, a recent development of k-ε model is proposed by Shih et al. [32] called realizable k-ε model. It differs from the standard k-ε model in two ways. First, it contains a new formulation for the turbulent viscosity. Second, a new transport equation for the dissipation rate has been derived from an exact equation for the transport of the mean-square vorticity fluctuation. The term *realizable* means that the model satisfies certain mathematical constraints on the Reynolds stresses, consistent with the physics of turbulent flows.

The equation for turbulent kinetic energy is the same as that of the standard k-ε model (equation 3.3).

For the rate of dissipation (ε), the following equation is proposed

$$\frac{\partial}{\partial t}(\rho\varepsilon) + \frac{\partial}{\partial x_j}(\rho\varepsilon u_j) = \frac{\partial}{\partial x_j}\left[(\mu + \frac{\mu_\mathrm{t}}{\sigma_\varepsilon})\frac{\partial \varepsilon}{\partial x_j}\right] + \rho C_1 S\varepsilon - \rho C_2 \frac{\varepsilon^2}{k + \sqrt{\nu\varepsilon}} + S_\varepsilon \quad (3.8)$$

where C_1 is found to be a simple function of the time scale ratio of the turbulence to the mean strain, η

$$C_1 = \max\left[0.43\ ,\ \frac{\eta}{\eta + 5}\right] \quad (3.9)$$

with

$$\eta = S\frac{k}{\varepsilon} \quad (3.10)$$

and S defined by Equation 3.6. For the production of turbulent kinetic energy (G_k), the same equation (Equation 3.5) is used as in the case of the standard k-ε model.

As in the standard k-ε model, the turbulent viscosity is defined by Equation 3.7

$$\mu_\mathrm{t} = \rho C_\mu \frac{k^2}{\varepsilon} \quad (3.11)$$

where the value of C_μ is not a constant anymore and is defined as

$$C_\mu = \frac{1}{A_0 + A_\mathrm{s}\frac{kU^*}{\varepsilon}} \quad (3.12)$$

where

$$U^* = \sqrt{S_{ij}S_{ij} + \tilde{\Omega}_{ij}\tilde{\Omega}_{ij}} \quad (3.13)$$

and

$$\tilde{\Omega}_{ij} = \Omega_{ij} - 2\varepsilon_{ijk}\omega_k, \quad (3.14)$$

$$\Omega_{ij} = \bar{\Omega}_{ij} - \varepsilon_{ijk}\omega_k, \quad (3.15)$$

with $\bar{\Omega}_{ij}$ being the mean rate-of-rotation tensor viewed in a rotating reference frame with the angular velocity ω_k. The model constant $A_0 = 4.04$ and A_s is given by [32]:

$$A_s = \sqrt{6}\ \cos\phi \quad (3.16)$$

where

$$\phi = \frac{1}{3}\ \cos^{-1}(\sqrt{6}W), \tag{3.17}$$

$$W = \frac{S_{ij}S_{jk}S_{ki}}{\tilde{S}^3}, \tag{3.18}$$

$$\tilde{S} = \sqrt{S_{ij}S_{ij}}, \tag{3.19}$$

and

$$S_{ij} = \frac{1}{2}\left(\frac{\partial u_j}{\partial x_i} + \frac{\partial u_i}{\partial x_j}\right). \tag{3.20}$$

It can be seen that C_μ is a function of the mean strain and rotation rates, the angular velocity of the system rotation and the turbulence field. The model coefficients are summarized in Table 3.1.

The realizable k-ε model has been validated for a wide range of flow types. Its performance has been found to be substantially better than that of the standard k-ε model [32].

For both standard and realizable k-ε models, the effective thermal conductivity used in energy equation (Equation 2.4) is defined as

$$\lambda_{\text{eff}} = \lambda + \frac{c_{\text{p}}\mu_{\text{t}}}{Pr_{\text{t}}} \tag{3.21}$$

where, for the turbulent Prandtl number the value of $Pr_{\text{t}} = 0.85$ is used [26].

3.2 Thermal Radiation

All substances emit and absorb electromagnetic radiation continuously. The emitted radiation is, due to the molecular and atomic agitation, associated with the internal energy of the material [33]. Those radiations occupying intermediate wavelength range (approximately between $10^{-1}\mu$m and $10^{3}\mu$m) are called thermal radiation [33].

The importance of thermal radiation for gasification and combustion properties is its dependence on temperature. Generally for conduction and convection heat transfer,

the heat flux depends on the first power of temperature difference. The thermal radiative heat flux

$$Q_{\text{rad}} = \sigma(T_{\text{max}}^4 - T_{\text{min}}^4) \tag{3.22}$$

shows that the transfer of energy depends on the difference between the absolute temperatures each raised to a power of four. This depicts that the radiation heat transfer will be important at high absolute temperature difference levels. Consequently, one has to consider thermal radiation in combustion processes.

3.2.1 Radiative Transfer Equation

Radiation along a certain path is enhanced by emission and by scattering from other directions and is attenuated by absorption and scattering. Employing these concepts (see [33]), an equation governing the radiation intensity along a path through a medium is developed. This equation is called Radiative Transfer Equation (RTE) having the form

$$\frac{dI(\vec{r},\vec{s})}{ds} = -(a+\sigma_{\text{s}})I(\vec{r},\vec{s}) + a\frac{\sigma T^4}{\pi} + \frac{\sigma_{\text{s}}}{4\pi}\int_0^{4\pi} I(\vec{r},\vec{s'})\Phi(\vec{s}\cdot\vec{s'})d\Omega'. \tag{3.23}$$

In this equation, a is the absorption coefficient, σ_{s} is the scattering coefficient, the sum of which $(a+\sigma_{\text{s}})$ is called extinction coefficient and $(a+\sigma_{\text{s}})s$ is defined as optical thickness (opacity) of the medium. Furthermore, I, Φ and Ω' are the radiation intensity, phase function and solid angle, respectively. The phase function has the physical interpretation of being the scattered intensity in a direction, divided by the intensity that would be scattered in that direction if the scattering were isotropic [33]. For the current study, isotropic scattering, having $\Phi = 1$, is considered.

The intensity given by equation 3.23 is the local radiation traveling in a single direction per unit solid angle and wavelength. The first term on the right hand side of the equation indicates the loss by absorption (including the contribution by induced emission) and scattering. The second term indicates the gain by emission (not including induced emission) and the last term on the right hand side shows the gain by scattering (see Figure 3.1).

3.2.2 Discrete Ordinates Model

For an accurate modeling of high-temperature systems (such as combusting systems), one needs to solve the radiative transfer equation simultaneously with the

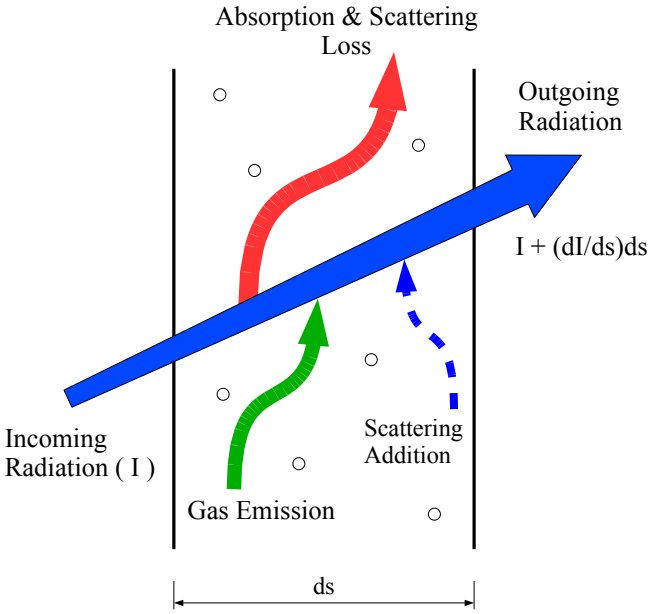

Figure 3.1: Radiative Heat Transfer (adapted from [26])

Navier-Stokes equations. This means that the model to solve the RTE must be computationally efficient enough to permit its inclusion in the other submodels and the numerical procedure used for the RTE must be compatible with the transport equations for the other processes [34]. Simple solutions are usually not possible for the RTE.

Many different methods have been developed for solving the equation of radiative transfer. They include methods such as P-N method, Monte Carlo method, discrete transfer method and discrete ordinates method (DOM). Each of these methods has its own relative advantages and disadvantages, and none of them is superior to others in all aspects. However, the DOM has been widely recognized to be one of the most appropriate methods in high-temperature applications because it shares the same philosophy and computational grid as the fluid dynamics approach [34] and can be employed in the entire range of optical thicknesses.

The P-N method [35] uses a set of moment equations of the RTE (by multiplying the RTE by various powers of the direction cosines of the intensity) and an expansion of the intensity in terms of the spherical harmonics (denoted by P) truncated after a selected number of terms (N) [33]. The Monte Carlo is a method of statistical simulation and consists of following a number of individual bundles of energy as they travel within the geometry and are absorbed or scattered [33, 36]. With the discrete transfer method [37], the total radiative flux is calculated by integrating the

energy contribution along rays emanating from the radiative source and pointing to any selected direction [38].

The discrete ordinates method (DOM) is an extension of a method called two-flux method [33] for studying radiative transfer in stellar atmosphere and later implemented by Fiveland [39, 40] for the analysis of heat transfer in coal-fired furnaces. In many studies, DOM has proved to produce good results in predicting radiation heat transfer [34, 40, 41, 42, 43] and is used in the context of this thesis as the RTE solution method.

The discrete ordinates model solves the radiative transfer equation for a finite number of discrete solid angles, each associated with a vector direction s_i $(i = 1, 2, ..., n)$ fixed in the global Cartesian system. The integrals over these directions are replaced by numerical quadratures. The model considers the RTE in the $\vec{s}$ direction as a field equation [26]. Thus, equation 3.23 is written as

$$\nabla \cdot (I(\vec{r}, \vec{s})\vec{s}) = -(a + \sigma_{\mathrm{s}})I(\vec{r}, \vec{s}) + a\frac{\sigma T^4}{\pi} + \frac{\sigma_{\mathrm{s}}}{4\pi}\int_0^{4\pi} I(\vec{r}, \vec{s'})\Phi(\vec{s} \cdot \vec{s'})d\Omega'. \tag{3.24}$$

In case of the presence of a second discrete phase in the flow, equation 3.24 is modified as follows

$$\nabla \cdot (I(\vec{r}, \vec{s})\vec{s}) = -(a + a_{\mathrm{p}} + \sigma_{\mathrm{p}})I(\vec{r}, \vec{s}) + a\frac{\sigma T^4}{\pi} + E_{\mathrm{p}} + \frac{\sigma_{\mathrm{s}}}{4\pi}\int_0^{4\pi} I(\vec{r}, \vec{s'})\Phi(\vec{s} \cdot \vec{s'})d\Omega'. \tag{3.25}$$

In the above equation other sources of scattering in the gas phase are neglected. a_{p}, E_{p} and σ_{p} are equivalent absorption coefficient of particles, equivalent particle emission and equivalent particle scattering factor, respectively, defined by [26]

$$a_{\mathrm{p}} = \lim_{V \to 0} \sum_{n=1}^{N} \epsilon_{\mathrm{pn}} \frac{A_{\mathrm{pn}}}{V}, \tag{3.26}$$

$$E_{\mathrm{p}} = \lim_{V \to 0} \sum_{n=1}^{N} \epsilon_{\mathrm{pn}} A_{\mathrm{pn}} \frac{\sigma T_{\mathrm{pn}}^4}{\pi V}, \tag{3.27}$$

$$\sigma_{\mathrm{p}} = \lim_{V \to 0} \sum_{n=1}^{N} (1 - f_{\mathrm{pn}})(1 - \epsilon_{\mathrm{pn}}) \frac{A_{\mathrm{pn}}}{V}, \tag{3.28}$$

where ϵ_{pn}, A_{pn}, T_{pn} and f_{pn} are emissivity, projected area, temperature and scattering factor of particle n.

The solid angle of 4π around a point at any spatial location is divided into several sectors. The size of each sector is determined from quadrature schemes. The transport equation is then solved for this set of discrete directions, represented by its direction cosines, spanning the total solid angle [42].

3.2.3 Radiation in Reactive Flow

Flames can be classified as luminous and nonluminous. The radiation from the nonluminous fraction of the combustion products is fairly well understood [33]. In the case of hydrocarbon combustion, the radiation is from the CO_2 and H_2O bands in the infrared. Luminous radiation, which is mostly due to soot particles, is not the subject of the present work.

There are different methods for specifying absorption-emittance of the radiating gases (see [33] and [44] for more detail about the available methods). One acceptable compromise between the very simple method of Gray Gases and complete models, taking into account the particular absorption bands, is the so called Weighted Sum of Gray Gases Model (WSGGM). In this model the gas is assumed to behave like a mixture of gray gases and a transparent medium to account for the windows between the absorption bands [33]. In this model the total emissivity over the distance s is calculated as

$$\epsilon = \sum_{i=0}^{I} a_{\epsilon,i} \left(1 - e^{-\kappa_i p s}\right). \tag{3.29}$$

The weighting factor $a_{\epsilon,i}$ depends on temperature and is defined in [45] as

$$a_{\epsilon,i} = \sum_{j=1}^{J} b_{\epsilon,i,j} T^{j-1} \tag{3.30}$$

where $b_{\epsilon,i,j}$ are the emissivity gas temperature polynomial coefficients, which together with κ_i, are determined by curve fitting of the experimental values of emittance of CO_2, H_2O and a mixture of these two gases (see [33] and [44]).

The WSGGM is examined in detail in [46]. Good results are obtained with a substantial reduction in computation time.

3.3 Discrete Phase Model

There are basically three numerical methods to solve the dispersed multiphase flows [47]. These methods are known as Euler-Lagrange, Euler-Euler and PDF methods.

The Discrete Phase Model (DPM), which is applied in this work, uses the Euler-Lagrange approach [26]. This approach treats the continuous phase (fluid phase) as a continuum and the particles as discrete entities. For the continuum, the Navier-Stokes equations, discussed in Chapter 2, are solved, while the dispersed phase is solved by tracking a large number of particles or droplets through the calculated flow field [48]. The dispersed phase can exchange momentum, mass, and energy with the fluid phase [26]. The Euler-Lagrange approach is the most popular model to solve multiphase flows [47].

In the PDF methods, the state of the flow at each position and time is described by a Probability Density Function (PDF), which can be a one variable or a joint multi-variable PDF. The transport equation of the PDF is deduced from the Navier-Stokes equations [49, 50].

3.3.1 Particle Motion Theory

Newton's second law of motion is the governing equation of motion of the particles in the DPM. According to this law, the sum of the forces acting on a particle is responsible for its acceleration. The equation of motion can be written as

$$\frac{du_\mathrm{p}}{dt} = F_\mathrm{D}(u - u_\mathrm{p}) + \frac{g_\mathrm{x}(\rho_\mathrm{p} - \rho)}{\rho_\mathrm{p}} + F_\mathrm{x} \tag{3.31}$$

where $F_\mathrm{D}(u - u_\mathrm{p})$ is the drag force basically due to the frictional effects as defined below and F_x is any other force acting on the particle, both per unit particle mass. F_x can be the *virtual mass* force negligible when $\rho < \rho_\mathrm{p}$, force due to pressure gradient in the fluid, thermophoretic force or Brownian force, which are all neglected in the current study. The drag force is often dominating the motion of the particle [47]. The second term on the right hand side of equation 3.31 is due to the buoyancy (based on Archimedes's principle) and gravitational force.

F_D is defined as

$$F_\mathrm{D} = \frac{3}{4} \cdot \frac{\mu C_\mathrm{D} Re}{\rho_\mathrm{p} d_\mathrm{p}^2} \tag{3.32}$$

where Re is the particle Reynolds Number to characterize the effect of dispersed phase on the turbulence variation of the carrier gas, defined by

$$Re = \frac{\rho d_\mathrm{p} |u_\mathrm{p} - u|}{\mu}. \tag{3.33}$$

The drag coefficient C_D is used to model the dependency between particle and flow condition. The spherical drag law is considered in this study, stating that the drag coefficient can be defined as

$$C_\mathrm{D} = a_1 + \frac{a_2}{Re} + \frac{a_3}{Re^2}. \tag{3.34}$$

The coefficients a_1, a_2 and a_3 are defined in the work of Morsi and Alexander [51] for several ranges of Re.

In order to take into account the effect of turbulence on the dispersion of the particles, the stochastic tracking model has been used, which employs the instantaneous gas velocity, $u = \bar{u} + u'(t)$ along the particle path during the calculations.

The time, a particle spends in turbulent motion along its path ds, is known as integral time scale τ_T presented by

$$\tau_\mathrm{T} = \int_0^\infty \frac{u'_\mathrm{p}(t)u'_\mathrm{p}(t+s)}{\overline{u'^2_\mathrm{p}}} ds \tag{3.35}$$

For small *tracer* particles that move with the fluid (zero drift velocity), the integral time becomes the fluid Lagrangian integral time τ_L, which can be approximated for the k-ε turbulence model [26], [52] as

$$\tau_\mathrm{L} \approx 0.15\frac{k}{\varepsilon}. \tag{3.36}$$

A stochastic method (random walk model) is used to determine the instantaneous gas velocity. In the discrete random walk (DRW) model, also known as *eddy lifetime* model, the fluctuating velocity components are discrete piecewise constant functions of time. Their random value is kept constant over an interval of time given by the characteristic lifetime of the eddies [26].

In this model, the fluctuating velocity components u_i , that prevail during the lifetime of the turbulent eddy are sampled by assuming that they obey a Gaussian probability distribution, so that

$$u' = \zeta\sqrt{\overline{u'^2}} \tag{3.37}$$

where ζ is a normally distributed random number. The RMS value of the velocity fluctuation is computed (assuming isotropy) as

$$\sqrt{\overline{u_i'^2}} = \sqrt{\frac{2k}{3}}. \tag{3.38}$$

The interaction time between particles and eddies is the smaller of the eddy lifetime τ_e, and the particle eddy crossing time t_{cross}. The characteristic lifetime of the eddy is defined as

$$\tau_e = 2\tau_L \tag{3.39}$$

where τ_L is given by equation 3.36.

The particle eddy crossing time is defined as

$$t_{cross} = -\tau \ln\left[1 - \left(\frac{L_e}{\tau|u - u_p|}\right)\right] \tag{3.40}$$

where τ is the particle relaxation time $\left(\tau = \frac{\rho_p d_p^2}{18\rho\nu}\right)$, a measure for how a particle reacts after a sudden flow velocity change, and L_e is the eddy length scale. The particle interacts with the fluid eddy over the interaction time. When the eddy lifetime is reached, a new value of the instantaneous velocity is obtained by applying a new value of ζ in equation 3.37 [26].

Integration of the equation 3.31 yields the velocity of the particle at each point along the trajectory. The trajectory itself can be calculated by solving

$$\frac{dx}{dt} = u_p. \tag{3.41}$$

Equations 3.31 and 3.41 are a set of coupled ordinary differential equations, the numerical solution of which will be discussed in chapter 5 in detail.

3.3.2 Heat and Mass Exchange

The particles can exchange heat and mass with the continuous phase. Based on the particle type, these exchanges might be different resulting in different heat and mass transfer relationships, also called *laws*. The particles considered in this study are liquid droplets. The droplets can undergo different laws (e.g. inert heating, evaporation or boiling) according to the physical condition of the continuous phase. These contain inert heating of the particle, evaporation and boiling.

Unless the particle temperature T_p is less than the evaporation temperature T_{vap}, the particle exchanges heat according to the following law

$$m_{\mathrm{p}} c_{\mathrm{p}} \frac{dT_{\mathrm{p}}}{dt} = hA_{\mathrm{p}}(T_\infty - T_{\mathrm{p}}) + \epsilon_{\mathrm{p}} A_{\mathrm{p}} \sigma(\theta_{\mathrm{R}}^4 - T_{\mathrm{p}}^4) \tag{3.42}$$

where $m_{\mathrm{p}}, c_{\mathrm{p}}, A_{\mathrm{p}}$ and ϵ_{p} are the mass, heat capacity, surface area and emissivity of the particle, correspondingly, and h is the convective heat transfer coefficient.

This equation is derived by a simple energy balance of the particle, assuming that the particle is at a uniform temperature throughout. The first term on the right hand side of the equation denotes the convective heat transfer and the second term indicates radiation heat transfer with $\theta_{\mathrm{R}} = \left(\frac{G}{4\sigma}\right)^{1/4}$ being the radiation temperature and $G = \int_{\Omega=4\pi} I d\Omega$ being the incident radiation (see section 3.2 for more details).

Equation 3.42 is integrated in time using an approximate, linearized form that assumes that the particle temperature changes slowly from one time value to the next [26]:

$$m_{\mathrm{p}} c_{\mathrm{p}} \frac{dT_{\mathrm{p}}}{dt} = A_{\mathrm{p}} \left\{ - \left[h + \epsilon_{\mathrm{p}} \sigma T_{\mathrm{p}}^3 \right] T_{\mathrm{p}} + \left[hT_\infty + \epsilon_{\mathrm{p}} \sigma \theta_{\mathrm{R}}^4 \right] \right\}. \tag{3.43}$$

Integrating the above equation yields

$$T_{\mathrm{p}}(t + \Delta t) = \alpha_{\mathrm{p}} + \left[T_{\mathrm{p}}(t) - \alpha_{\mathrm{p}} \right] e^{-\beta_{\mathrm{p}} \Delta t} \tag{3.44}$$

with Δt being the time step and

$$\alpha_{\mathrm{p}} = \frac{hT_\infty + \epsilon_{\mathrm{p}} \sigma \theta_{\mathrm{R}}^4}{h + \epsilon_{\mathrm{p}} \sigma T_{\mathrm{p}}^3(t)} \tag{3.45}$$

and

$$\beta_{\mathrm{p}} = \frac{A_{\mathrm{p}}(h + \epsilon_{\mathrm{p}} \sigma T_{\mathrm{p}}^3(t))}{m_{\mathrm{p}} c_{\mathrm{p}}}. \tag{3.46}$$

Ranz and Marshall [53, 54] proposed the following equation for calculating the convective transfer coefficient

$$Nu = \frac{hd_{\mathrm{p}}}{k_\infty} = 2.0 + 0.6 Re_{\mathrm{d}}^{1/2} Pr^{1/3} \tag{3.47}$$

where k_∞ is the thermal conductivity of the continuous phase and $Pr = \frac{c_{\mathrm{p}} \mu}{k_\infty}$ is the Prandtl number of the continuous phase. The particle Reynolds number is defined in equation 3.33.

The heat transfer by the particle as it traverses each computational cell appears as a source or sink of heat in subsequent calculations of the continuous phase energy equation. In this case, droplets do not exchange mass with the continuous phase and do not participate in any chemical reaction [26].

When the temperature of the particle is between the evaporation temperature and boiling temperature $T_{\text{vap}} \leq T_{\text{p}} < T_{\text{bp}}$, the droplet exchanges heat and mass according to the evaporation law. During this law, the rate of vaporization is governed by gradient diffusion, with the flux of droplet vapor into the gas phase defined as:

$$N_i = k_{\text{c}}(C_{i,\text{s}} - C_{i,\infty}) \tag{3.48}$$

where k_{c} is the mass transfer coefficient and the term in the parentheses indicates the difference in vapor concentration between the droplet surface and the bulk gas.

The mass transfer coefficient k_{c} is calculated using the following correlation for the Sherwood number [53, 54]:

$$Sh_{\text{AB}} = \frac{k_{\text{c}} d_{\text{p}}}{D_{i,\text{m}}} = 2.0 + 0.6 Re_{\text{d}}^{1/2} Sc^{1/3} \tag{3.49}$$

with the Schmidt number defined as $Sc = \frac{\mu}{\rho D_{i,\text{m}}}$ and $D_{i,\text{m}}$ being the diffusion coefficient of vapor in the bulk.

For the calculation of the vapor concentration at the droplet surface, assuming that the partial pressure of vapor at the interface is equal to the saturated vapor pressure at the droplet temperature, $p_{\text{sat}}(T_{\text{p}})$, the following equation can be used.

$$C_{i,\text{s}} = \frac{p_{\text{sat}}(T_{\text{p}})}{R T_{\text{p}}}. \tag{3.50}$$

The vapor concentration in the bulk gas is defined by

$$C_{i,\infty} = X_i \frac{p}{R T_{\infty}} \tag{3.51}$$

where X_i is the local bulk mole fraction of species i and R is the universal gas constant.

The vapor flux calculated by equation 3.48 is used as a source term for species i in the species transport equation (see equation 2.12).

The mass of the droplet reduces according to

$$m_{\mathrm{p}}(t+\Delta t) = m_{\mathrm{p}}(t) - N_i A_{\mathrm{p}} M_{\mathrm{w},i} \Delta t \tag{3.52}$$

where $M_{\mathrm{w},i}$ is the molecular weight of the species i.

The heat transfer equation according to this law is similar to equation 3.42 with an additional term due to droplet evaporation

$$m_{\mathrm{p}} c_{\mathrm{p}} \frac{dT_{\mathrm{p}}}{dt} = hA_{\mathrm{p}}(T_\infty - T_{\mathrm{p}}) + \epsilon_{\mathrm{p}} A_{\mathrm{p}} \sigma(\theta_{\mathrm{R}}^4 - T_{\mathrm{p}}^4) + \frac{dm_{\mathrm{p}}}{dt} h_{\mathrm{fg}} \tag{3.53}$$

where h_{fg} is the latent heat of evaporation. The heat transferred according to this law becomes a source of energy during subsequent calculations of the continuous phase energy equation.

When the temperature of the droplet reaches the boiling temperature T_{bp}, the droplet starts to boil and the droplet boiling law is used to predict the heat and mass exchange with the continuous phase. According to this law and assuming that the droplet temperature remains constant during boiling, equation 3.53 is modified to calculate the boiling rate:

$$-\frac{dm_{\mathrm{p}}}{dt} h_{\mathrm{fg}} = hA_{\mathrm{p}}(T_\infty - T_{\mathrm{p}}) + \epsilon_{\mathrm{p}} A_{\mathrm{p}} \sigma(\theta_{\mathrm{R}}^4 - T_{\mathrm{p}}^4) \tag{3.54}$$

or

$$-\frac{d(d_{\mathrm{p}})}{dt} = \frac{2}{\rho_{\mathrm{p}} h_{\mathrm{fg}}} \left[\frac{k_\infty Nu}{d_{\mathrm{p}}} (T_\infty - T_{\mathrm{p}}) + \epsilon_{\mathrm{p}} \sigma(\theta_{\mathrm{R}}^4 - T_{\mathrm{p}}^4) \right]. \tag{3.55}$$

Using equation 3.47 for the Nusselt number and an empirical value for the Prandtl number in the above equation [26], it becomes

$$-\frac{d(d_{\mathrm{p}})}{dt} = \frac{2}{\rho_{\mathrm{p}} h_{\mathrm{fg}}} \left[\frac{k_\infty \left[1 + 0.23\sqrt{Re_{\mathrm{d}}}\right]}{d_{\mathrm{p}}} (T_\infty - T_{\mathrm{p}}) + \epsilon_{\mathrm{p}} \sigma(\theta_{\mathrm{R}}^4 - T_{\mathrm{p}}^4) \right]. \tag{3.56}$$

As long as the droplet boiling law governs, the energy required for vaporization appears as a (negative) source term in the energy equation for the gas phase and the evaporated liquid enters the gas phase.

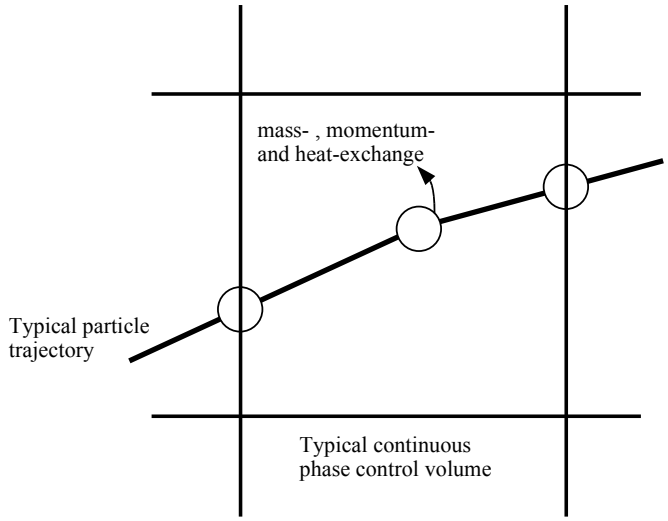

Figure 3.2: Mass, momentum and heat exchange between discrete and continuous phases (adapted from [26])

3.3.3 Coupling with the Continuous Phase

Based on the particle volume fraction, Elgobashi [55] has defined different classes of interactions between the different phases. When the discrete phase has a negligible effect on the turbulence of the continuous phase, one talks about *one-way coupling*. When the particle volume fraction increases, feedback of the dispersed phase on the properties of the continuous phase fluid dynamics must also be taken into account, which is known as *two-way coupling*. In the case of dense flows, particle-particle interactions have to be considered as well. This class of interactions is known as *four-way coupling*. For this study a two-way coupling is taken into consideration based on the criteria of [55]. In this way both phases exchange mass, momentum and heat with each other. This interphase exchange from the particle to the continuous phase is depicted qualitatively in Figure 3.2.

The transfer of mass, momentum and heat from the continuous phase to the particle is computed by determining the change in corresponding variables of the particle as it passes through each control volume.

The mass change is computed as

$$M = \frac{\Delta m_{\mathrm{p}}}{\Delta m_{\mathrm{p,0}}} \dot{m}_{\mathrm{p,0}} \tag{3.57}$$

This mass exchange appears as a source term in the continuity equation and also in the corresponding species conservation equation.

The momentum exchange is computed as

$$F = \sum \left(\frac{3}{4} \cdot \frac{\mu C_{\mathrm{D}} Re}{\rho_{\mathrm{p}} d_{\mathrm{p}}^2} (u_{\mathrm{p}} - u) + F_{\mathrm{other}} \right) \dot{m}_{\mathrm{p}} \Delta t \tag{3.58}$$

where the summation is over all the control volumes (see section 5.1) that the particle passes through and F_{other} is any force other than drag force. This momentum force is used as a source term in the continuous phase momentum equation.

In the absence of chemical reactions of particles, the following equation is used to compute the heat exchange with continuous phase:

$$Q = \frac{\dot{m}_{\mathrm{p},0}}{m_{\mathrm{p},0}} \left[H_{\mathrm{lat,ref}} (m_{\mathrm{p,out}} - m_{\mathrm{p,in}}) - m_{\mathrm{p,out}} \int_{T_{\mathrm{ref}}}^{T_{\mathrm{p,out}}} c_{\mathrm{p_p}} dt + m_{\mathrm{p,in}} \int_{T_{\mathrm{ref}}}^{T_{\mathrm{p,in}}} c_{\mathrm{p_p}} dt \right] \tag{3.59}$$

where the subscripts *in* and *out* are for cell entry and exit correspondingly and subscript 0 indicates the initial value of the variable. The latent heat at reference conditions $H_{\mathrm{lat,ref}}$, is defined as the difference between liquid and gas standard formation enthalpies and can be related to the latent heat at the boiling point H_{lat}, using the following equation:

$$H_{\mathrm{lat,ref}} = H_{\mathrm{lat}} - \int_{T_{\mathrm{ref}}}^{T_{\mathrm{bp}}} c_{\mathrm{p_g}} dt + \int_{T_{\mathrm{ref}}}^{T_{\mathrm{bp}}} c_{\mathrm{p_p}} dt \tag{3.60}$$

with T_{bp} and T_{ref} being the boiling point and reference temperatures correspondingly.

In the case of chemical reactions of particles, a fraction of the energy produced by the reactions is used additionally as a heat source for the continuous phase and the rest of it is absorbed by the particle directly [56].

4. Chemistry Models

The use of global reactions in reactive flow problems does not completely take into account the effects of the chemical intermediates. On the other hand, a detailed description of chemistry gives a deeper insight into reactive flow processes such as combustion and gasification but requires often a prohibitive amount of calculation time. The detailed chemical mechanism required to describe such processes contains typically hundreds of chemical species in thousands of elementary reactions. In this chapter the basics of chemical kinetics and reaction mechanism development are discussed.

In order to perform a CFD simulation of a reactive flow, chemistry models should be used together with other fluid mechanical submodels. In case of very fast chemistry, the chemistry can be decoupled from the flow and the Chemical Equilibrium model can be used. For such cases the molecular species concentrations and temperature are functions of only one progress variable, i.e. the mixture fraction. In the Flamelet model, two progress variables are required to fully describe the system. These two variables are mixture fraction and scalar dissipation rate. The flamelet model uses also the principle of decoupling chemistry from the fluid flow but takes the nonequilibrium effects into consideration by using the second progress variable. These two models will be discussed later in this chapter.

At the end of the chapter, the Eddy Dissipation Concept (EDC) will be introduced which is a chemistry-turbulence interaction model that considers detailed chemical reaction mechanisms in turbulent reactive flows. Here, the chemistry and fluid flow calculations will not be decoupled. EDC is a computationally expensive model and should be used where the assumption of fast chemistry is not valid. The assumption of fast chemistry and accordingly decoupling of chemistry from the fluid flow is

based on the comparison of the time scales of chemistry and physical processes. The chemical reactions typically cover a time range from 10^{-10} s to more than 1 s [23, 27]. The physical processes like molecular transport, on the other hand, cover a much smaller range as can be seen in Figure 4.1.

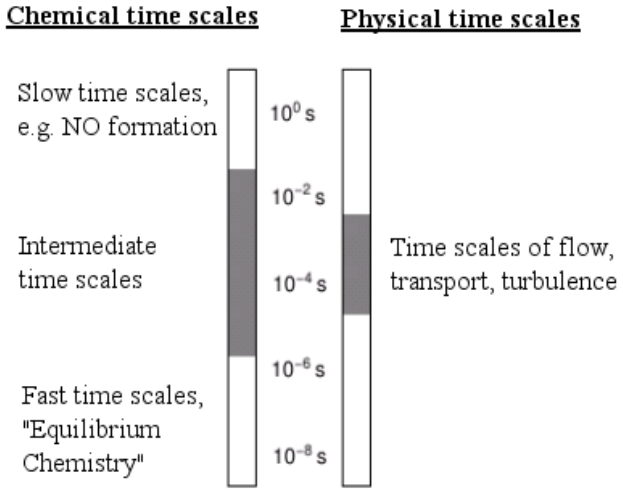

Figure 4.1: Time Scales in a Reactive Flow [23]

4.1 Chemical Reaction Mechanism

A chemical reaction with N chemical species can be described by:

$$\sum_{i=1}^{N} \nu_i' A_i \xrightarrow{k_\mathrm{f}} \sum_{i=1}^{N} \nu_i'' A_i \tag{4.1}$$

where ν_i' and ν_i'' are the stoichiometric coefficients for reactants and products, A_i denotes the chemical species i and k_f is the rate coefficient. The reaction rate of creation/destruction of species i can be written as

$$\frac{dc_i}{dt} = (\nu_i'' - \nu_i') \left(k_\mathrm{f} \prod_{i=1}^{N} c_i^{n_{i,\mathrm{f}}} \right) \tag{4.2}$$

with c_i being the concentration of species i and $n_{i,\mathrm{f}}$ being the reaction order with respect to this species.

For the reverse reaction of 4.1, having a rate coefficient of k_r, the reaction rate is defined as

$$\frac{dc_i}{dt} = -(\nu_i'' - \nu_i') \left(k_\mathrm{r} \prod_{i=1}^{N} c_i^{n_{i,\mathrm{r}}} \right) \tag{4.3}$$

where $n_{i,\mathrm{r}}$ is the reaction order of the i^{th} product species.

At chemical equilibrium, the forward and reverse reactions have the same rate, i.e.

$$(\nu_i'' - \nu_i') \left(k_{\mathrm{f}} \prod_{i=1}^{N} c_i^{n_{i,\mathrm{f}}} \right) = (\nu_i'' - \nu_i') \left(k_{\mathrm{r}} \prod_{i=1}^{N} c_i^{n_{i,\mathrm{r}}} \right) \tag{4.4}$$

meaning that no net reaction can be observed on a macroscopic level. The equilibrium constant K_{c}, which represents the relation between the forward and reverse reactions is obtained as

$$K_{\mathrm{c}} = \frac{k_{\mathrm{f}}}{k_{\mathrm{r}}} = \prod_{i=1}^{N} c_i^{(\nu_i'' - \nu_i')} \tag{4.5}$$

The equilibrium constant for the j^{th} reaction is computed, based on the change in Gibbs free energy, from

$$K_{\mathrm{c},j} = \exp\left(\frac{\Delta S_j^0}{R} - \frac{\Delta H_j^0}{RT} \right) \left(\frac{p_0}{RT} \right)^{\sum_{i=1}^{N} (\nu_{i,j}'' - \nu_{i,j}')} \tag{4.6}$$

where p_0 is the atmospheric pressure and R is the universal gas constant. The values of ΔS_j^0 and ΔH_j^0 being the entropy and enthalpy of reaction at standard conditions, respectively, are calculated from thermodynamical databases (for example from [57] or [58]). The reverse reaction rate coefficient k_{r} can then be determined from k_{f} and the equilibrium constant calculated from Equation 4.6.

The reaction rate coefficient k depends strongly on temperature in a nonlinear manner [23]. Arrhenius gave an impirical expression for the form of this dependence in 1889 as [59]

$$k = A' \cdot e^{\left(-\frac{E_{\mathrm{a}}'}{RT} \right)}. \tag{4.7}$$

The pre-exponential factor A' in the above equation can be a function of temperature as well [23]. Therefore, the following expression is used to calculate the rate coefficient:

$$k = AT^b \cdot e^{\left(-\frac{E_{\mathrm{a}}}{RT} \right)}, \tag{4.8}$$

where A and b are the pre-exponential factor and temperature exponent, respectively. The activation energy E_{a} corresponds to an energy barrier to be overcome during

the reaction. Its maximum value corresponds to the bond energies in the molecule, but can be much smaller if new bonds are formed simultaneously as the old bonds break [23].

Under certain conditions for some dissociation/recombination reactions, the reaction rates depend strongly on pressure as well as temperature [23]. The pressure dependence of these so called fall-off reactions is described by two limiting situations; high pressure and low pressure limits. For both low pressure limit (k_0) and high pressure limit (k_∞), the rate coefficients are in the form of Equation 4.8. The rate coefficients for these two limits are then blended to produce a smooth pressure dependence rate expression. An often used formalism is the *F-Center treatment* of Troe [60, 61]. In this method the scaled rate coefficient $\frac{k}{k_\infty}$ is expressed as the product of the Lindemann-Hinshelwood formula [62] and a factor F :

$$\frac{k}{k_\infty} = \left(\frac{p_\mathrm{r}}{1+p_\mathrm{r}}\right) F \tag{4.9}$$

where p_r is defined as

$$p_\mathrm{r} = \frac{k_0[M]}{k_\infty} \tag{4.10}$$

with $[M]$ being the concentration of the collision partner. F is called the Lorentzian broadening factor which is used to reduce the systematic errors associated with the Lindemann-Hinshelwood formula in the pressure fall-off range [63] and is given by

$$\log F = \log F_\mathrm{cent} \left\{1 + \left(\frac{\log p_\mathrm{r} + c}{n - d(\log p_\mathrm{r} + c)}\right)^2\right\}^{-1} \tag{4.11}$$

where

$$\begin{aligned} c &= -0.4 - 0.67 \log F_\mathrm{cent} \\ n &= 0.75 - 1.27 \log F_\mathrm{cent} \\ d &= 0.14 \end{aligned} \tag{4.12}$$

and F_cent describing the center of the fall-off range as a function of temperature

$$F_\mathrm{cent} = (1-a)\exp(-\frac{T}{T^{***}}) + a\exp(-\frac{T}{T^{*}}) + \exp(-\frac{T^{**}}{T}). \tag{4.13}$$

The parameters a, T^{***}, T^{*} and T^{**} as well as the Arrhenius parameters for the low and high pressure limits are specified for each pressure dependent reaction.

4.1.1 Reaction Mechanism Development

The chemistry of combustion and gasification is described by chemical reaction mechanisms containing tens of species in hundreds of reactions. A reaction mechanism is defined as a complete set of elementary reactions together with their rate coefficients. The interaction of these elementary reactions produces the overall balanced stoichiometric chemical equation of the global reaction. On the contrary to global reactions, elementary reactions occur on a molecular level exactly in the way which is described by the reaction equation [23].

For the current study, a reaction mechanism is developed for the high temperature gasification of ethylene glycol [64]. Ethylene glycol ($HOCH_2CH_2OH$) is used as non-toxic model fuel for the pyrolysis oil by Karlsruhe Institute of Technology (KIT), where experimental measurements were performed. The base mechanism is an improved version of a previously validated C_1 - C_4 mechanism [65], consisting of 61 species and 778 elementary reactions. This mechanism is enhanced by reactions for ethanol [66]. Reaction constants of reactions with ethylene glycol and its products are implemented based on experiments, similar reaction schemes or estimated using analogy methods. The modified reaction scheme consists of 80 species and 1243 elementary reactions [64]. For details on development and validation of the ethylene glycol reaction mechanism, the reader is referred to [64].

4.1.2 Reaction Mechanism Simplification

The main problem in the use of detailed reaction mechanisms in CFD simulations is given by the fact that for each species of the mechanism, one species conservation equation (Equation 2.12) needs to be solved. This is bonded with a great amount of computer resources and computation time. Depending on the actual conditions in a numerical study, many of the reactions and corresponding species can be neglected. Here, analysis methods to eliminate these reactions, are of interest.

In order to simplify the developed reaction mechanism, two methods are used; sensitivity analysis and reaction flow analysis [23]. The sensitivity analysis identifies the rate-limiting reaction steps. For the determination of characteristic reaction paths, reaction flow analysis is performed.

The simulation program HOMREA [67] is used for the computation of time dependent homogeneous reaction systems. The governing equations are derived from the Navier-Stokes equations discussed in Chapter 2 and are solved numerically with either a modified DASSL [68] or a modified LIMEX [69] solver, neglecting the radiative heat fluxes. With the computational package MIXFLA [70], the simulation of

flame speeds and structure of stationary premixed 1-dimensional laminar flat flames can be performed.

The sensitivity analysis of the reaction mechanism is done for the ignition delay times and species concentrations using HOMREA and for the flame velocity using MIXFLA. The rate laws for the reaction mechanism can be written as a system of first order ordinary differential equations with rate coefficients as parameters of the system. The program HOMREA can also be used for reaction flow analysis, where the contributions of different reactions to the formation or consumption of a chemical species are considered.

4.2 Nonpremixed Combustion with Equilibrium Chemistry

The nonpremixed combustion occurs when combustion and mixing of fuel and oxidizer occur simultaneously [23]. This type of combustion is used mostly in industrial furnaces and burners due to safety issues. In case of very fast chemistry, the *mixed-is-burnt* model can be used assuming that the combustion occurs as soon as the fuel and oxidant mix with each other. For such cases, the molecular species concentrations and temperature are functions of only one conserved scalar [71]. There are a number of conserved scalars that can be used to describe the mixing in such flows. Under the assumption of equal diffusivity (meaning all species diffuse alike), the mixture fraction f is such a variable. It is defined as

$$f = \frac{Z_i - Z_{i2}}{Z_{i1} - Z_{i2}} \tag{4.14}$$

with Z_i being the mass fraction of element i. The subscripts 1 and 2 refer to the two feed streams (fuel and oxidant streams respectively). Mixture fraction varies between 1 for the fuel stream and 0 the for oxidant stream and can be interpreted as the mass fraction originated from the fuel stream.

To calculate the mixture fraction, two equations for its mean and variance are solved. The transport equation for mean mixture fraction is as follows

$$\frac{\partial}{\partial t}(\rho \bar{f}) + \nabla \cdot (\rho \vec{v} \bar{f}) = \nabla \cdot (\frac{\mu_\mathrm{t}}{\sigma_\mathrm{t}} \nabla \bar{f}) + S_\mathrm{m}, \tag{4.15}$$

where S_m is the source term for mass transfer from the liquid fuel to the gas phase.

For the mixture fraction variance, $\overline{f'^2}$, the following conservation equation is solved

$$\frac{\partial}{\partial t}(\rho\overline{f'^2}) + \nabla\cdot(\rho\vec{v}\overline{f'^2}) = \nabla\cdot(\frac{\mu_\mathrm{t}}{\sigma_\mathrm{t}}\nabla\overline{f'^2}) + C_\mathrm{g}\mu_\mathrm{t}(\nabla\bar{f})^2 - C_\mathrm{d}\rho\frac{\varepsilon}{k}\overline{f'^2}, \tag{4.16}$$

where the constants σ_t, C_g and C_d take the values of 0.85, 2.86 and 2.0, respectively [26].

Under the assumption of equilibrium chemistry for a non adiabatic combustion case (e.g. liquid fuel combustion)

$$\phi_i = \phi_i(f, H) \tag{4.17}$$

where ϕ_i represents instantaneous mass fraction, density or temperature and H is the instantaneous enthalpy defined in Chapter 2.

In turbulent flows, the average values of variables are calculated (Equations 4.15 and 4.16). To correlate these values to instantaneous values, the presumed probability density function (PDF) approach is selected in this work because of its simplicity [23, 71].

Using mixture fraction PDF $p(f)$, the mean value of species mass fraction, density and temperature can be calculated by

$$\bar{\phi}_i = \int_0^1 p(f)\phi_i(f)df. \tag{4.18}$$

A $\beta-$function PDF is employed here because of its flexibility (see Figure 4.2) and the ability to closely represent experimental PDFs [23, 27, 72].

The beta PDF shape is given by the following function of $\bar{f}$ and $\overline{f'^2}$

$$p(f) = \frac{f^{\alpha-1}(1-f)^{\beta-1}}{\int f^{\alpha-1}(1-f)^{\beta-1}df}, \tag{4.19}$$

where

$$\alpha = \bar{f}\left[\frac{\bar{f}(1-\bar{f})}{\overline{f'^2}} - 1\right] \tag{4.20}$$

and

$$\beta = (1-\bar{f})\left[\frac{\bar{f}(1-\bar{f})}{\overline{f'^2}} - 1\right]. \tag{4.21}$$

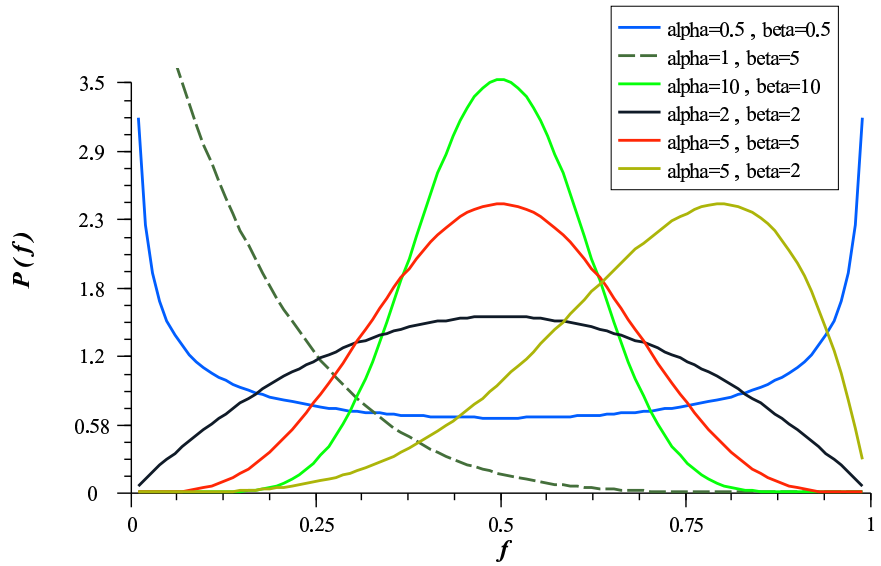

Figure 4.2: Shape of beta PDF for different sets of parameters α and β

4.3 Flamelet Model

In turbulent flows, the local micromixing rate (i.e. the instantaneous scalar dissipation rate χ in Equation 4.22) is a random variable. Thus, while the chemistry may be fast relative to the mean micromixing rate, at some points in the flow the instantaneous micromixing rate may be fast compared with the chemistry [72]. The effects caused by the fluctuation in micromixing rate can be modeled using the laminar flamelet concept.

The flamelet concept views the turbulent diffusion flame as an ensemble of thin, laminar, locally one-dimensional flamelet structures embedded within the turbulent flow field [27, 73]. Commonly a counterflow laminar diffusion flame is used to represent the flamelet in a turbulent flow. As the name suggests, the counterflow diffusion flame consists of opposed, axisymmetric oxidizer and fuel jets (Figure 4.3).

The scalar dissipation rate, characterizing the departure from equilibrium, is defined as

$$\chi = 2D|\nabla f|^2 \tag{4.22}$$

with D being the diffusivity. The scalar dissipation rate accounts for non-equilibrium effects caused by both convection and diffusion. Its relation with the strain rate a is presented in [74].

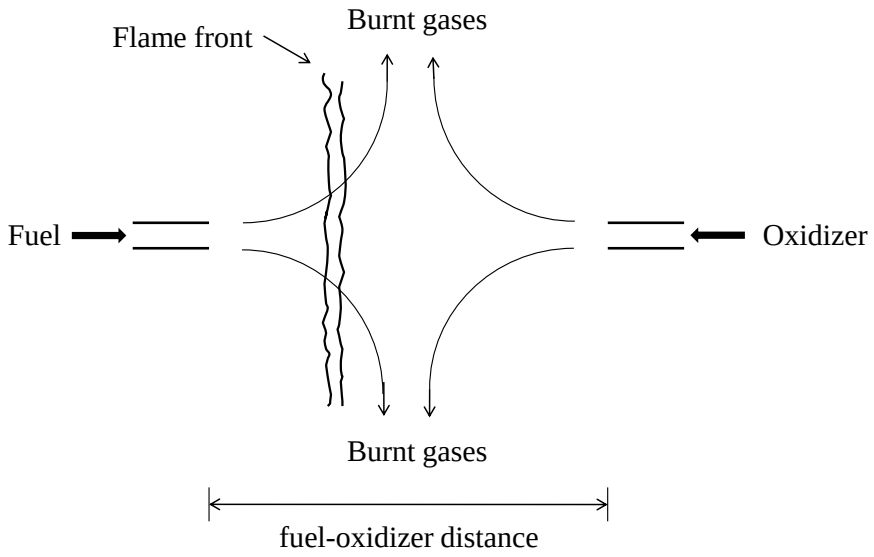

Figure 4.3: Laminar counterflow nonpremixed flame (adapted from [23])

For counterflow diffusion flames, the characteristic strain rate is defined as $a = v/2d$, where v is the relative velocity of the fuel and oxidizer jet and d is the distance between jet nozzles [26].

At the position where the mixture fraction f is stoichiometric, the scalar dissipation can be calculated by [75]:

$$\chi_{\mathrm{st}} = \frac{a}{\pi} \exp\left(-2[\mathrm{erfc}^{-1}(2f_{\mathrm{st}})]^2\right) \tag{4.23}$$

where erfc^{-1} is the inverse complementary error function and f_{st} is the stoichiometric mixture fraction.

The instantaneous stoichiometric scalar dissipation χ_{st}, has a dimension of s^{-1} and may be interpreted as the inverse value of a characteristic diffusion time. In the limit where $\chi_{\mathrm{st}} \to 0$, the chemistry tends to equilibrium. The increase in χ_{st} due to aerodynamic straining increases non-equilibrium.

To account for the effect of variable density across the flamelet, the following equation is solved as an extension of the above equation [76]:

$$\chi(f) = \frac{a}{4\pi} \frac{3(\sqrt{\rho_\infty/\rho}+1)^2}{2\sqrt{\rho_\infty/\rho}+1} \exp\left(-2[\mathrm{erfc}^{-1}(2f)]^2\right) \tag{4.24}$$

where ρ_∞ is the density of the oxidizer stream.

In order to model the laminar counter flow diffusion flame, the equations are transformed from the physical space to the mixture fraction space [26]. Here a simplified set of equations is solved [75]:

$$\rho\frac{\partial Y_i}{\partial t} = \frac{1}{2}\rho\chi\frac{\partial^2 Y_i}{\partial f^2} + S_i \tag{4.25}$$

where Y_i and S_i are the mass fraction and reaction rate of species i, respectively. The first term in the right hand side of the equation takes the effect of instantaneous micro mixing into account. Generally, near the stoichiometric surface, both terms in the right hand side of the above equation are large in magnitude and opposite in sign [27]. A quasi-stationary state is then quickly reached, wherein the accumulation term on the left hand side is negligible. The stationary laminar flamelet (SLF) model is found by simply neglecting the accumulation term in Equation 4.25. The SLF model can be used, yielding good results, for the prediction of heat release, concentration of major chemical components and even OH concentrations [77].

The following equation is solved for the temperature

$$\rho\frac{\partial T}{\partial t} = \frac{1}{2}\rho\chi\frac{\partial^2 T}{\partial f^2} - \frac{1}{c_\mathrm{p}}\sum_i H_i S_i + \frac{1}{2c_\mathrm{p}}\rho\chi\left[\frac{\partial c_\mathrm{p}}{\partial f} + \sum_i c_{\mathrm{p},i}\frac{\partial Y_i}{\partial f}\right]\frac{\partial T}{\partial f} \tag{4.26}$$

where $c_{\mathrm{p},i}$ and c_p are the i^{th} species specific heat and mixture averaged specific heat, respectively.

The turbulent flame is modeled as an ensemble of discrete laminar flamelets. Since in adiabatic cases the species mass fractions and temperature are functions of only mixture fraction f and scalar dissipation χ_st, the mean values of these parameters can be determined from the PDF of f and χ_st as

$$\bar{\phi}_i = \int_0^\infty \int_0^1 p(f,\chi_\mathrm{st})\phi_i(f,\chi_\mathrm{st})df d\chi_\mathrm{st}. \tag{4.27}$$

In this study, f and χ_st are assumed to be statistically independent, so the joint PDF $p(f,\chi_\mathrm{st})$ can be simplified as $p_f(f)p_\chi(\chi_\mathrm{st})$. A $\beta-$function PDF is considered for mixture fraction as discussed in section 4.2. For the sake of simplicity, the fluctuations in χ_st are ignored and a delta function is used [26].

$$p_\chi = \delta(\chi_\mathrm{st} - \overline{\chi_\mathrm{st}}) \tag{4.28}$$

where the mean scalar dissipation, $\overline{\chi_\mathrm{st}}$, is modeled as [75]

$$\overline{\chi_{\mathrm{st}}} = 2\frac{\varepsilon}{k}\overline{f'^2}. \tag{4.29}$$

The integration of Equation 4.27 is preprocessed and stored in look-up tables.

For non-adiabatic steady laminar flamelets, the additional parameter of enthalpy is required. However, the computational cost of modeling steady flamelets over a range of enthalpies are prohibitive, so some approximations are made [26]. Heat gain/loss to the system is assumed to have a negligible effect on the species mass fractions, and adiabatic mass fractions are used [78]. This approximation is not applied for the case corresponding to a scalar dissipation of zero. Such a case is modeled by equilibrium chemistry assumption discussed in section 4.2.

4.4 Eddy Dissipation Concept

The Eddy Dissipation Concept (EDC) model [79] can consider detailed chemical reaction mechanisms in turbulent reactive flow simulations. It is an extension of the Eddy Dissipation Model [80]. The basic idea behind EDC is that the reactions occur in regions where the dissipation of turbulence energy takes place. These regions occupy a small fraction of the flow. The small turbulent structures (the so called fine structures) have a characteristic dimensions in the Kolmogorov length scale order in one and two dimensions [81]. The Kolmogorov scales are the smallest scales of turbulent motion with a length scale of [82]

$$\eta_{\mathrm{k}} = \left(\frac{\nu^3}{\varepsilon}\right)^{1/4}, \tag{4.30}$$

and a time scale of

$$\tau_\eta = \left(\frac{\nu}{\varepsilon}\right)^{1/2}. \tag{4.31}$$

The length fraction of the fine structures is defined by

$$\xi^* = 2.1377\left(\frac{\nu\varepsilon}{k^2}\right)^{1/4}. \tag{4.32}$$

The fraction of the flow occupied by the fine structures is modeled as $(\xi^*)^3$. The time scale over which the reactions take place, is calculated as

$$\tau^* = 0.4082\left(\frac{\nu}{\varepsilon}\right)^{1/2}. \tag{4.33}$$

The combustion at fine scales is assumed to occur as a constant pressure homogeneous reactor, with initial conditions taken as the current species and temperature in the cell [26] and a residence time τ^*. The reactions, governed by Arrhenius rates, are solved numerically using ISAT algorithm (see section 5.3). The source term R_i for the i^{th} species conservation equation (Equation 2.12) is then calculated by

$$R_i = \frac{\rho(\xi^*)^2}{\tau^*[1-(\xi^*)^3]}(Y_i^* - Y_i) \tag{4.34}$$

where superscript $*$ denotes fine scale quantities. In the above equation, the mass exchange between the fine structures and the surroundings is modeled as $(\xi^*)^2/\tau^*$ [83]. The factor $1/[1-(\xi^*)^3]$ comes from the corresponding equation for the mass averaged mean state as discussed in detail in [81].

Typical chemical reaction mechanisms contain tens of species in hundreds of reactions. The ordinary differential equation system governing the combustion process is normally stiff and its numerical solution is computationally costly and often unstable [23]. Therefore, simulating detailed chemical reaction schemes using the EDC model needs more computational resources than equilibrium chemistry or the flamelet model. Efficient numerical procedures are hence required to decrease the computational resources required to treat the detailed chemistry using EDC. In this thesis, the EDC model is used in conjunction with ISAT procedure.

5. Numerical Models

In order to perform a CFD simulation, the governing equations and models discussed earlier need to be transferred to a numerical domain. In the numerical domain, the governing equations are discretized and solved by computer programs. Appropriate numerical algorithms are required. The method used in this study is based on the Finite Volume method which will be discussed in the next section. At the end of the chapter the ISAT algorithm used to accelerate chemistry calculations will be introduced.

5.1 Finite Volume Method

Fluid dynamics is governed by partial differential equations already discussed in Chapter 2. There are a number of different methods to solve them numerically. Finite difference, finite volume and finite element methods are among those used in the literature. In the finite difference approach, the derivatives are written in finite difference form using truncated Taylor series expansions resulting in coupled algebraic equations [84]. The mesh configurations for this method must be structured [85]. In the finite element method, some form of weighted residual of the governing equations is minimized over each finite element [84]. The underlying principles and formulations in finite element methods require mathematical rigor and are described in detail in [86]. Both finite difference and finite element methods do not explicitly enforce the conservation principle in their original forms. Hence, the mesh should be fine enough for a correct numerical solution of the CFD problem [84]. The finite volume method, on the other hand, uses an integral representation of the conservation equations to develop the algebraic equations. This method guarantees the

conservation properties throughout the domain and needs no coordinate transformations for unstructured meshes and complex geometries [85]. Finite volume and finite difference methods are shown to be the predominant methods in engineering applications [87] although a fair comparison between the methods is difficult.

The Finite Volume Method is used in the frame of this work to solve the governing equations describing the continuous phase. The integral form of these equations are discretized. In this method, the whole computational domain is subdivided into a set of non-overlapping cells called control volumes (CV). The governing equations are then applied to each of the control volumes to determine the flow variables in the cells.

The velocity field is obtained from the momentum equation. A pressure based approach is used here which calculates the pressure by solving a pressure or a pressure correction equation obtained by manipulating continuity and momentum equations [26]. This type of solver and the discretization of the equations are discussed in the subsections that follow.

5.1.1 Pressure Based Solver

The pressure based solution method is a particular form of a more general method called Projection Method [88]. In this method a pressure equation is derived from the continuity and the momentum equations in such a way that the velocity field satisfies the continuity [26]. This method has often been used in the literature to solve the governing Navier-Stokes equations ([89, 90, 91]). Due to the nonlinearity of the equations, an iterative solution method is required.

The pressure based methods for solving incompressible flows have been the method of choice in the last decades [92]. The segregated pressure based solver is used in this study in which the equations are solved sequentially. The solution procedure for each iteration, outlined in Figure 5.1, is as follows:

1. The fluid properties are updated based on current available solution.
2. The momentum equations are solved sequentially using updated values of pressure and mass fluxes.
3. The pressure-correction equation is solved using the results of step 2.
4. The values of pressure, velocity field and mass fluxes are updated.
5. The equation for additional scalars such as energy, species, turbulence and radiation are solved.

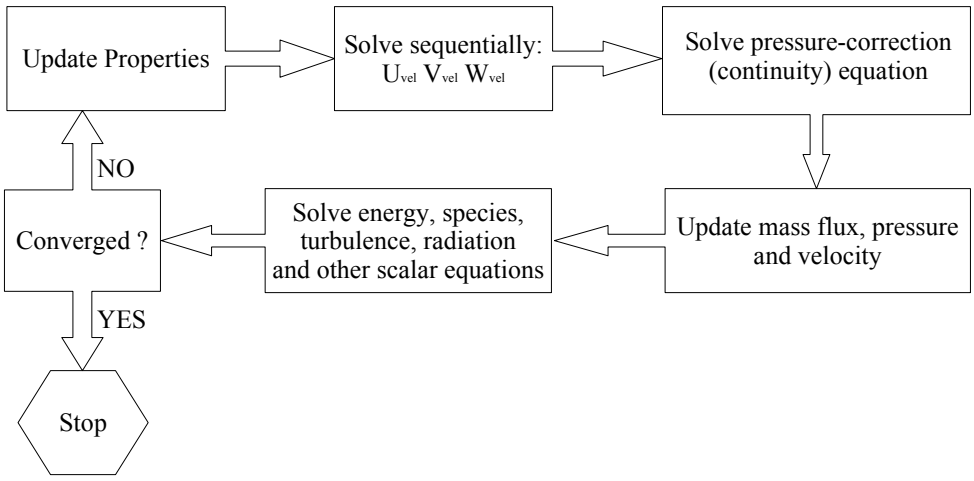

Figure 5.1: Pressure based segregated solver

6. The source terms arising from interactions with discrete phase are updated.

7. Convergence is checked.

For the first iteration, the initial conditions defined for the fluid properties are used and the above mentioned procedure starts from the step 2. The iteration continues until the convergence is obtained.

The segregated algorithm (in which the equations are solved in a decoupled manner) is memory efficient, because it stores the discretized equations in the memory one at a time. However, the solution convergence is relatively slow, inasmuch as the equations are solved in a decoupled manner [26, 92].

5.1.2 Discretization of Equations

Consider the differential equation for the transport of the scalar quantity ϕ. This equation can be written in integral form for a control volume V as

$$\int_V \frac{\partial \rho\phi}{\partial t}\,\mathrm{d}V + \oint \rho\phi\vec{v}\cdot\mathrm{d}\vec{A} = \oint \Gamma_\phi \nabla\phi\cdot\mathrm{d}\vec{A} + \int_V S_\phi\,\mathrm{d}V \tag{5.1}$$

where Γ_ϕ is the diffusion coefficient for ϕ and S_ϕ indicates the source of ϕ per unit volume. Discretization and integration of the above equation on the control volume results in the following equation:

$$\frac{\partial \rho\phi}{\partial t}V + \sum_f^{N_{\text{faces}}} \rho_f\vec{v}_f\phi_f\cdot\vec{A}_f = \sum_f^{N_{\text{faces}}} \Gamma_\phi\nabla\phi_f\cdot\vec{A}_f + S_\phi V \tag{5.2}$$

where N_{faces} is the number of faces enclosing the cell and ϕ_f is the amount of ϕ convected through the face.

For the steady state case considered in this study, $\frac{\partial \rho \phi}{\partial t} V = 0$, and no temporal discretization is required. Equation 5.2 can then be written in the form

$$\sum_f J_f \phi_f = \sum_f D_f + S_\phi V \tag{5.3}$$

where J_f is the mass flow rate and D_f shows the transport due to the diffusion through the face f. The mass flow rate is defined from the solution of continuity and momentum equations.

The face value of the scalar ϕ is calculated using a First-Order Upwind scheme indicating that the face value ϕ_f is equal to the cell value of the scalar of the upstream cell. Hence,

$$\phi_f = \phi_{upwind} \tag{5.4}$$

One needs to determine the gradient $\nabla \phi$ of the scalar ϕ not only to calculate velocity derivatives, but also the secondary diffusion terms. Calculation of the gradients is based on the divergence theorem stating that the gradient of ϕ at the cell center is defined as

$$(\nabla \phi)_0 = \frac{1}{V} \sum_f \bar{\phi}_f \vec{A}_f \tag{5.5}$$

where the summation is over all the faces of the cell and the face value of ϕ is obtained by arithmetic averaging at the neighboring cell

$$\bar{\phi}_f = \frac{\phi_0 + \phi_1}{2} \tag{5.6}$$

The discretization procedure yields a linearized form of the Equation 5.2 for ϕ at the cell center in the form

$$a_p \phi_p = \sum_{nb} a_{nb} \phi_{nb} + b_p \tag{5.7}$$

where the subscript nb indicates the neighbor cells and a is the linearized coefficient for ϕ. Here the summation is over all the neighbors nb of cell p. Similar equations

in the form of the above equation have to be written for all the cells in the domain. The system of equations is solved using a Gauss-Seidel linear equation solver [87] in conjunction with an algebraic multi grid (AMG) method discussed in detail in [87], [93] and [94].

By setting $\phi = u$, one can obtain the discretized equation for momentum in the same manner as discussed above. The equation has the form

$$a_p u = \sum_{nb} a_{nb} u_{nb} + \sum p_f A \cdot \hat{i} + S \tag{5.8}$$

and the discrete continuity equation is written as

$$\sum_{f}^{N_{faces}} J_f A_f = 0 \tag{5.9}$$

Both velocity and pressure components are stored at cell centers. Computing J_f by averaging the cell velocities causes checker boarding [92]. This can be avoided by using a scheme similar to that proposed in [95, 96]. A momentum-weighted averaging is used with weighting factors based on the a_p coefficient from Equation 5.8. The mass flow rate can then be written as

$$J_f = \rho_f \frac{a_{p,0} v_{n,0} + a_{p,1} v_{n,1}}{a_{p,0} + a_{p,1}} + d_f \left[(p_0 + (\nabla p)_0 . \vec{r_0}) - (p_1 + (\nabla p)_1 . \vec{r_1}) \right] = \hat{J}_f + d_f (p_0 - p_1) \tag{5.10}$$

where $p_0, p_1, v_{n,0}$ and $v_{n,1}$ are the pressure and normal velocity, respectively, of the cells at both sides of each face. The term d_f is a function of $\bar{a}_p$, the average of the momentum equation coefficients for the cells on either side of the face.

5.1.3 Pressure Velocity Coupling

Pressure velocity coupling is accomplished by using the Equation 5.10 to achieve a formulation for pressure through manipulating the continuity equation. This is achieved by using an algorithm called Semi-Implicit Method for Pressure-Linked Equations (SIMPLE) [95]. The algorithm is based on the finite volume discretization on the staggered grids employed by the present work. It describes the iterative procedure by which the solutions of the discretized equations are obtained.

For an arbitrary pressure p^*, the mass flow rate obtained from Equation 5.10 is written as

$$J_f^* = \hat{J}_f^* + d_f(p_0^* - p_1^*) \tag{5.11}$$

which, in general does not satisfy the continuity equation. To solve this, a term J' is added in the form

$$J_f' = d_f(p_0' - p_1') \tag{5.12}$$

so that the resulting mass flux

$$J_f = J_f^* + J_f' \tag{5.13}$$

satisfies the continuity. p' is called cell pressure correction. The SIMPLE algorithm then substitutes the correction equation in the discretized continuity equation to obtain an equation for pressure correction in the form

$$a_p p' = \sum_{nb} a_{nb} p'_{nb} + b \tag{5.14}$$

where b is the net flow rate to the cell for the starred condition,

$$b = \sum_f J_f^* A_f. \tag{5.15}$$

If $b = 0$, the starred condition satisfies the continuity and no pressure correction is needed. Therefore the term b represents a mass source which the pressure corrections must annihilate [95].

When the pressure correction equation is solved, the values of corrected pressure and mass flux are

$$p = p^* + \alpha_p p' \tag{5.16}$$

$$J_f = J_f^* + d_f(p_0' - p_1') \tag{5.17}$$

where α_p is the relaxation factor for pressure having a value between 0 and 1.

A relaxation method is used to accelerate the convergence. Large change in the variables could cause numerical instability. Therefore, the variable ϕ is changed as

$$\phi = \phi_{old} + \alpha_\phi \Delta\phi. \tag{5.18}$$

The SIMPLE procedure can be summarized in the following steps:

1. Guess the pressure p^*.
2. Solve Equation 5.11 for starred velocities.
3. Solve p' equation (Equation 5.14).
4. Calculate p from Equation 5.16.
5. Calculate the velocity field from Equation 5.17.
6. Treat the corrected pressure p as a new guess p^*, return to step 2 and repeat until convergence.

One can use the mass source b as a useful indicator of the flow solution convergence. The iterations should be continued until the value of b becomes sufficiently small everywhere.

5.2 Integration of Particle Equation of Motion

As already discussed in section 3.3, the particle velocity is calculated by integrating Equation 3.31 and the trajectory is calculated by solving Equation 3.41. Rearranging Equation 3.31 to a general form, one obtains:

$$\frac{du_p}{dt} = \frac{1}{\tau_p}(u - u_p) + a \tag{5.19}$$

where a is the acceleration due to all forces other than the drag force.

Two numerical discretization schemes are used here to solve Equation 5.19 numerically. Using Euler implicit discretization, one obtains

$$u_p^{n+1} = \frac{u_p^n + \Delta t \left(a + \frac{u^n}{\tau_p}\right)}{1 + \frac{\Delta t}{\tau_p}}. \tag{5.20}$$

When applying a trapezoidal discretization to Equation 5.19, the variables u and u_p on the right hand side are taken as averages, and a as a constant. The solution will then be as follows:

$$\frac{u_p^{n+1} - u_p^n}{\Delta t} = \frac{1}{\tau_p}(u^* - u_p^*) + a \tag{5.21}$$

where

$$\begin{aligned} u^* &= \frac{1}{2}(u^{n+1} + u^n) \\ u_p^* &= \frac{1}{2}(u_p^{n+1} + u_p^n) \\ u^{n+1} &= u^n + \Delta t u_p^n . \nabla u^n \end{aligned} \tag{5.22}$$

Combining equations 5.21 and 5.22, the particle velocity at the new location $n+1$ is computed by

$$u_p^{n+1} = \frac{u_p^n(1 - \frac{1}{2}\frac{\Delta t}{\tau_p}) + \frac{\Delta t}{\tau_p}(u^n + \frac{1}{2}\Delta t u_p^n . \nabla u^n) + a\Delta t}{1 + \frac{1}{2}\frac{\Delta t}{\tau_p}}. \tag{5.23}$$

Using trapezoidal discretization of the Equation 3.41, the trajectory of the particle is calculated as

$$x_p^{n+1} = x_p^n + \frac{1}{2}\Delta t(u_p^{n+1} + u_p^n). \tag{5.24}$$

A combination of the implicit and trapezoidal schemes is used in ANSYS FLUENT and hence in this study as well. In situations where the particle is far from hydrodynamic equilibrium, a trapezoidal scheme produces better solution, whereas when the particle reaches hydrodynamic equilibrium, the higher order trapezoidal schemes become inefficient and the mechanism switches to a stable implicit scheme [26].

5.3 In Situ Adaptive Tabulation

As discussed in chapter 4, detailed chemical models typically include reactants, products and reaction intermediates that sum up to tens of species resulting from hundreds of reactions. The corresponding reaction timescales can range from $10^{-10}s$ to more than $1s$ [23]. Reaction schemes with a wide range of timescales produce a stiff numerical system that is difficult to integrate.

For the reaction fractional step in the EDC model (see section 4.4), each particle evolves according to the chemical source term:

$$\frac{d\phi^{(i)}}{dt} = S(\phi^{(i)}) \tag{5.25}$$

where ϕ is the particle composition vector

$$\phi = (Y_1, Y_2, ..., Y_N, T) \tag{5.26}$$

with Y_k being the k^{th} species mass fraction.

Direct Integration (DI) of the above differential equations is computationally expensive for detailed reaction schemes. To circumvent the cost of DI, the In Situ Adaptive Tabulation (ISAT) algorithm [97] is used in this study.

ISAT is a powerful tool that enables realistic chemistry to be incorporated in multi-dimensional flow simulations by accelerating the chemistry calculations. In full, the method is: in situ, unstructured, adaptive tabulation of the accessed region with control of retrieval errors [97].

In order to use a tabulation method for a particular flow, it is sufficient to tabulate the accessed domain, rather than the whole of the realizable domain which is much larger. Since the accessed domain depends on many aspects of the flow including the kinetics, the transport processes and the boundary conditions, it is not known before performing the calculation. Hence, the table is built up during the reactive flow calculation. Each entry in the table corresponds to a composition that occurs in a cell during the calculation and the corresponding $S(\phi^{(i)})$. This is referred to as *in situ* tabulation.

The basic idea behind ISAT method is to integrate the governing equation using DI and then store the reaction mapping as well as sensitivity information in a binary tree data structure for later use [98]. For subsequent calculations, DI is avoided for the points that are within a small defined distance from previously calculated points. Here, the reaction mapping will be estimated using multi linear interpolation [98]. However, DI will be performed where the reaction mapping can not be interpolated with sufficient accuracy. This idea is depicted in Figure 5.2 and summarized as follows:

- On subsequent call the table is queried.
- Check if the initial state falls inside Ellipsoid Of Accuracy (EOA).
- If yes, interpolate and retrieve the mapping.
- If not, a Direct Integration is performed.
- Check if the mapping falls within ISAT error tolerance.

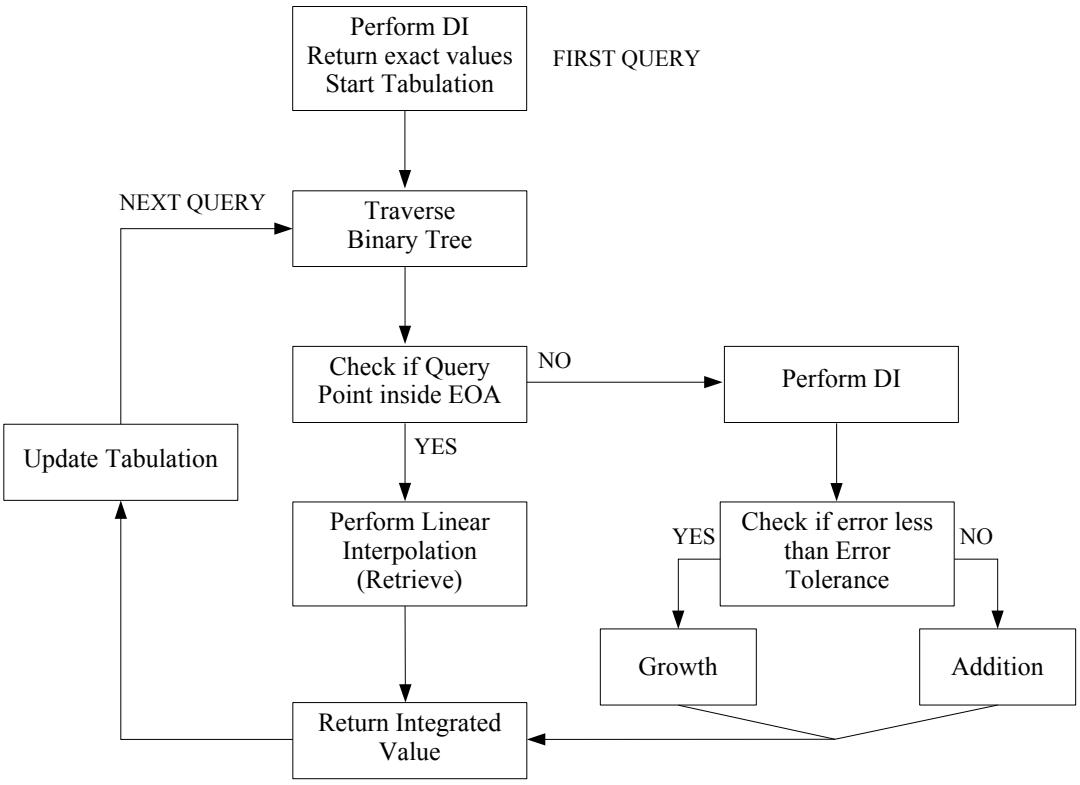

Figure 5.2: Key steps involved in ISAT algorithm [98]

- If yes, the EOA is grown.
- If not, a new table entry is added.

At the start of the simulation, most operations are "Addition" and "Growth" which are slow due to performing DI. Later, as more points in the composition space are tabulated, "Retrieve" becomes frequent and hence the CFD calculation will be accelerated. Typical speed-up factor of 100-1000 is obtained compared to DI [97], [98].

6. Results and Discussion

This chapter focuses on the CFD simulation results of the gasification of ethylene glycol which was used as a model fuel for pyrolysis oil in the lab-scale entrained flow gasifier REGA. The gasifier and the gasification conditions are described in section 6.1 of this chapter. The physical, chemical and numerical models discussed in previous chapters are utilized to perform CFD simulations using the ANSYS FLUENT 12.0 code. The resulted flow patterns, temperature profiles and product gas compositions are presented and compared with experimental measurements wherever possible. The results are presented in sections 6.2 and 6.3.

In section 6.4, a series of simulations is performed to study the effect of the boundary and operating conditions on the gasification efficiency and the product gas compositions. Oxidizer and fuel inlet temperatures, oxidizer composition, air-fuel ratio, and the gasifier operating pressure are the four variables used for sensitivity analyses.

Section 6.5 is dedicated to study the effect of chemistry on the gasification process. In the first part, three versions of the ethylene glycol reaction mechanism are used to study the effect of reaction kinetics on the gasification. In the second part, the chemistry models discussed in chapter 4, namely equilibrium chemistry, flamelet model and eddy dissipation concept are compared with each other and their effects on the simulation results are discussed.

At the end of this chapter simulation results of the slurry gasification are presented with a focus on the effect of char gasification on the whole process.

6.1 Gasifier Model and Simulation Conditions

The modeled gasifier in this thesis is a pilot scale Research Entrained Flow Gasifier (REGA) which is operated at the Karlsruhe Institute of Technology (KIT). It is a 60 kW atmospheric entrained flow gasifier having a total length of 3 m and an inner diameter of 28 cm. It is equipped with an external mixing burner nozzle for atomization of slurries with air [99]. Fuel and oxidizer enter the gasifier at the top through the burner and the hot product gases exit at the bottom of the gasifier as depicted in Figure 6.1. The electrical heating of the reactor walls up to 1200 °C allows adiabatic operating conditions [22].

In this study, ethylene glycol ($HOCH_2CH_2OH$) serves as non-toxic model fuel for pyrolysis oil, mainly because of its similar C/H/O-ratio and its similar physical properties to biomass derived liquid pyrolysis products [99, 100].

The ethylene glycol oxidization reaction mechanism, developed by Hafner [64, 66], was simplified using the methods and softwares discussed in section 4.1. The current reduced version of the reaction mechanism comprises of 43 chemical species and 629 elementary reactions (see Appendix A.2). The analysis of the mechanism for stoichiometric, fuel-rich and fuel-lean cases, using HOMREA and MIXFLA packages, showed that the concentrations of major species in the reduced mechanism deviate by less than 2% from the corresponding values of the original mechanism. Hence, using the simplified reaction mechanism does not introduce significant errors in the reactive flow CFD calculation. The reduced mechanism will thus be used in the context of this thesis.

A 2D axisymmetric geometry was used due to the available symmetry of the REGA. A structured quadratic element grid with *Successive Ratio* scheme was generated. This scheme is a non-symmetric scheme, in which the cell size increases in both radial and axial directions from the burner. The grid nodes generated for the top cap of the REGA using the successive ratio scheme can be seen in Figure 6.2. The gasifier mesh was generated using GAMBIT software and consisted of 17612 cells.

The CFD simulations are performed using ANSYS FLUENT 12.0 software. To check the generated mesh, a cold flow simulation was performed in which air at T_a=300 K and a volume flow rate of 17.41 m^3/h was injected and the axial velocity along the axis of symmetry of the gasifier was compared with measured values. Due to the turbulent nature of the flow, the realizable k-ε model was used. The experimental data were derived by KIT using a propeller anemometer and Laser Doppler Anemometer (LDA) [100, 101]. Figure 6.3 shows a comparison of the simulated axial velocity of

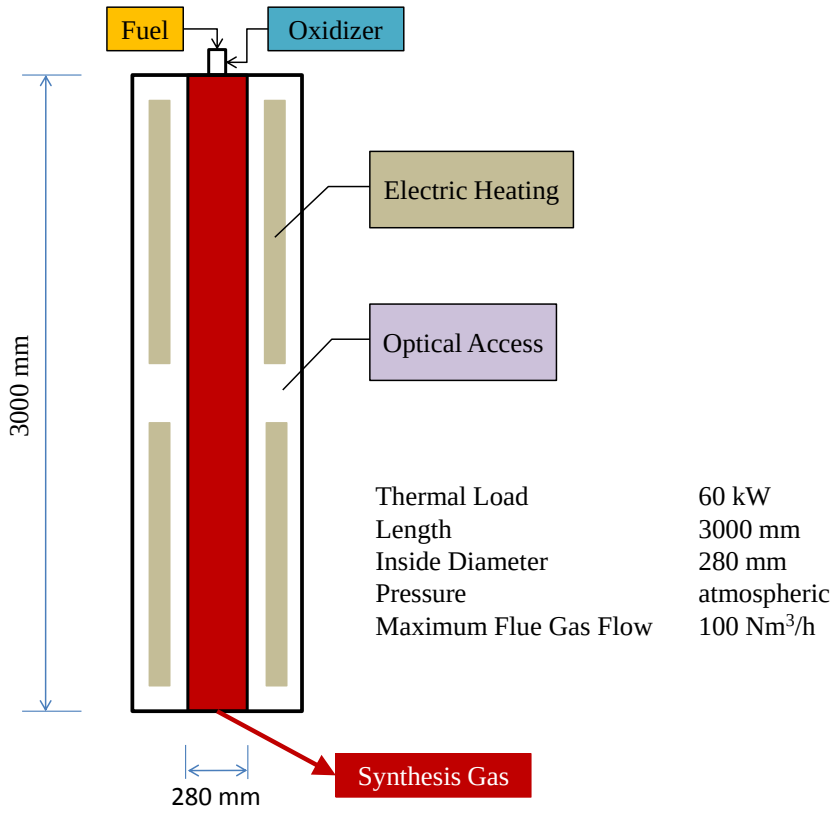

Figure 6.1: The simulated entrained flow gasifier

the air along the symmetry axis of the REGA with the two measurement methods. The simulation results showed agood agreement with experimental values.

The mesh was also used for the hot reactive flow simulations. The turbulence-chemistry interactions were taken into account by using the EDC model (section 4.4). The EDC model was employed together with the ISAT algorithm (section 5.3) to dynamically tabulate the chemistry mapping and to reduce the time to solution. The Discrete Phase Model (section 3.3) together with the Discrete Ordinates model (section 3.2) were used to model the liquid phase and radiation heat transfer, respectively.

ANSYS FLUENT applies the finite volume method (section 5.1) to solve the governing equations numerically. Here, a first-order-upwind scheme was applied for interpolation within a pressure-based implicit solver. The SIMPLE procedure was employed for pressure velocity coupling.

For the reactive flow simulation, a case was considered in which ethylene glycol was injected at a flow rate of 9.5 kg/h and gasified under fuel rich condition ($\lambda = 0.43$). The oxidizing agent was a mixture of air and pure oxygen. The enriched air contained 40 % vol oxygen (Case C1 in Table 6.2). The gasifier wall was kept at a constant temperature of 1373 K.

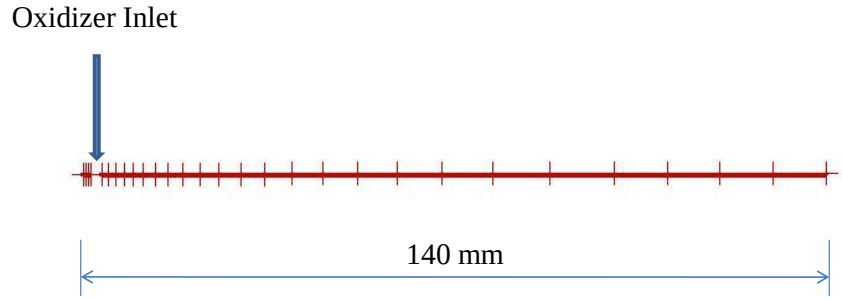

Figure 6.2: Grid nodes generated on the top cap using 'Successive Ratio Scheme'

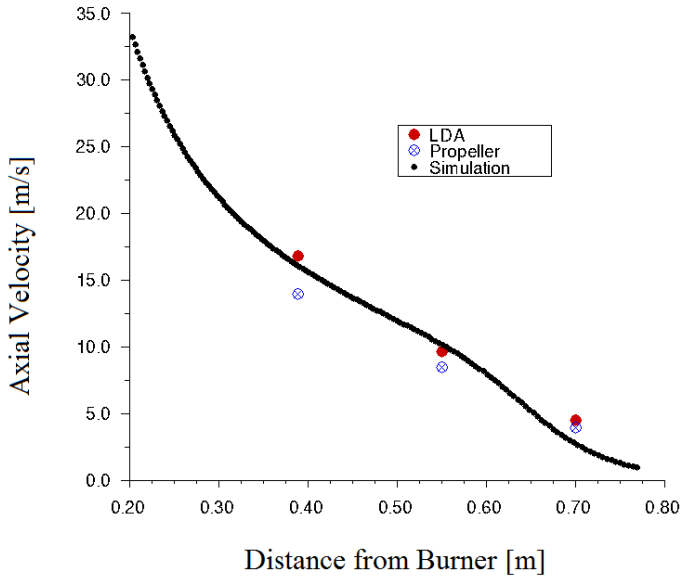

Figure 6.3: Axial velocity along the symmetry axis of the gasifier
LDA and Propeller are experimental values [101]

6.2 Flow Pattern

Figure 6.4 shows the contours of the gas velocity, the streamlines and the droplet trajectories for the top 1 m of the gasifier. In the middle plot, one can see the recirculation zone that is formed around the centerline of the gasifier. From the middle part of the gasifier to the outlet, the flow pattern turns to a uniform turbulent plug flow profile. Ethylene glycol droplets are vaporized quickly due to the high temperature inside the gasifier and do not enter the recirculation zone, as can be seen in Figure 6.4.c. The *random* shape of the droplet trajectories is due to a tracking model of ANSYS FLUENT (the DRW model was used in this thesis) that was used to better describe their turbulent and stochastic nature. In essence, the particles are not expected to follow the same geometrical routes every time they are injected into the flow field, they rather follow a scattered (around a time-mean path) route which

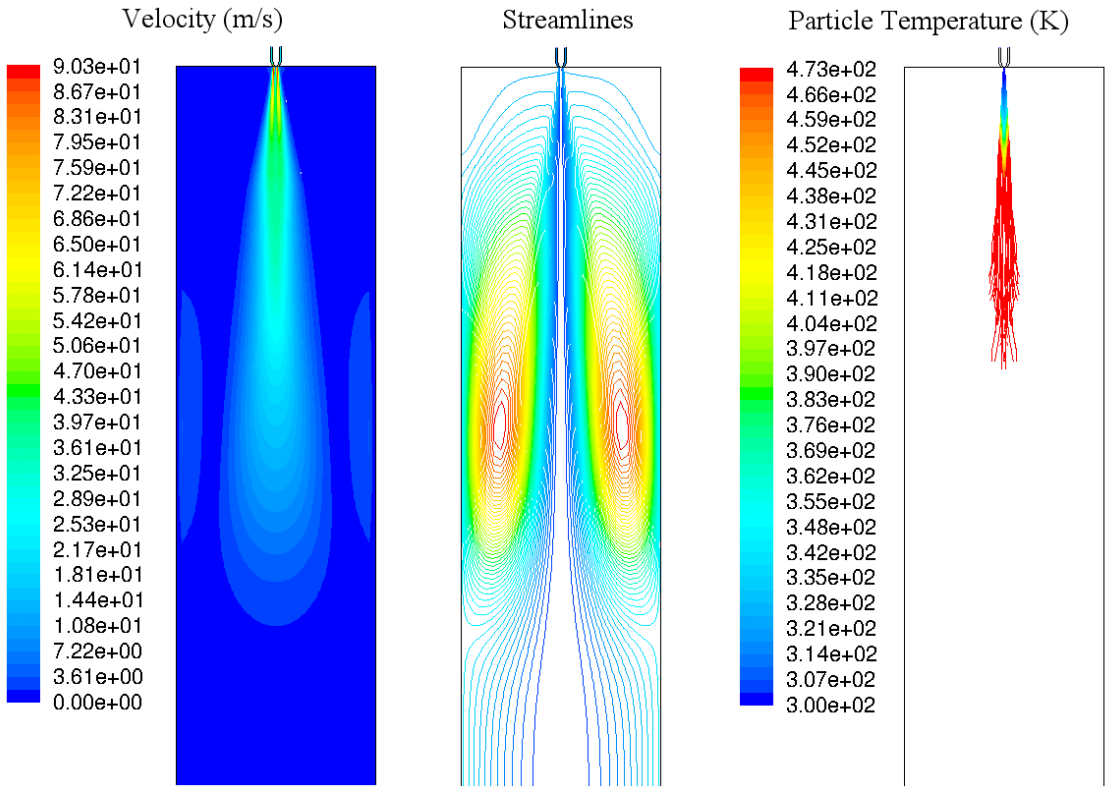

Figure 6.4: Gas velocity (left), streamlines (middle), and droplet temperature (right) for the top 1 meter of the gasifier

is set by a random number generator determined by the local turbulence levels as discussed in section 3.3.

The molecular viscosity of the gases was calculated using the Sutherland viscosity law [102], based on kinetic theory of ideal gases and an idealized intermolecular-force potential, as

$$\mu = \mu_0 \frac{T_0 + C}{T + C} \left(\frac{T}{T_0} \right)^{3/2}, \tag{6.1}$$

where μ_0 and T_0 are the reference values of viscosity and temperature, respectively, and C is the Sutherland constant. The values of μ_0, T_0 and C for different relevant chemical species are derived from [103].

In Figure 6.5, the contours of viscosity and gas temperature on the top third of the gasifier are presented. As can be seen, the molecular viscosity and the temperature have a similar profile due to the temperature dependence of viscosity according to the Sutherland law.

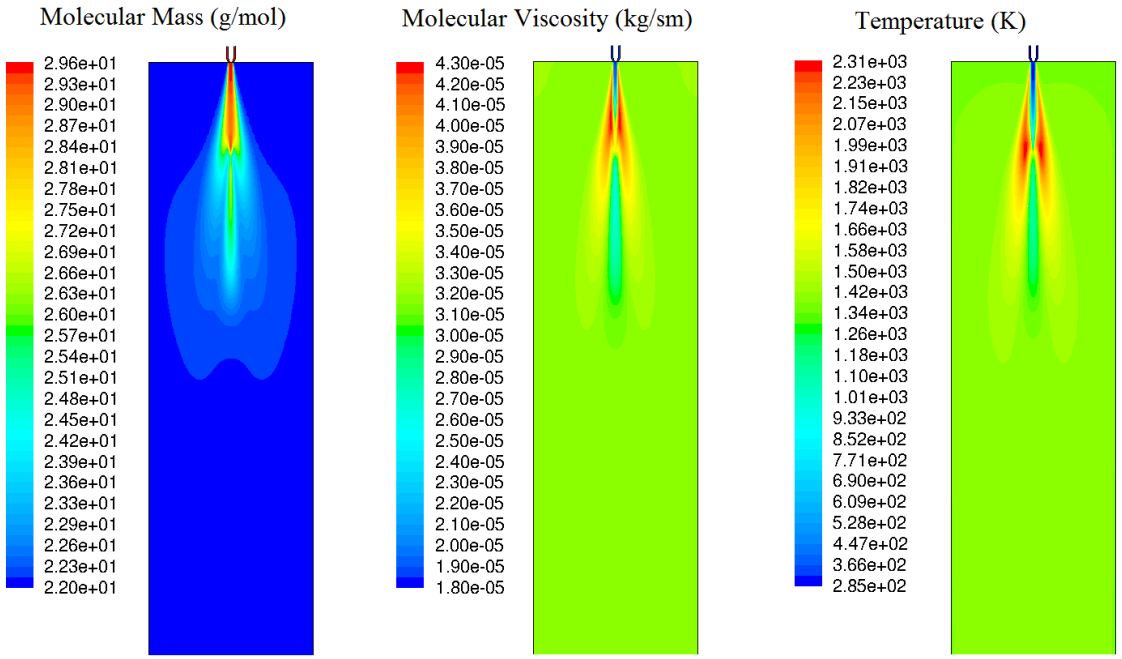

Figure 6.5: Molecular mass, molecular viscosity and temperature of the gas for the top 1 meter of the gasifier

6.3 Temperature and Species Concentrations

Due to the recirculation pattern shown in Figure 6.4, hot gas from the lower part of the flame will move up along the wall to the top of the gasifier. The recirculated gas is rich in reactive species (i.e. CO and H_2) and has a high temperature. Hence, it will easily be oxidized when brought in contact with the oxygen injected from the burner. This assists the flame to hold its high temperature and also the formation of regions with high temperatures close to the burner, where oxygen mixes with recirculation gas, as can be seen from the temperature contours in Figure 6.5. The maximum temperature achieved in this region is about 2310 K. Because of the plug flow nature of the flow, most of the reactor has a homogeneous temperature of about 1375 K.

Hafner et al. [66] performed a reaction flow analysis of the ethylene glycol oxidization under fuel-rich conditions in a jet stirred reactor. The main reaction path under this condition was the decomposition of ethylene glycol to acetaldehyde (CH_3CHO) with subsequent H-abstraction to acetaldehyde radical CH_3CO and finally the decomposition to CH_3 and CO. This trend can be observed in the REGA simulation as well. After the injection, liquid ethylene glycol vaporizes and enters the gas phase at an axial distance between 120-450 mm from the burner with a maximum mole fraction occurring around x = 200 mm from the injection point (see Figure 6.6). At

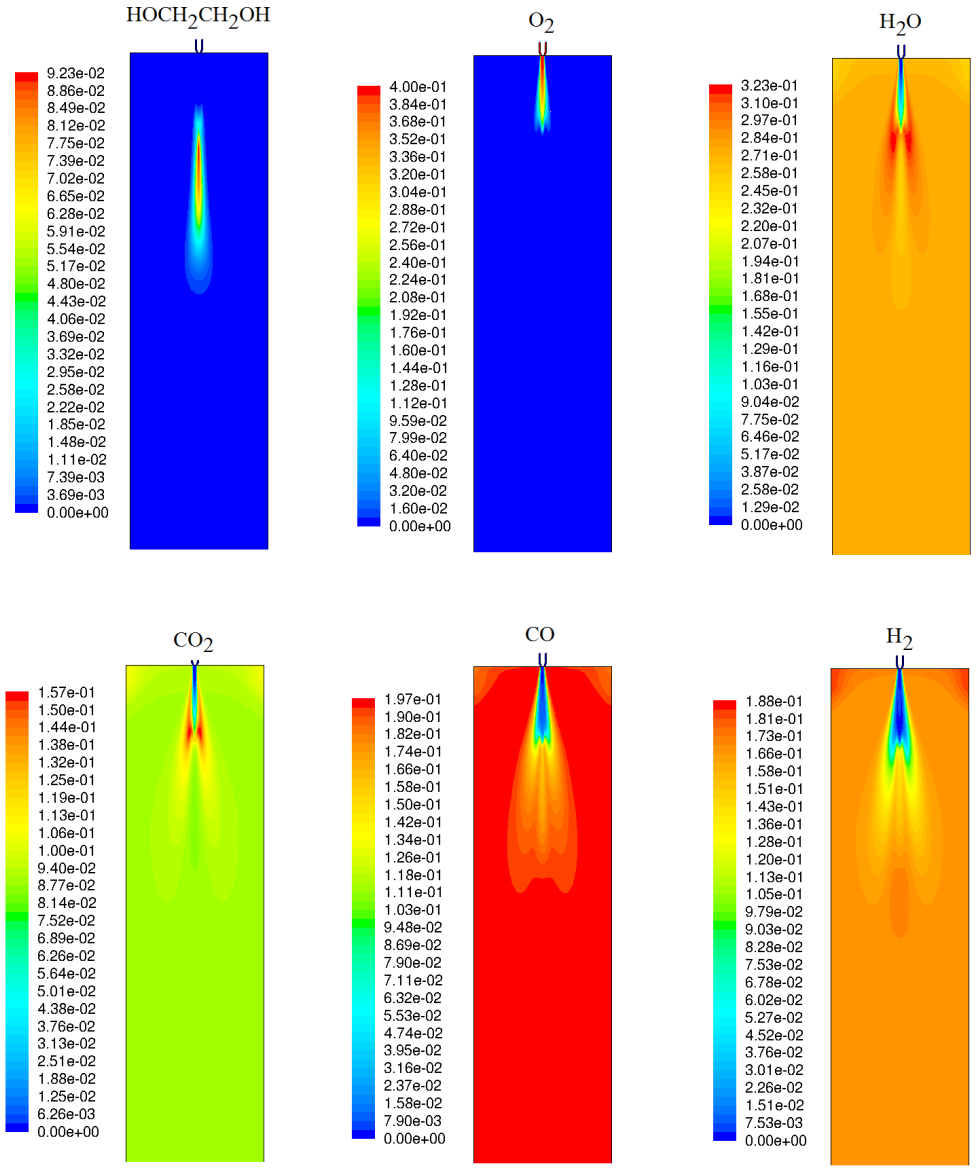

Figure 6.6: Mole fractions of ethylene glycol ($HOCH_2CH_2OH$), O_2, H_2O, CO_2, CO, and H_2 for the top 1 meter of the gasifier

an axial distance of about 155 mm acetaldehyde is formed and the kinetic rate of the ethylene glycol decomposition reaction

$$HOCH_2CH_2OH \rightleftharpoons CH_3CHO + H_2O \tag{6.2}$$

reaches its maximum value at the same distance. This value is one order of magnitude higher than other ethylene glycol decomposition reactions. The contours of mole fractions of acetaldehyde and its radical CH_3CO can be seen in Figure 6.7.

It is observed from Figure 6.6 that the whole amount of oxygen is consumed as it enters the gasifier which is the result of the ethylene glycol intermediate species

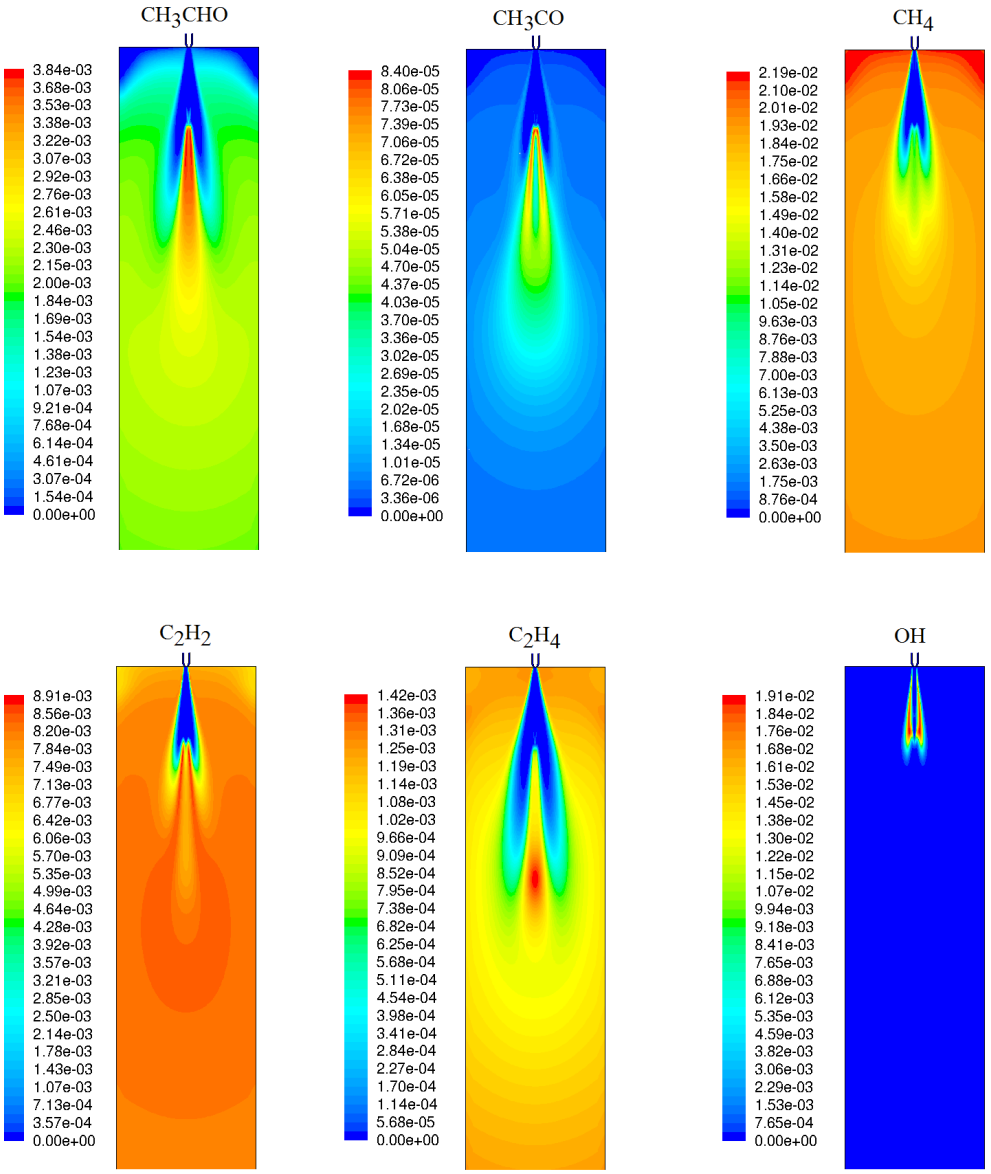

Figure 6.7: Mole fractions of CH_3CHO, CH_3CO, CH_4, C_2H_2, C_2H_4, and OH for the top 1 meter of the gasifier

oxidation as well as the recirculation zone effect already discussed. The products of oxygen reactions with the reactive components CO and H_2 reach high values at the hot regions as can be seen in the contours of mole fractions of CO_2 and H_2O. The recirculation zone causes some gas to be trapped in the top corner of the gasifier which can be seen from for example the H_2 mole fraction contours (Figure 6.6).

The mole fractions of major gasification products at the gasifier exit are listed in Table 6.1, for the gasification case C1. The syngas components CO and H_2 have nearly the same mole fractions, 18.69 mole% and 18.28 mole%, respectively. The listed species account for 99.15 mol% of the product gas. Acetylene (0.7 mol%) and ethylene (0.13 mol%) are two minor species present in the product gas.

Species	CO	H_2	CO_2	H_2O	N_2	CH_4
mol%	18.69	18.28	10.28	25.64	24.08	2.18

Table 6.1: Product gas composition at the gasifier exit for Case C1

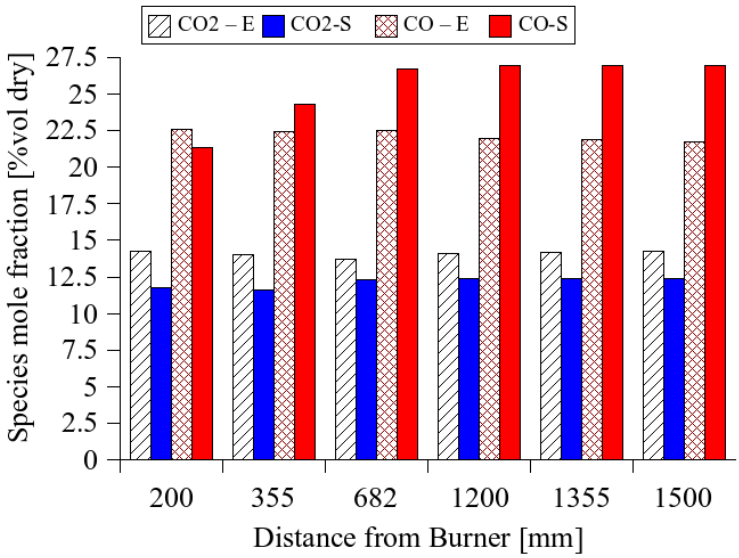

Figure 6.8: Experimental (E) and simulated (S) mole fractions of CO_2 and CO vs. distance from the burner

Figure 6.8 shows the mole fractions of CO_2 and CO in percentage of gas volume for different distances from the burner head. The experimental data were taken from the measurements performed at KIT [104]. The gas samples are extracted from the gasifier through a sampling probe, cooled to 160 °C, filtered, and cooled further via a cooler to condense water vapor. The sample is then analyzed in a gas analyzer [100]. In this way, the CH_4, H_2, CO and CO_2 mole fractions can be measured in dry condition (% vol dry). As can be observed from Figure 6.8, the CO_2 concentration is slightly under-predicted and the CO concentration far from the burner is over-predicted by the model.

The radial profiles of mole fractions of CO_2 and H_2 at an axial distance of x = 200 mm from the burner are depicted together with the experimental values in Figure 6.9. Outside the flame region, the H_2 concentration is higher than the experimental values but the CO_2 concentration shows good agreement with the measurements. In general, the simulation results showed acceptable agreement with the experimental values. A reason for the difference between numerical and experimental values could be the addition of errors due to the differences in the mole fractions when calculating

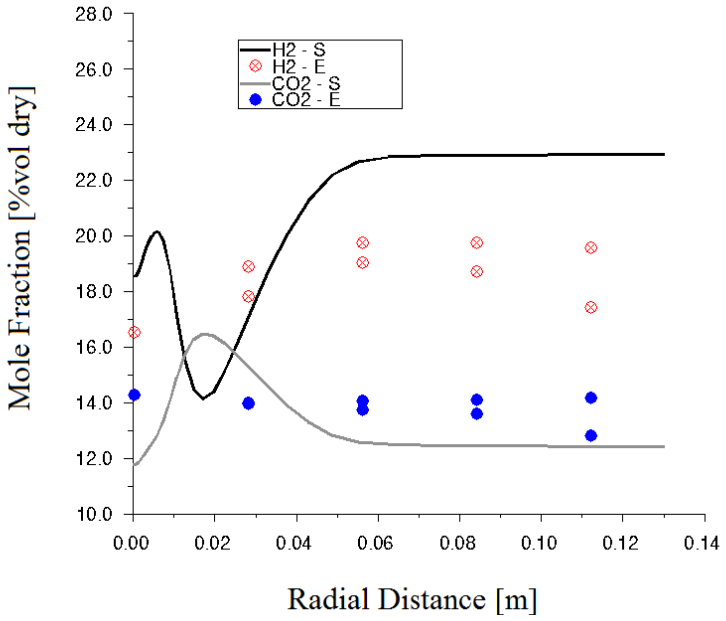

Figure 6.9: Experimental (E) and simulated (S) mole fractions of CO_2 and H_2 vs. radial distance at an axial distance of 200 mm from the burner

them in dry condition. Numerical errors and measurement error tolerances are also another source of discrepancy between the simulation and the experimental results. The error tolerance of the measurements was around ∓ 2.2 % for H_2 and ∓ 1.2 % for H_2O, CO, and CO_2 [101]. Furthermore, the effect of leakage air was neglected in the simulations. Leakage air from the seals of the gasifier flanges [22] has some influence on the temperature field and the gas concentrations due to availability of excess oxygen.

The k-ε turbulence model is known to over-predict the strength of the vortex structure (and consequently the recirculation zone effect) [105]. This causes a reduction of the temperature in the symmetry plane and hence the chemical species concentrations change as well.

To develop the detailed chemical reaction mechanism, some estimates are made [64], which due to the unavailability of enough kinetic data of ethylene glycol oxidation to validate them, are another source of uncertainty of the CFD results.

6.4 Effect of Operating Conditions

In order to study the effect of boundary and operating conditions on the gasification process, a series of simulations were done to perform sensitivity analysis. Four parameters were varied, namely: oxidizer and fuel inlet temperatures, the oxidizer composition which is the enrichment of air with O_2, the air-fuel ratio and the operating pressure of the gasifier. Table 6.2 shows an overview of the different simulation cases taken into account for the parameter studies.

The objective of gasification process is the production of high quality synthesis gas. To check the effectiveness of gasification, a parameter called gasification efficiency is defined as [106]:

$$\eta_{\mathrm{G}} = \frac{\dot{m}_{\mathrm{g}} \mathrm{LHV}_{\mathrm{g}}}{\dot{m}_{\mathrm{f}} \mathrm{LHV}_{\mathrm{f}}} \tag{6.3}$$

where $\dot{m}$ and LHV are the mass flow rate (kg/s) and lower heating value (MJ/kg), respectively. The subscript g stands for the product gas and f for the fuel which in our case is ethylene glycol. The gasification efficiency η_{G} is then the ratio of the heat content of the product gases generated by gasification to the heat content of the fuel when it is totally burnt.

The lower heating value of ethylene glycol is calculated based on its chemical elements and have a value of about 17.94 MJ/kg. For the product gas, the LHV is calculated based on the amount of available burnable chemical species (CO, H_2, CH_4, C_2H_2, and C_2H_4).

6.4.1 Inlet Temperatures

Four cases are considered for studying the changes in inlet temperatures. These cases (case C1-C4) are listed in Table 6.2. In the basic case (C1), both oxidizer and fuel had an inlet temperature of 300 K. The oxidizer temperature was then increased to 330 K (C2) and 350 K (C3) keeping the fuel inlet temperature constant. For the case C4, the fuel and the oxidizer both entered the gasifier at 350 K.

Figure 6.10 shows the gasification efficiency as a function of the inlet oxidizer temperature. With increasing temperature from 300 K to 350 K, the gasification efficiency increased significantly from 68.58 % to 74.48 %. At the same time, the results show that the composition of product gas varied and its LHV increased due to an increase in CO and H_2 mole fractions, as shown in Figure 6.10. The gasification efficiency for the case C4 did not show a significant difference with that of case C3, meaning that preheating the fuel from 300 K to 350 K does not affect the syngas composition

Case	λ [-]	$\dot{m}_f$ [kg/h]	T_f [K]	T_{ox} [K]	x_{O_2} [%]	$T_w[K]$	p [atm]
C1	0.43	9.5	300	300	40	1373	1
C2	0.43	9.5	300	330	40	1373	1
C3	0.43	9.5	300	350	40	1373	1
C4	0.43	9.5	350	350	40	1373	1
C5	0.43	11.9	300	300	50	1373	1
C6	0.43	5.12	300	300	21	1373	1
C7	0.60	9.5	300	300	40	1373	1
C8	0.75	9.5	300	300	40	1373	1
C9	0.30	9.5	300	300	40	1373	1

Table 6.2: Overview of the boundary conditions for the Cases C1 - C9

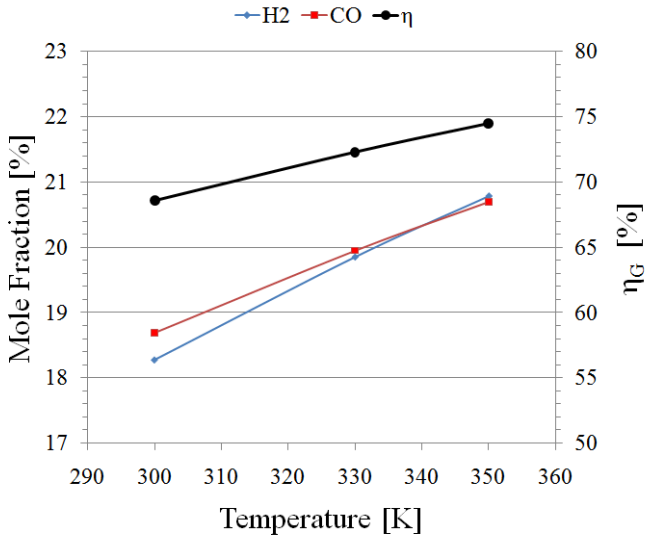

Figure 6.10: Gasification efficiency and mole fractions at the gasifier outlet for different oxidizer inlet temperatures

and hence the gasification efficiency. This is due to the high temperatures inside the gasifier causing the fuel to evaporate very fast as already shown in Figure 6.4.

The highest temperature inside the gasifier has increased from around 2310 K for the case C1 to around 2370 K for the case C3. The position of the highest temperature area moved toward the burner with preheating the oxidizer. This trend is visualized in Figure 6.11. The temperature outside the flame zone did not show significant difference and was about 1375 K for all the cases.

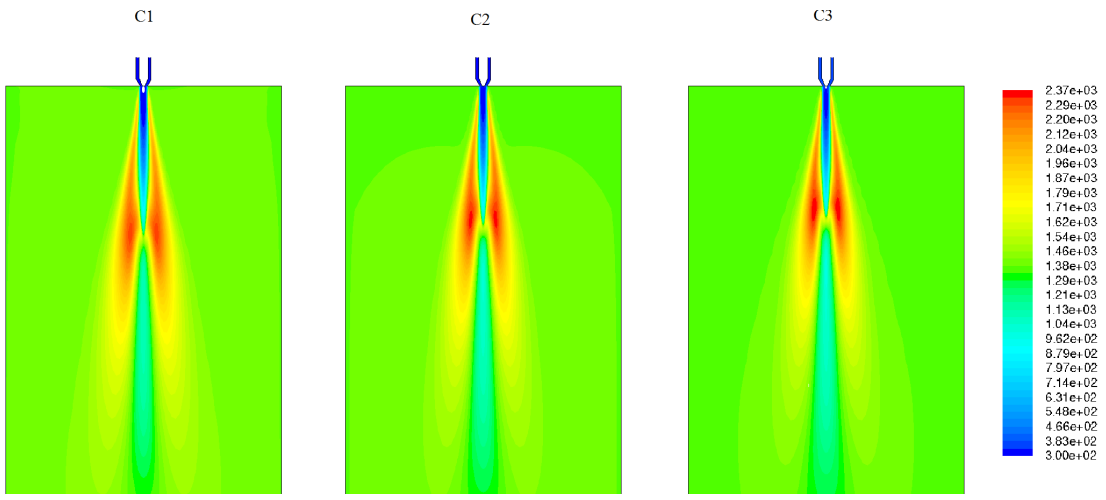

Figure 6.11: Contours of gas temperatures in the flame zone for Cases C1, C2, C3

6.4.2 Oxidizer Composition

To study the effect of the oxygen content of the oxidizer on the gasification efficiency, three cases were considered that are shown in Table 6.2. In the first case (C1) the oxidizer contained 40 % oxygen and the other 60 % of the gas volume is N_2. In the second case (C5), the oxidizer was enriched with even more oxygen to reach $x_{O_2} = 50\%$. These two cases were compared with a case (C6), in which the gasifying agent was air ($x_{O_2} = 21\%$).

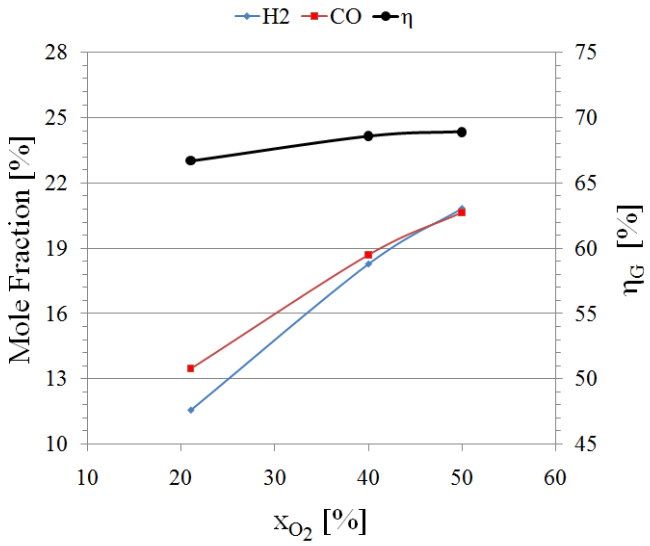

Figure 6.12: Gasification efficiency and mole fractions at the gasifier outlet for different oxidizer compositions

The mole fractions of syngas components (H_2, CO) at the gasifier exit as well as the gasification efficiencies are plotted in Figure 6.12. The plot shows an increase in the gasification efficiency as the oxygen mole fraction increases, although the increase

is not considerable between the cases with $x_{O_2} = 40\%$ and $x_{O_2} = 50\%$. As x_{O_2} was increased, the mole fraction of H_2 increased faster than that of CO.

The maximum temperature inside the gasifier increased from about 1820 K for gasification with air to about 2490 K when the gasifying agent contained 50 % oxygen. This was mainly due to the decrease in the thermal ballast N_2.

6.4.3 Air-Fuel Ratio

In order to study the effect of the air-fuel ratio (λ) on the gasification efficiency and the composition of the product gas, the basic case C1 (λ=0.43) was considered with three other cases C7, C8, and C9 with λ=0.60, λ=0.75, and λ=0.30, respectively. The results of the comparison are shown in Figure 6.13.

With increasing λ, one moves from gasification to combustion. This implies that the gasification efficiency should decrease and less syngas should be produced (solid lines in Figure 6.13). On the other hand, the combustion products CO_2 and H_2O increase. Furthermore, the heat release from the process increases and large amount of heat transfered from the walls of the gasifier causing the process not to be adiabatic anymore. An adiabatic boundary condition for the gasifier wall was selected to study its effect on the gasification. The dashed lines in Figure 6.13 indicate the results of the simulations of the three cases C1,C7 and C8 with adiabatic boundary conditions.

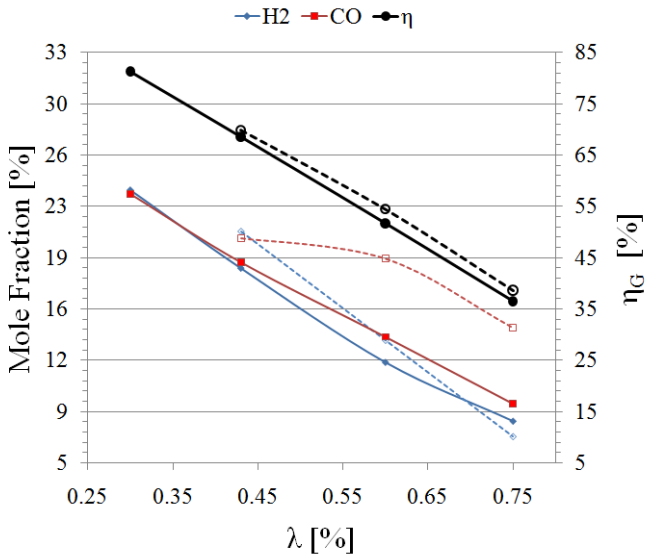

Figure 6.13: Gasification efficiency and mole fractions at the gasifier outlet for different air-fuel ratios for constant wall temperature (solid lines) and adiabatic walls (dashed lines)

A slight increase of the gasification efficiency was observed for the adiabatic cases in comparison with the non adiabatic cases. This was due to the increase in the mole fractions of H_2 and CO and hence the LHV of the product gas. However, the simulations indicated that the mole fractions of CH_4, C_2H_2 and C_2H_4 were around zero for the adiabatic cases. This was due to the increase in the reactor temperature. The reactor temperature increased from around 1373 K for the non adiabatic cases to 1485 K, 1954 K and 2300 K for the adiabatic cases with $\lambda = 0.43$, $\lambda = 0.60$ and $\lambda = 0.75$, respectively. At higher reactor temperatures, the reactions proceeded faster, resulting in the faster decomposition of CH_4, C_2H_2 and C_2H_4 to the end product species CO, CO_2, H_2 and H_2O. For the non adiabatic cases, the mole fractions of the minor species decreased with increasing the air-fuel ratio. For example, the methane mole fraction decreased from 3.47 % for $\lambda = 0.30$ to 0.73 % for $\lambda = 0.75$.

The maximum flame temperature has increased from around 2310 K for $\lambda = 0.43$ to around 2480 K for $\lambda = 0.75$. The increase in the heat release with increasing air-fuel ratio caused the hot zone to be bigger.

6.4.4 Pressure

Operating a gasifier under high pressures leads to a reduction of the specific volume of the gases, which in return decreases the dimensions of the equipment [107]. On the other hand, increasing the operating pressure causes an increase in manufacturing costs. In case of the bioliq® process, the high pressure operation is desirable as it obviates intermediate syngas compression prior to the fuel synthesis step [3].

The case C6 (see Table 6.2) was considered as the basis case for studying the effect of the reactor operating pressure on the gasification efficiency. Two more cases were considered in which the operating pressure was increased to 2 and 5 bars, respectively. All the other boundary conditions were kept constant as those of C6.

The gasification efficiency increased from η_G=66.72 % for atmospheric gasification to 71.55 % when the operating pressure was 5 bars. This was due to the increasing of the LHV of the product gas due to higher fractions of CO and H_2 as can be seen in Figure 6.14. A gradual increase in the ratio of hydrogen to carbon monoxide, from about 0.83 at atmospheric pressure to over 1.11 at 5 bars was observed which shows the capability of adjusting the ratio of syngas constituents by changing the operating pressure. However, this may be of limited value since the operating pressure is usually determined by other process based considerations.

The REGA is designed for the operation under atmospheric pressures. Due to this fact, high pressure gasification simulations were not performed based on the

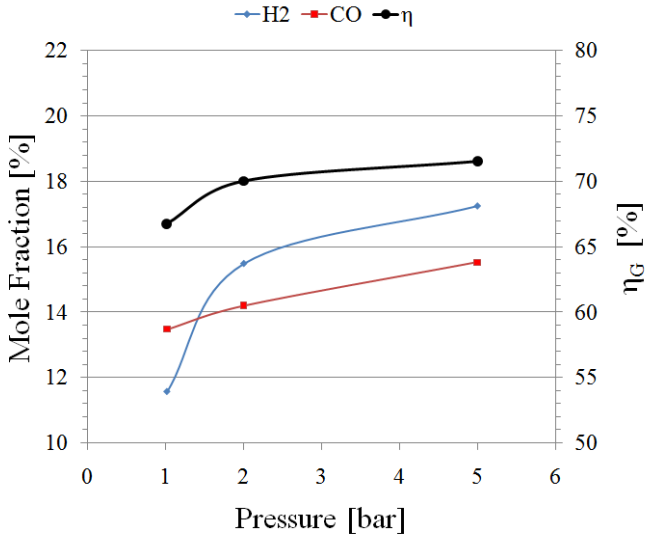

Figure 6.14: Gasification efficiency and mole fractions at the gasifier outlet for different pressures

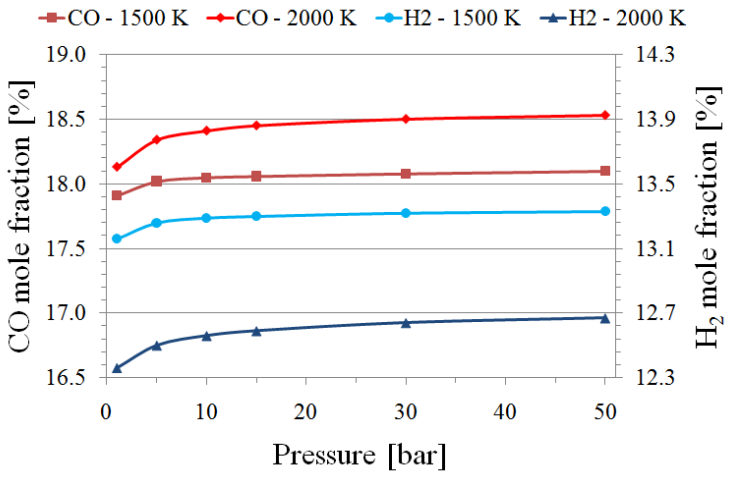

Figure 6.15: Mole fractions of CO and H_2 for different temperatures and pressures

geometry of the gasifier and the burner. To check the effect of high pressures on the composition of the product gas, a series of simulations using the HOMREA software were carried out. The initial reaction pressure was varied from 1 bar up to 50 bars and the initial temperature was varied between 900 K and 2100 K. The results of two cases with initial temperatures of 1500 K and 2000 K are depicted in Figure 6.15. At initial reaction temperature of 2000 K, an increase in the mole fractions of H_2 and CO was seen up to reaction pressure of 15 bar. In the case of higher pressures, the gas composition remained almost constant. The same trend can be observed in the lower reaction temperature.

It should be noted that the ethylene glycol reaction mechanism is validated for pressures up to about 40 bars [64]. For simulations with higher pressures, care should be taken about the usage of the reaction mechanism.

When comparing Figures 6.14 and 6.15, the predicted gas compositions show significant differences which is due to the differences in the model assumptions used in the simulation softwares. In HOMREA, an ideal jet stirred reactor is considered and the effect of thermal radiation is neglected. Whereas in ANSYS FLUENT, effects of turbulence and thermal radiation are taken into account.

6.5 Effect of Chemistry

In this section, the effect of chemistry on the simulation results of the gasification process is studied. In the first part, three versions of the chemical reaction mechanism, developed for ethylene glycol oxidation, are used for CFD simulations and the results are compared. In the second part of this section, the three chemistry models already discussed in chapter 4 (equilibrium chemistry model, flamelet model and eddy dissipation concept) will be compared together. These models are developed based on different underlying assumptions which offer certain advantages and disadvantages for the simulation of a selected reactive flow problem.

6.5.1 Reaction Mechanism

Due to the lack of experimental kinetic rate data for high temperature ethylene glycol oxidation, some of the rate constants had to be estimated using statistical correlations and analogies to other reactions [64]. For the estimation of the activation energies from analog reactions, the Bell-Evans-Polanyi equation [108, 109] was used

$$E_{\mathrm{a},1} = E_{\mathrm{a},0} + \alpha \Delta H^0_{\mathrm{R}} \tag{6.4}$$

where $E_{\mathrm{a},0}$ is the activation energy of the analog reaction, α is a factor between 0 and 1 and ΔH^0_{R} is the difference between the standard reaction enthalpies of the reactions.

The reaction mechanism used in this thesis was developed based on $\alpha = 0.5$ [64]. To study the effect of the changes in the reaction scheme on the gasification, two versions of the reaction mechanism, created with $\alpha = 0.0$ and $\alpha = 1.0$, were considered together with the original mechanism.

The calculations based on the package HOMREA did not show significant differences in the mole fractions of the major gasification product species CO, CO_2, H_2 and H_2O.

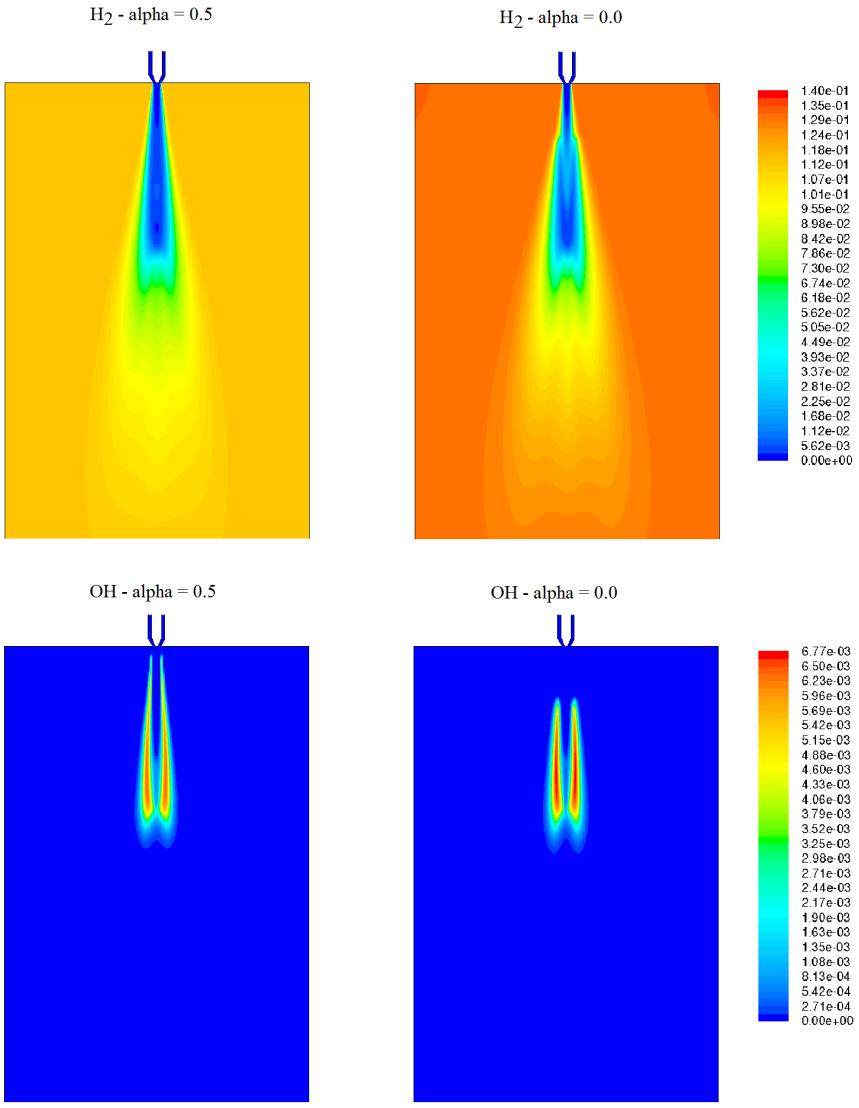

Figure 6.16: Contours of mole fractions of H_2 (top) and OH (bottom) at the top part of the gasifier for simulations using different versions of the reaction mechanism with $\alpha = 0.0$ (right) and $\alpha = 0.5$ (left)

For the CFD simulations in ANSYS FLUENT, the gasification case C6 was studied using the three chemical reaction mechanisms. No significant difference has been observed in the mole fractions of major species (< 0.5 %) for the cases with $\alpha = 0.5$ and $\alpha = 1.0$. However, in the simulation using the mechanism with $\alpha = 0.0$, the mole fraction of H_2 was increased about 2 % at the gasifier outlet. This increase caused a decrease of about 1 % in the mole fraction of H_2O, as expected. The changes in the mole fractions of other species were not significant (< 0.3 % for CO and CO_2). The contours of the mole fractions of H_2 and OH on the top part of the gasifier is shown in Figure 6.16. The shape of the flame based on the OH concentration can be seen in this figure as well. No OH production was observed in the very vicinity of the burner when $\alpha = 0.0$ was used.

The results of the simulations emphasize that the choice of reaction kinetics plays a role if one is interested in the flame shape and properties, however, the product gas composition at the gasifier outlet did not show great sensitivity to the choice of reaction kinetics (α values) for the studied chemical reaction mechanism. For the effects of the factor α on the ignition delay times and flame velocities, the reader is referred to [64].

6.5.2 Chemistry Model

Within the framework of this thesis, a comparison of the chemistry models available in the CFD code ANSYS FLUENT has been done. These models have been discussed in chapter 4 in detail. The boundary conditions used, were based on the gasification case C1 (see Table 6.2). The simulations were performed using non-premixed combustion with equilibrium chemistry (EQ), the steady laminar flamelet model (SLF) and the eddy dissipation concept (EDC).

The computational costs of the EQ and the SLF models are much lower than that of the EDC model. This is due to the fact that the preprocessing of chemistry in look-up tables is possible for the EQ and SLF models. Therefore, only two and three transport equations for the EQ and SLF models, respectively, are required to be solved. The EDC model, on the other hand, solves one transport equation for each chemical species. The model utilizes the ISAT procedure to decrease the computational time for chemistry calculations, but is still a very time consuming model when detailed reaction mechanisms are used.

The resulting mole fractions of major product species at the gasifier outlet are shown in Figure 6.17. As seen in this figure, the mole fractions of the species for simulations with the flamelet model (SLF) and the equilibrium chemistry model (EQ) have almost the same values at the outlet. As the stoichiometric scalar dissipation (χ_{st} in equation 4.23) tends to zero in the SLF, the chemistry tends to equilibrium. This happens outside of the flame zone and is the reason for the equality of the species mole fractions at the gasifier outlet. The mole fractions of methane, acetylene and ethylene are predicted by both EQ and SLF models to be zero at the gasifier outlet, whereas the EDC model predicted methane to be 2.18 % and acetylene and ethylene together around 0.83 % of the product gas at the outlet.

In the flame zone, the temperatures are predicted higher by the EQ model than by the SLF model, which is due to the equilibrium calculations [110]. However, the temperatures predicted by both models are qualitatively similar, as can be seen in Figure 6.18. Furthermore, the SLF model underpredicts the temperature in com-

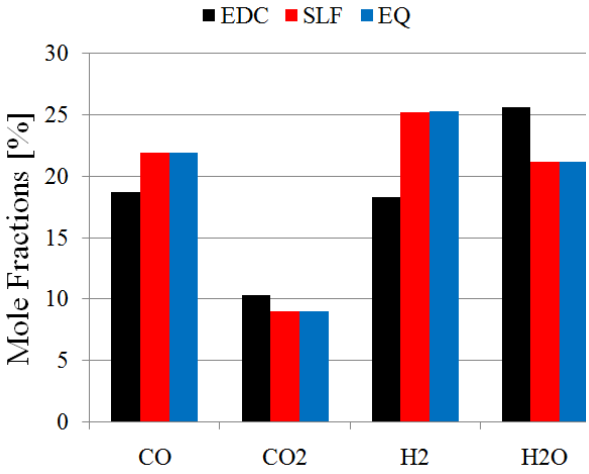

Figure 6.17: Mole fractions of CO, CO_2, H_2 and H_2O at the gasifier outlet Resulting from simulations with Eddy Dissipation Concept (EDC), Steady Laminar Flamelet Model (SLF) and Equilibrium Non-premixed Chemistry Model (EQ)

parison with the EDC model. This trend in temperature prediction of both models is mentioned in the literature as well [27, 111].

An overprediction of H_2 is observed by the EQ model in comparison with the SLF model which is due to the assumption of fast chemistry in EQ model [112]. On the symmetry axis of the gasifier, CO and H_2 mole fractions peak nearer to burner in SLF (and EQ) model comparing with EDC as seen in Figure 6.18.

The mass fractions of H_2O, CO_2 and OH for the SLF and EDC models are depicted in Figure 6.19. It is evident that the SLF model predicts higher H_2O mass fractions and significantly lower CO_2 mass fractions than the EDC model. Liu et al. [113] reported the same trend when comparing the SLF model with direct numerical solutions. The maximum OH mass fraction predicted by both models did not differ significantly. The OH mass fraction in the SLF model, however, spreads much further downstream than that of the EDC model as observed in Figure 6.19. Generally, the SLF model predicts a faster conversion of the fuel species into products. This is in accordance with the results of other studies [114].

One should note the importance of the turbulence model on the predictions of temperature and chemical species by chemistry models. The predicted profiles of the mixture fraction, its variance and the scalar dissipation rate in the SLF model are sensitive to the turbulence model [115]. Inaccurate description of mixing causes discrepancies between predictions and measurements. The quality of the EDC model predictions depends also on the performance of the turbulence model. In this case,

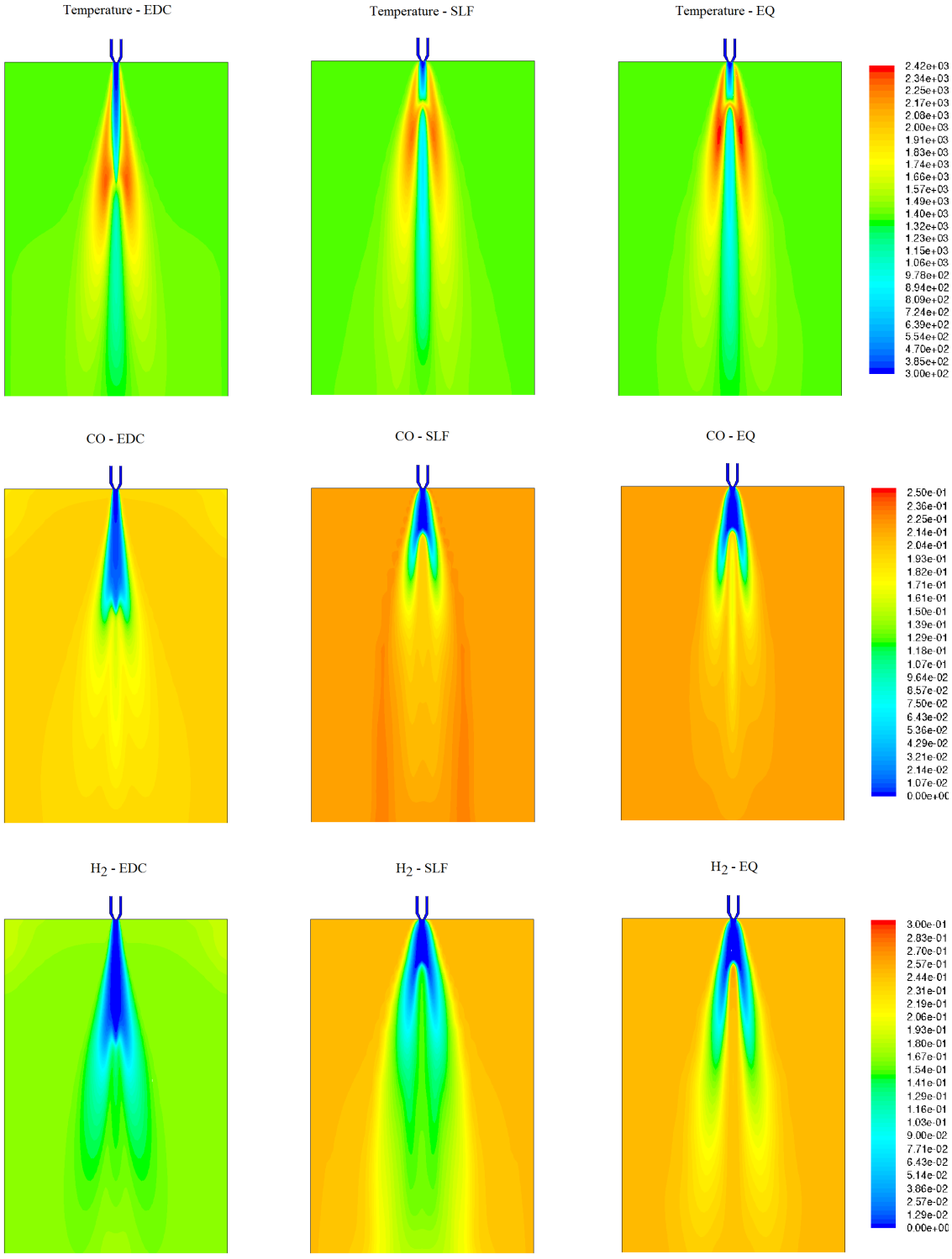

Figure 6.18: Contours of temperature, CO, and H_2 mole fractions resulting from simulations with Eddy Dissipation Concept (EDC), Steady Laminar Flamelet Model (SLF), and Equilibrium Nonpremixed Chemistry Model (EQ) at the top part of the gasifier

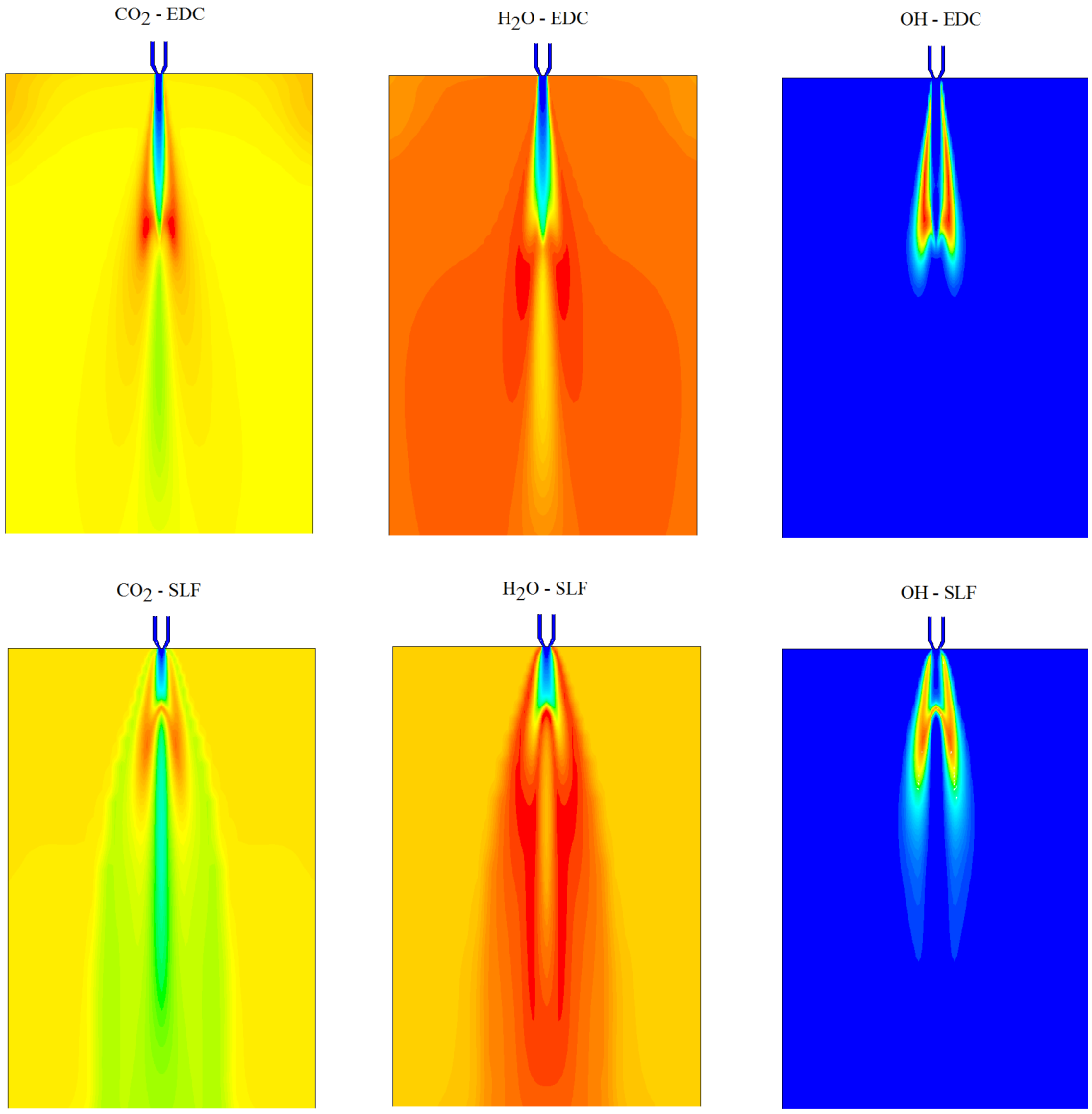

Figure 6.19: Contours of mass fractions of CO_2, H_2O, and OH, resulting from simulations with Eddy Dissipation Concept (EDC), and Steady Laminar Flamelet Model (SLF) at Top Part of the Gasifier

the length fraction and time scale of the fine structures (equations 4.32 and 4.33, respectively) directly depend on the turbulence properties (k and ε). An inaccurate prediction of these two quantities leads to erroneous calculation of ξ^* and τ^* and hence the thermochemical field.

The scalar dissipation rate (used in the SLF model) is insufficient to quantify the non-equilibrium structure of a diffusion flame in an axisymmetric coflow configuration [113]. In addition, the studied gasifier (REGA) with recirculation zones is problematic for flamelet models. For these reactors, partially reacted fluid is recirculated to mix with the feed streams so that the simple non-premixed flow model

		Slurry		Oxidizer
Case	λ [-]	w_{eg} [%]	w_{char} [%]	x_{O_2} [%]
C1	0.43	100	0	40
C10	0.43	90	10	40
C11	0.43	80	20	40

Table 6.3: Slurry gasification cases

no longer applies [72]. The EDC model proves to be a better choice when modeling gasification in entrained flow gasifiers with recirculation zones.

However, care should be taken not to make a definite statement about one model's superiority over another, as the model predictions depend strongly on the process and boundary conditions for the problem in question.

6.6 Slurry Gasification Simulation

As discussed in section 1.2, a mixture of pyrolysis oil and char was used as the feed for the gasification in the bioliq® process. Ethylene glycol was used as a model fuel for pyrolysis oil. In order to simulate the gasification process using slurry, a submodel, developed by Hafner [64], was utilized in ANSYS FLUENT, which modeled the char particle gasification and combustion. For the detailed description of the model, the reader is referred to [64].

The model is based on the heterogeneous reactions of carbon with gasifying agents CO_2, H_2O, and O_2 which takes into account the inhibition effect of CO and H_2. Each char particle is composed of a porous carbon sphere. The slurry is then a mixture of char particles and ethylene glycol droplets. It is assumed that at the beginning, the porous part of a char particle is filled with ethylene glycol.

After the slurry enters the gasifier, the particles are heated and the ethylene glycol vaporizes and enters the gas phase. At the same time, the char particles are heated and react with the gasifying agents. The char gasification product is composed of CO, CO_2, and H_2.

In order to simulate the slurry gasification and to study the effect of char particles on the product gas and the gasification efficiency, two cases were considered together with the case C1. The considered cases are summarized in Table 6.3.

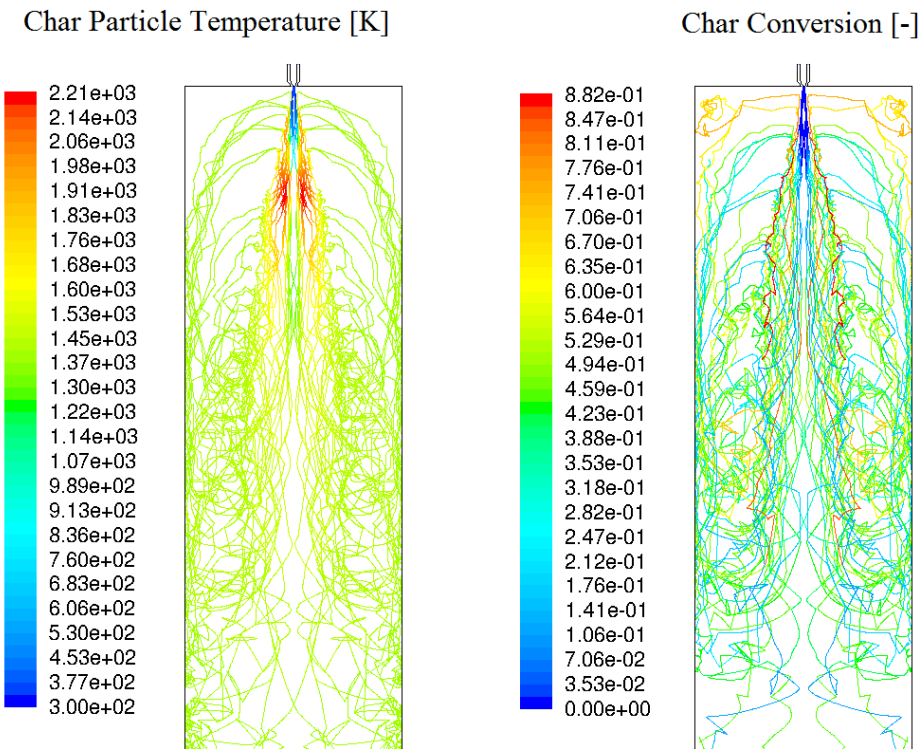

Figure 6.20: Contours of char particles temperature and char conversion for Case C10 at the top 1 meter of the gasifier

The case C1 has already been discussed in section 6.1. For the cases C10 and C11, the mass fraction of char particles in the slurry (w_{char}) was chosen to be 10 % and 20 %, respectively. All other boundary conditions were kept constant as those of the case C1 in Table 6.2.

Figure 6.20 shows the char particle temperatures and the char conversion for the case C10. For clarity reasons only 20 % of the simulated particles are shown in this figure. The highest particle temperature occured in the flame zone and was more than 2200 K. This caused the particles to react very fast with the available oxygen. The recirculation zone played an important role in the char conversion by increasing the residence time of the particles inside the gasifier. Those particles that were not trapped in this zone have not been completely converted and exited the gasifier, which in turn results in more effort in the gas cleaning steps.

Figure 6.21 shows the contours of the chemical species CO and H_2 produced through char particle reactions for both considered cases C10 and C11. Hydrogen was produced by the reaction of char particles (C_f) with H_2O as

$$C_f + H_2O \rightleftharpoons C(O) + H_2. \tag{6.5}$$

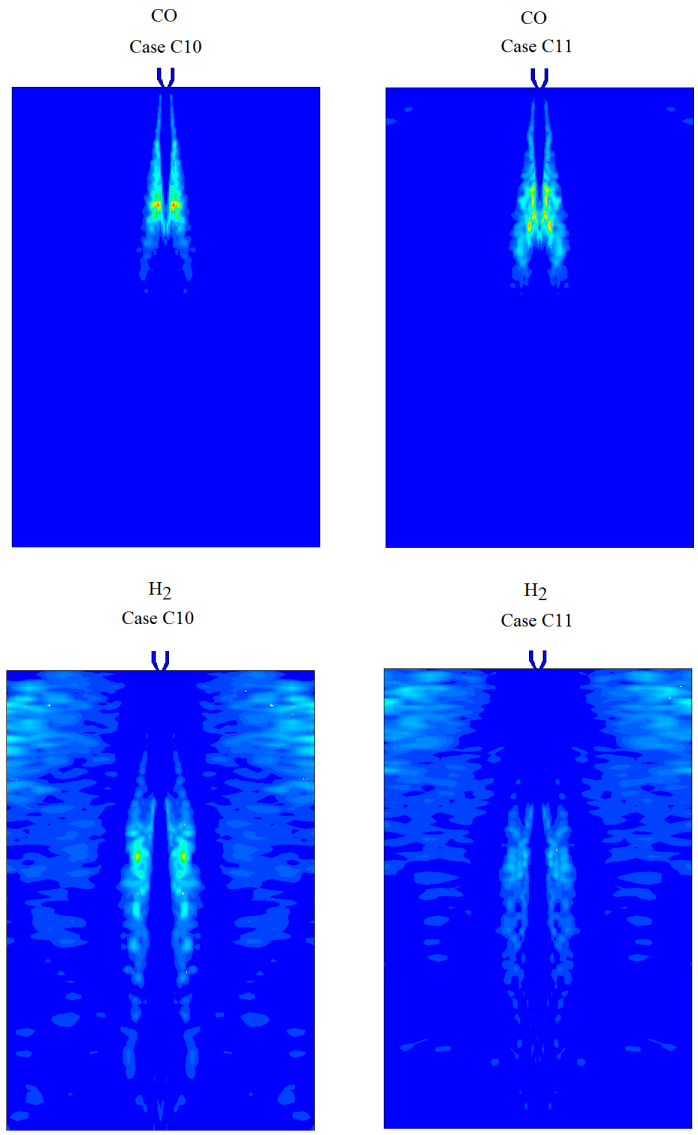

Figure 6.21: Contours of produced CO and H_2 from char particles for Cases C10 and C11 at the top part of the gasifier

By comparing Figures 6.7 and 6.21, it can be observed that the H_2 production was high in the areas where H_2O had a high concentration. At the top corner of the gasifier, where some water vapor was trapped, the hydrogen production was also of importance. At the second half of the gasifier (not shown in Figure 6.21), the char particles not trapped in the recirculation zone reacted with H_2O molecules and produced more hydrogen.

CO was produced near the burner outlet due to the availability of oxygen according to the following chemical reaction:

$$C_f + O_2 \longrightarrow CO + CO_2 \tag{6.6}$$

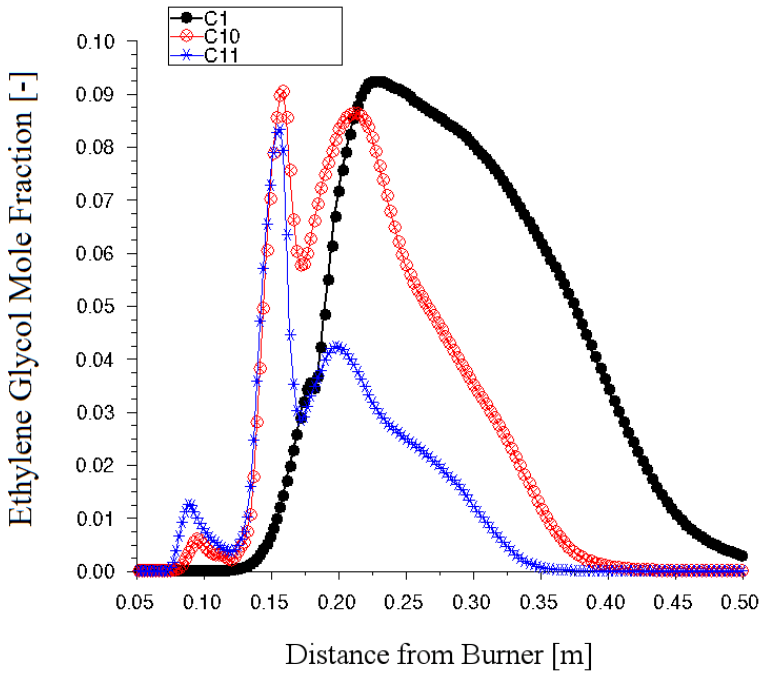

Figure 6.22: Mole fraction of ethylene glycol in the gas phase along the symmetry axis of the gasifier for different char contents

The kinetics of the above reaction indicates that more CO is produced at high temperatures (above 1000 K). At low temperature regions, on the other hand, more CO_2 is produced. This can be seen as well in Figure 6.21.

As in the case of H_2, at the second half of the gasifier some char particles, not trapped in the recirculation zone, reacted with the available CO_2 molecules and produced CO according to the reaction

$$C_f + CO_2 \rightleftharpoons CO + C(O). \tag{6.7}$$

The rate of CO production in this zone was not very high in comparison to that of the area near the burner.

The evaporation of ethylene glycol drops trapped in the pores of char particles caused a change in the distribution of ethylene glycol in the gas phase as can be observed from Figure 6.22. For the case C1, where no char particles were present, the ethylene glycol droplets started to evaporate at an axial distance of about x = 120 mm from the burner and reached their maximum at about x = 220 mm across the symmetry axis. In the cases C10 and C11 some ethylene glycol entered the gas phase at a distance of about x = 60 mm from the burner which was due to some evaporation from the pores of the char particles. The maximum values of ethylene glycol con-

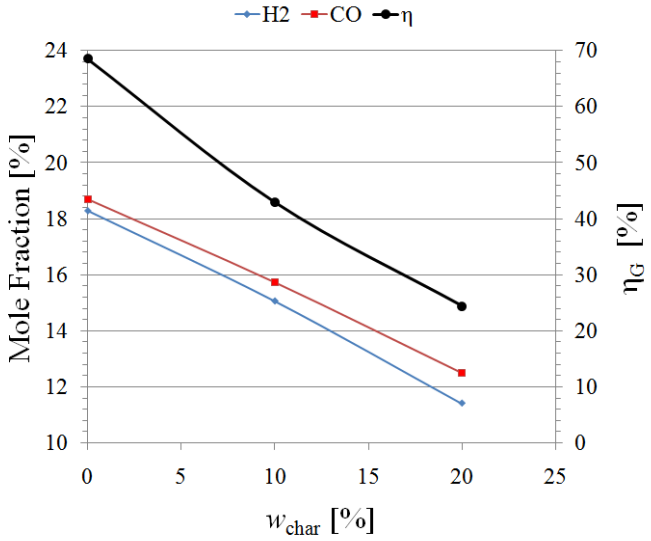

Figure 6.23: Gasification efficiency and mole fractions at the gasifier outlet for different char contents

centration in gas phase decreased for cases C1, C10 and C11 due to the decrease in the initial mass fraction and the distribution of droplets in the fuel.

The mole fractions of CO and H_2 showed a decrease with increasing the mass fraction of char as shown in Figure 6.23. An explanation for the decrease in CO and H_2 is that the char particles enter the gasifier at the burner position and enter the flame zone where very reactive chemical radicals such as OH and O are present. The produced species CO and H_2, resulting from the reaction of carbon particles with oxygen and water vapor (reactions 6.5 and 6.6), react with the radicals, for example OH, through the following reactions

$$H_2 + OH \rightleftharpoons H_2O + H \tag{6.8}$$

$$CO + OH \rightleftharpoons CO_2 + H \tag{6.9}$$

This causes the production of CO_2 and H_2O, which in turn do not react back to CO and H_2 very easily. One way to deal with this problem is a later injection of char particles so that they do not come into contact with reactive chemical radicals. The new injection should again create a recirculation zone so that the char particles are present in the gasifier long enough for the char gasification reactions to take place.

Figure 6.23 further shows a decrease in the gasification efficiency when using char particles in the fuel. One reason is the mentioned decrease in CO and H_2 and the

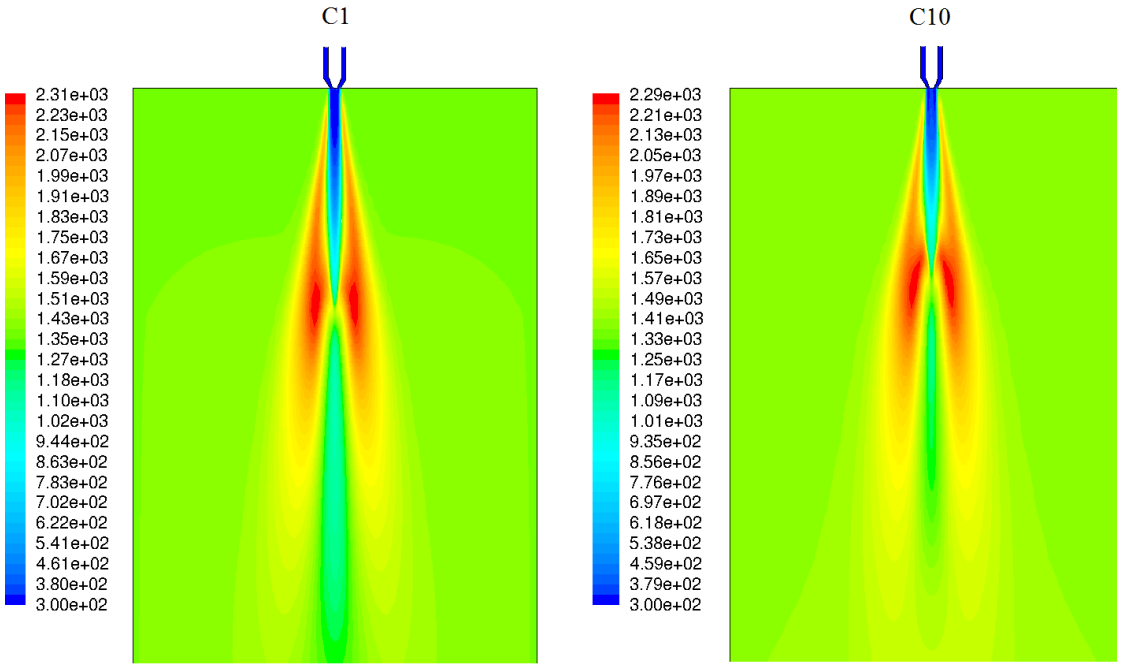

Figure 6.24: Contours of temperature for Cases C1 and C10 at the top part of the gasifier

other reason is the increase in the lower heating value (LHV) of the fuel due to the presence of char. This means an increase in the heat content of the fuel (the denominator of the right hand side of equation 6.3) of about 10 % and 20 % for the cases C10 and C11, respectively.

Figure 6.24 shows the contours of temperature for cases C1 and C10 at the top of the gasifier. The maximum temperature in the flame zone inside the gasifier decreased from around 2310 K in the case C1 to around 2285 K for the case C10. This decrease was due to the gasification of char particles. The reactions of char particles with H_2O and CO_2 are endothermic reactions which occured in the hot part of the flame and caused the temperature to drop. Furthermore, the exothermic reaction of char particles with oxygen caused the location of the maximum temperature to move further upstream toward the burner as can be observed in Figure 6.24.

7. Conclusions and Perspective

The prime goal of this work was the modeling and simulation of the gasification of biomass-based pyrolysis oil-char slurry in an entrained flow gasifier as a part of the bioliq® process. In this two-stage process, straw or other abundant lignocellulosic agricultural by-products are converted to syngas through fast pyrolysis and subsequent entrained flow gasification.

The entrained flow gasification belongs to the class of reactive turbulent flow problems which, due to the complex interactions between chemistry and turbulence, needs special attention. The choice of the chemistry-turbulence interaction model as well as other related physical and numerical submodels play an important role in the CFD simulation results.

The models discussed in chapters 2 to 5 as part of the CFD software package ANSYS FLUENT were used to perform the simulations. Ethylene glycol served as a non-toxic model substance for the biomass-based pyrolysis oil in the experiments at KIT. It has also been used in this work as the model substance in order to allow a comparison between simulation results and the experimental results.

A 2-D axisymmetric geometrical model of the pilot scale entrained flow gasifier REGA was used for the mesh generation. The simulation results are presented and discussed in chapter 6.

The cold flow simulation results showed acceptable agreement with the experimental measurements. However, more experimental values would help to optimize the model constants of the k-ε turbulence model shown in Table 3.1. In this work, the values suggested by [26] and [32] have been used.

The reactive flow simulations were also compared with experimental measurements wherever possible. These comparisons again showed acceptable agreement. The simulations depicted the importance of the recirculation zone in entrained flow gasification. It brings the hot reactive gas into contact with the injected oxidizer, helping the flame to hold its high temperature. The recirculation zone plays another important role in the entrained flow gasification of slurry. Due to the recirculation, the char particles have longer residence time in the gasifier to react with the gas phase. The choice of the turbulence model is of essential importance for the modeling of the recirculation zone. More work is required to study the effect of other turbulence models on the prediction of flow patterns inside an entrained flow gasifier.

The use of eddy dissipation concept (EDC) enabled us to employ detailed chemical reaction schemes in the turbulent flow. The reaction mechanism utilized in this work is based on the simplification of the mechanism developed by Hafner [64]. The simplification was performed using sensitivity and reaction flow analysis. With detailed chemistry the reaction path of the oxidation of ethylene glycol could be observed in the simulations. The detailed chemistry enables one to study the chemical processes and composition of the chemical intermediates which is not possible when using global reactions. With regard to calculation time, the EDC is a very expensive model and should thus be used where the fast chemistry assumption can not be assumed.

In order to study the effect of boundary conditions on the gasification process, a series of simulations were done to perform sensitivity analysis. Four parameters were varied, namely: oxidizer and fuel inlet temperatures, the oxidizer composition, the air-fuel ratio and the operating pressure of the gasifier.

An increase in the oxidizer inlet temperature caused an increase in the gasification efficiency as well as an increase in the mole fractions of H_2 and CO. The increase in the inlet temperature of the fuel did not show a significant effect on gasification efficiency nor on the product gas composition. Here, the heat in the product gas can be used to preheat the oxidizer to achieve a more efficient gasification.

Enrichment of the air with oxygen has a positive effect on the gasification process. As the air is enriched, the amount of N_2 decreases which in return causes higher temperatures in the flame and a higher amount of syngas. In this way the gasification temperature can be regulated as desired. Decrease in the oxidizer N_2 is also in favor of decreasing the pollutant production (NOx, NH_3, etc.). The NOx formation chemistry, which is of interest when using air as the oxidizer, has not been considered in this thesis.

With increasing air-fuel ratio, conditions shift from gasification to combustion. This implies that the gasification efficiency should decrease and less syngas (CO and H_2) and more CO_2 and H_2O should be produced. Larger values of the air-fuel ratio cause higher heat release rates. Operating the gasifier under adiabatic boundary condition increases the reactor temperature and promotes syngas production. Other burnable gases such as CH_4 and C_2H_2 were not present in the product gas, which would facilitate the gas cleaning and conditioning steps.

Operating the gasifiers under high pressures is desirable as it decreases the size of the gasifier and in the case of the bioliq® process, obviates intermediate syngas compression prior to the fuel synthesis. An increase in the gasification pressure showed an increase in the efficiency of the process. Furthermore, the ratio of hydrogen to carbon monoxide changed by changing the pressure, which can be of interest for different downstream syngas utilizations.

Variations in other operating and boundary conditions are not considered in this thesis. More simulations for the varied parameters to cover a broader range may help to better understand the effect of these parameters on the process.

Three different chemistry models were studied in this thesis. Their relative advantages and disadvantages were examined. The EDC model proved to be the better choice when modeling gasification in entrained flow gasifiers with recirculation zones. However, care should be taken not to make a definite statement about one model's superiority over another, as the model predictions depend strongly on the process and boundary conditions for the problem in question.

The gasification of slurry was simulated using char particles suspended in ethylene glycol. The char reaction model was developed by Hafner [64]. The simulations showed a decrease in the flame temperature with increasing the mass fraction of char particles in the slurry. This is due to the endothermic reactions of particles with water vapor and CO_2. The mole fractions of CO and H_2 decreased too, which caused a decrease in the gasification efficiency. This is because the CO and H_2 produced by the reactions of char particles with oxygen and water vapor react with chemically reactive radicals in the flame region to CO_2 and H_2O. One way to deal with this problem is a later injection of the char particles so that they do not come into contact with these radicals. The new injection should again create a recirculation zone so that the char particles are present long enough for the char gasification reactions to take place.

The simulations performed in this work help to better understand the gasification process inside entrained flow gasifiers and considerably reduce the number of ex-

periments needed to characterize the system. The simulations produced spatial and temporal profiles of different system variables that are hard or sometimes even impossible to measure or would require expensive experiments. However, more experimental measurements would help to validate and optimize the CFD model. The sensitivity analyses performed in this study are considered as a basis to find optimized operating conditions and assist in the successful scale-up of the entrained flow gasifiers.

Bibliography

[1] European Commission. Renewable Energy Road Map, renewable energies in the 21st century: building a more sustainable future. Technical report, COM(2006)848, 2007.

[2] European Commission. On sustainability requirements for the use of solid and gaseous biomass sources in electricity, heating and cooling. Technical report, COM(2010)11, 2010.

[3] E. Henrich and F. Weirich. Pressurized entrained flow gasifiers for biomass. *Environmental Engineering Science*, 21:53–64, 2004.

[4] T. Bridgwater. Biomass for energy. *Journal of the Science of Food and Agriculture*, 86:1755–1768, 2006.

[5] UNFCCC. Clarifications on definition of biomass and consideration of changes in carbon pools due to a CDM project activity. Technical report, EB-20, Annex 8, 2005.

[6] P. Basu. *Biomass gasification and pyrolysis - practical design and theory.* Academic Press, 2010.

[7] P. Kumar, D. M. Barrett, M. J. Delwiche, and P. Stroeve. Methods for pretreatment of lignocellulosic biomass for efficient hydrolysis and biofuel production. *Ind. Eng. Chem. Res.*, 48 (8):3713–3729, 2009.

[8] Y. Shinya and M. Yukihiko, editors. *The Asian Biomass Handbook.* The Japan Institute of Energy, 2008.

[9] I. Olofsson, A. Nordin, and U. Soderlind. Initial review and evaluation of process technologies and systems suitable for cost-efficient medium-scale gasification for biomass to liquid fuels. Technical report, ETPC Report 05-02, 2005.

[10] A. van der Drift, H. Boerrigter, B. Coda, M. K. Cieplik, and K. Hemmes. Entrained flow gasification of biomass: Ash behaviour, feeding issues, and system analyses. Technical report, ECN and Shell Global Solutions, ECN-C-04-039, 2004.

[11] R. L. Bain. Biomass gasification overview. Technical report, National Renewable Energy Laboratory (NREL), US Department of Energy (DoE), 2004.

[12] L. Leible, S. Kaelber, G. Kappler, S. Lange, E. Nieke, P. Proplesch, D. Wintzer, and B. Fuerniss. Kraftstoff, Strom und Waerme aus Stroh und Waldrestholz - eine systemanalytische Untersuchung. *Technikfolgenabschaetzung - Theorie und Praxis*, 15(1):61–72, 2006.

[13] E. Henrich, N. Dahmen, K. Raffelt, R. Stahl, and F. Weirich. The Karlsruhe "bioliq" process for biomass gasification. In *2nd European Summer School on Renewable Motor Fuels*, 2007.

[14] E. Henrich, N. Dahmen, and E. Dinjus. Cost estimate for biosynfuel production via biosyncrude gasification. *Biofuels, Bioproducts and Biorefining*, 3:28–41, 2009.

[15] N. Dahmen, E. Dinjus, and E. Henrich. Das Karlsruher bioliq-Verfahren - Stand und Entwicklung. In *Mobil mit Biomasse*, 2006.

[16] Y. Wang and L. Yan. CFD studies on biomass thermochemical conversion. *Int. J. Mol. Sci.*, 9:1108–1130, 2008.

[17] T. Norton, D. W. Sun, J. Grant, R. Fallon, and V. Dodda. Applications of computational fluid dynamics (CFD) in the modelling and design of ventilation systems in the agricultural industry: A review. *Bioresource Technology*, 98 (12):2386 – 2414, 2007.

[18] T. F. Dixon, A. P. Mann, F. Plaza, and W. N. Gilfillan. Development of advanced technology for biomass combustion - CFD as an essential tool. *Fuel*, 84 (10):1303–1311, 2005.

[19] H. A. J. A. van Kuijk, R. J. M. Bastiaans, J. A. Van Oijen, and L. P. H. De Goey. Modelling NOx-formation for application in a biomass combustion furnace. In *Proceedings of the European Combustion Meeting*, 2005.

[20] D. F. Fletcher, B. S. Haynes, F. C. Christo, and S. D. Joseph. A CFD based combustion model of an entrained flow biomass gasifier. *Applied Mathematical Modelling*, 24(3):165–182, 2000.

[21] A. K. Sharma. Modeling fluid and heat transport in the reactive, porous bed of downdraft (biomass) gasifier. *International Journal of Heat and Fluid Flow*, 28:1518–1530, 2007.

[22] U. Santo, D. Kuhn, H. J. Wiemer, E. Pantouflas, N. Zarzalis, H. Seifert, and T. Kolb. Erzeugung von Synthesegas aus biomassestaemmigen Slurries im Flugstromvergaser. *Chemie Ingenieur Technik*, 79 No.5:651–656, 2007.

[23] J. Warnatz, U. Mass, and R.W. Dibble. *Combustion*. Heidelberg: Springer Verlag, 2006.

[24] J. F. Douglas, J. M. Gasiorek, and J. A. Swaffield. *Fluid Mechanics*. Longman Scientific and Technical, 1995.

[25] J. Piquet. *Turbulent Flows - Models and Physics*. Springer Verlag, 1999.

[26] *ANSYS FLUENT 12.0 Theory Guide 2009*.

[27] N. Peters. *Turbulent Combustion*. Cambridge University Press, 2000.

[28] D. Veynante and L. Vervisch. *Turbulent Combustion Modelling*. Von Karman Institute, 1999.

[29] J. O. Hinze. *Turbulence*. McGraw-Hill Publishing Company, 1975.

[30] D. C. Wilcox. *Turbulence modeling for CFD*. DCW Industries, 1998.

[31] B. E. Launder and D. B. Spalding. *Lectures in mathematical models of turbulence*. Academic Press, 1972.

[32] T. H. Shih, W. W. Liou, A. Shabbir, Z. Yang, and J. Zhu. A new k-ε eddy viscosity model for high Reynolds number turbulent flows. *Computers Fluids*, 24(3):227–238, 1995.

[33] R. Siegel and J. R. Howell. *Thermal Radiation Heat Transfer*. Hemisphere Publishing Corporation, 1992.

[34] J. Liu, H. M. Shang, and Y. S. Chen. Development of an unstructured radiation model applicable for two-dimensional planar, axisymmetric, and three-dimensional geometries. *Journal of Quantitative Spectroscopy and Radiative Transfer*, 66:17–33, 2000.

[35] A. G. Ratzel. *P-N Differential Approximation for Solution of One and Two Dimensional Radiation and Conduction Energy Transfer in Gray Participating Media*. PhD thesis, University of Texas, 1981.

[36] J. R. Howell and M. Perlmutter. Monte Carlo solution of thermal transfer through radiant media between gray walls. *J. Heat Transfer*, 86:116–122, 1964.

[37] N. G. Shah. *A new Method of Computation of Radiant Heat Transfer in Combustion Chambers*. PhD thesis, Imperial College of Science and Technology, London, 1979.

[38] E. P. Keramida, H. H. Liakos, M. A. Founti, A. G. Boudouvis, and N. C. Markatos. The discrete transfer radiation model in a natural gas fired furnace. *Int. J. Numer. Meth. Fluids*, 34:449–462, 2000.

[39] W. A. Fiveland. Three dimensional radiative heat transfer solutions by the discrete ordinate method. *J. Thermophys. Heat Transfer*, 2:309–316, 1988.

[40] W. A. Fiveland. Discrete ordinate methods for radiative heat transfer in isotropically and anisotropically scattering media. *Journal of Heat Transfer*, 109:807–812, 1987.

[41] D. Joseph, P. J. Coelho, B. Cuenot, and M. El Hafi. Application of the discrete ordinates method to grey media in complex geometries using unstructured meshes. In *Proceedings of Eurotherm73 on Computational Thermal Radiation in Participating Media*, 2003.

[42] B. R. Adams and P. J. Smith. Three dimensional discrete ordinates modelling of radiative transfer in a geometrically complex furnace. *Combustion Science and Technology*, 88:293–308, 1993.

[43] A. S. Jamaluddin and P. J. Smith. Predicting radiative transfer in axisymmetric cylindrical enclosures using the discrete ordinates method. *Combustion Science and Technology*, 62:173 – 186, 1988.

[44] C. B. Ludwig, W. Malkmus, J. G. Reardon, and J. A. Thomson. *Handbook of Infrared Radiation from Combustion Gases*. NASA SP-3080, 1973.

[45] T. F. Smith, Z. F. Shen, and J. N. Friedman. Evaluation of coefficients for the weighted sum of gray gases model. *J. Heat Transfer*, 104:602–608, 1982.

[46] M. F. Modest. The weighted-sum-of-gray-gases model for arbitrary solution methods in radiative transfer. *J. Heat Transfer*, 113:650–656, 1991.

[47] M. Chrigui. *Eulerian-Lagrangian Approach for Modeling and Simulations of Turbulent Reactive Multi-Phase Flows under Gas Turbine Combustor Conditions*. PhD thesis, Technische Universitaet Darmstadt, 2005.

[48] M. Chrigui, A. Sadiki, J. Janicka, and M. Maneshkarimi. CFD analysis of conjugate effects of turbulence and swirl intensity on spray combustion in a single gas turbine combustor. In *ASME TURBO EXPO*, 2004.

[49] S. B. Pope. PDF methods for turbulent reactive flows. *Prog. Energy Combust. Sci.*, 11:119–192, 1985.

[50] H. W. Ge. *Probability Density Function Modeling of Turbulent Non-reactive and Reactive Spray Flows.* PhD thesis, Heidelberg University, 2006.

[51] S. A. Morsi and J. A. Alexander. An investigation of particle trajectories in two-phase flow systems. *J. Fluid Mech.*, 55(2):193–208, 1972.

[52] Z. F. Tian, J. Y. Tu, and G. H. Yeoh. Numerical simulation and validation of dilute gas-particle flow over a backward-facing step. *Aerosol Science and Technology*, 39:319–332, 2005.

[53] W.E. Ranz and W.J. Marshall. Evaporation from drops, part I. *Chem. Eng. Prog.*, 48:141–146, 1952.

[54] W. E. Ranz and W. J. Marshall. Evaporation from drops, part II. *Chem. Eng. Prog.*, 48:173–180, 1952.

[55] S. Elgobashi. Particle-laden turbulent flows: direct simulation and closure models. *Applied Scientific Research*, 48:301–314, 1991.

[56] R. K. Boyd and J. H. Kent. Three-dimensional furnace computer modelling. In *21st. Symposium (International) on Combustion, The Combustion Institute*, 1986.

[57] A. Burcat. *Combustion Chemistry*, chapter Thermochemical Data for Combustion. Springer Verlag, 1984.

[58] R. J. Kee, F. M. Rupley, and J. A. Miller. Chemical thermodynamic data base. Technical report, Sandia Report 87-82153, 1987.

[59] S. Arrhenius. Ueber die Reaktionsgeschwindigkeit bei der Inversion von Rohrzucker durch Saeuren. *Z Phys. Chem.*, 4:226, 1889.

[60] R. G. Gilbert, K. Luther, and J. Troe. Theory of thermal unimolecular reactions in the fall-off range. *Ber. Bunsenges. Phys. Chem.*, 87:169 – 177, 1983.

[61] J. Troe. Predictive possibilities of unimolecular rate theory. *J. Phys. Chem.*, 83:114 – 126, 1979.

[62] P. W. Atkins and J. De Paula. *Physical Chemistry*. Oxford University Press, 2006.

[63] P. Zhang and C. K. Law. A fitting formula for the falloff curves of unimolecular reactions. *International Journal of Chemical Kinetics*, 41:727–734, 2009.

[64] S. Hafner. *Modellentwicklung zur numerischen Simulation eines Flugstromvergasers fuer Biomasse*. PhD thesis, Heidelberg University, 2010.

[65] C. Heghes. *C1 - C4 Hydrocarbon Oxidation Mechanism*. PhD thesis, Heidelberg University, 2006.

[66] S. Hafner, A. Rashidi, G. Baldea, and U. Riedel. A detailed chemical kinetic model of high temperature ethylene glycol gasification. *Combustion Theory and Modelling*, In Press, 2010.

[67] U. Maas. *Mathematische Modellierung instationaerer Verbrennungsprozesse unter Verwendung detaillierter Reaktionsmechanismen*. PhD thesis, Heidelberg University, 1988.

[68] L. R. Petzold. A description of DASSL: A differential/algebraic system solver. Technical report, Sandia National Laboratories, SAND82-8637, 1982.

[69] P. Deuflhard, E. Hairer, and J. Zugck. One step and extrapolation methods for differential-algebraic systems. *Numer. Math.*, 51:501 – 516, 1987.

[70] J. Warnatz. Calculation of the structure of laminar flat flames I: Flame velocity of freely propagating ozone decomposition flames. *Ber. Bunsenges. Phys. Chem.*, 82:193 – 200, 1978.

[71] P. A. Libby and F. A. Williams. *Topics in Applied Physics: Turbulent Reacting Flows*. Springer Verlag, 1980.

[72] R. O. Fox. *Computational Models for Turbulent Reacting Flows*. Cambridge University Press, 2003.

[73] N. Peters. Fifteen lectures on laminar and turbulent combustion. In *Ercoftac Summer School*, 1992.

[74] E. S. Bish and W. J. A. Dahm. Strained dissipation and reaction layer analysis for non-equilibrium chemistry in turbulent reacting flows. *Combustion and Flame*, 100:457, 1995.

[75] N. Peters. Laminar diffusion flamelet models in non-premixed turbulent combustion. *Prog. Energy Combust. Sci.*, 10:319–339, 1984.

[76] J. S. Kim and F. A. Williams. Extinction of diffusion flames with nonunity Lewis numbers. *Journal of Engineering Mathematics*, 31:101–118, 1997.

[77] H. Pitsch, M. Chen, and N. Peters. Unsteady flamelet modelling of turbulent hydrogen-air diffusion flames. In *27th Symposium on Combustion, The Combustion Institute*, 1998.

[78] C. M. Muller, H. Breitbach, and N. Peters. Partially premixed turbulent flame propagation in jet flames. In *25th Symposium (Int) on Combustion, The Combustion Institute*, 1994.

[79] B. F. Magnussen. On the structure of turbulence and a generalized eddy dissipation concept for chemical reaction in turbulent flow. In *19th AIAA Meeting*, 1981.

[80] B. F. Magnussen and B. H. Hjertager. On mathematical models of turbulent combustion with special emphasis on soot formation and combustion. In *16th Symp. (International) on Combustion. The Combustion Institute*, 1976.

[81] I. R. Gran and B. F. Magnussen. A numerical study of a bluff-body stabilized diffusion flame. part 2. influence of combustion modeling and finite-rate chemistry. *Combustion Science and Technology*, 119:191–217, 1996.

[82] M. T. Landahl and E. Mollo-Christensen. *Turbulence and Random Processes in Fluid Mechanics*. Cambridge University Press, 1992.

[83] B. F. Magnussen. Modeling of pollutant formation in gas turbine combustors based on the eddy dissipation concept. In *18th International Congress on Combustion Engines*, 1989.

[84] W. J. Minkowycz, E. M. Sparrow, and J. Y. Murthy, editors. *Handbook of Numerical Heat Transfer*. John Wiley and Sons, 2006.

[85] T. J. Chung. *Computational Fluid Dynamics*. Cambridge University Press, 2002.

[86] J. N. Reddy. *An introduction to Finite Element Method*. Mc-Graw-Hill, 1993.

[87] P. Wesseling. *Principles of Computational Fluid Dynamics*. Springer Verlag, 2000.

[88] A. J. Chorin. Numerical solution of navier-stokes equations. *Mathematics of Computation*, 22:745–762, 1968.

[89] M. H. Kobayashia, J. M. C. Pereira, and J. C. F. Pereira. A conservative finite-volume second-order-accurate projection method on hybrid unstructured grids. *Journal of Computational Physics*, 150:40–75, 1999.

[90] A. S. Almgren, J. B. Bell, P. Colella, L. H. Howell, and M. L. Welcome. A conservative adaptive projection method for the variable density incompressible Navier-Stokes equations. *Journal of Computational Physics*, 142:1–46, 1998.

[91] J. B. Bell, P. Colella, and H. M. Glaz. A second-order projection method for the incompressible Navier-Stokes equations. *Journal of Computational Physics*, 85:257–283, 1989.

[92] S. R. Mathur and J. Y. Murthy. A pressure-based method for unstructured meshes. *Numerical Heat Transfer, Part B: Fundamentals*, 31:195 – 215, 1997.

[93] B. R. Hutchinson and G. D. Raithby. A multigrid method based on additive correction strategy. *Numer. Heat Transfer*, 9:511–537, 1986.

[94] W. Hackbusch. *Multi-Grid Methods and Applications*. Springer Verlag, 1985.

[95] S. V. Patankar. *Numerical Heat Transfer and Fluid Flow*. Hemisphere Publishing Corporation, 1980.

[96] C. M. Rhie and W. L. Chow. Numerical study of the turbulent flow past an airfoil with trailing edge separation. *AIAA Journal*, 21:1525–1532, 1983.

[97] S. B. Pope. Computationally efficient implementation of combustion chemistry using in situ adaptive tabulation. *Combust. Theory Modelling*, 1:41–63, 1997.

[98] J. J. Shah and R. O. Fox. Computational fluid dynamics simulation of chemical reactors: Application of in situ adaptive tabulation to methane thermochlorination chemistry. *Ind. Eng. Chem. Res.*, 38:4200–4212, 1999.

[99] T. Kolb, T. Jakobs, and N. Zarzalis. Syngas from biomass-based slurry entrained-flow gasification. In *10th Conference on Energy for a Clean Environment*, 2009.

[100] H. J. Wiemer, D. Kuhn, U. Santo, M. Eberhard, T. Kolb, E. Pantouflas, and N. Zarzalis. Thermochemische Umsetzung von Matrixfluessigkeit in

einem Flugstromvergaser bei der Variation des Luftbedarfs. In *VDI-GET-Fachtagung Verbrennung und Feuerung-23. Deutscher Flammentag, vol. VDI-Bericht*, 2007.

[101] Personal correspondances with KIT, 2007-2009.

[102] W. Sutherland. LII. the viscosity of gases and molecular force. *Philosophical Magazine*, Series 5 , 36:507 – 531, 1893.

[103] Crane. Flow of fluids through valves, fittings and pipe. Technical report, No. 410M, Crane Co., 1988.

[104] A. Rashidi, M. Eberhard, and U. Riedel. CFD simulation of gasification process with ethylene glycol as model substance for biomass based pyrolysis oil. *International Journal of Energy for a Clean Environment*, 2010.

[105] A. Bennardo, F. Podenzani, and L. Borello. A flare case : comparison of the results of two CFD codes with experimental data. In *10th Conference on Energy for a Clean Environment*, 2009.

[106] P. Mathieu and R. Dubuisson. Performance analysis of a biomass gasifier. *Energy Conversion and Management*, 43:1291–1299, 2002.

[107] H. R. Weir. High pressure gasification of coal in Germany. *Industrial and Engineering Chemistry*, 39:48–54, 1947.

[108] R. P. Bell. The theory of reactions involving proton transfers. *Proceedings of the Royal Society of London. Series A, Mathematical and Physical Sciences*, 154:414–429, 1936.

[109] M. G. Evans and M. Polanyi. Inertial and driving force of chemical reactions. *Transactions of Faraday Society*, 34:11–24, 1938.

[110] T. Poinsot and D. Veynante. *Theoretical and Numerical Combustion*. Edwards, 2005.

[111] F. Tabet-Helal, B. Sarh, M. Birouk, and I. Goekalp. Numerical investigation of the near-field region of a turbulent non-premixed (CH4-H2-N2)/air flame. In *Proceedings of 3rd European Combustion Meeting*, 2007.

[112] K. Claramunt Altimira. *Numerical Simulation of Non-Premixed Laminar and Turbulent Flames by means of Flamelet Modelling Approaches*. PhD thesis, Universitat Politecnica Catalunya, 2005.

[113] F. Liu, H. Guo, and G. J. Smallwood. Evaluation of the laminar diffusion flamelet model in the calculation of an axisymmetric coflow laminar ethylene-air diffusion flame. *Combustion and Flame*, 144:605–618, 2006.

[114] B. A. Albrecht, S. Zahirovic, R. J. M. Bastiaans, J. A. van Oijen, and L. P. H. de Goey. A premixed flamelet-PDF model for biomass combustion in a grate furnace. *Energy and Fuels*, 22:1570–1580, 2008.

[115] F. Tabet-Helal, B. Sarh, and I. Goekalp. A comparative study of turbulence modelling in diluted hydrogen non-premixed flames. *IFRF Industrial Combustion*, Nr. 200803:1–41, 2008.

A. Appendices

A.1 Nomenclature

a	Strain Rate
a	Absorption Coefficient
a_{p}	Equivalent Absorption Coefficient of Particles
A	Pre-exponential Factor in Arrhenius Formula
A	Surface Area
A_{pn}	Projected Area of Particle n
b	Temperature Exponent in Arrhenius Formula
c_i	Concentration of Species i
c_{p}	Specific Heat Capacity at Constant Pressure
$C_{1\varepsilon}$, $C_{2\varepsilon}$	Constants of Standard k-ε Model
C_1 , C_2	Constants of Realizable k-ε Model
C_i	Vapor Concentration
C_{D}	Drag Coefficient
d	Distance Between Jet Nozzles
d_{p}	Particle Diameter
D	Diffusivity
$D_{i,\mathrm{m}}$	Mass Diffusion Coefficient
$D_{\mathrm{T},i}$	Thermal Diffusion Coefficient
E	Total Energy
E_{a}	Activation Energy
E_{p}	Equivalent Particle Emission
f	Mixture Fraction
f_{pn}	Scattering Factor of Particle n

F	Lorentzian Broadening Factor
$\vec{F}$	Force Vector
F_{D}	Drag Force
$\vec{g}$	Gravitational Acceleration
G	Incident Radiation
G_{k}	Production of Turbulent Kinetic Energy
h	Species Enthalpy
h	Convective Heat Transfer Coefficient
h_{fg}	Latent Heat of Evaporation
H	Total Enthalpy
H_{lat}	Latent Heat at Boiling Point
$H_{\mathrm{lat,ref}}$	Latent Heat at Reference Condition
I	Radiation Intensity
$\vec{J}_i$	Diffusion Flux
k	Turbulent Kinetic Energy
k_{c}	Mass Transfer Coefficient
k_{f} , k_{r}	Rate Constant for Forward / Reverse Reactions
k_{∞}	Thermal Conductivity of Continuous Phase
K_{c}	Equilibrium Constant
L_{e}	Eddy Length Scale
Le	Lewis Number
LHV	Lower Heating Value
m	Mass
$\dot{m}$	Mass Flow Rate
$M_{\mathrm{w},i}$	Molecular Weight of Species i
$n_{i,\mathrm{f}}$, $n_{i,\mathrm{r}}$	Reaction Orders of Forward / Reverse Reactions
N	Number of Chemical Species
N_i	Flux of Droplet Vapor into Gas Phase
Nu	Nusselt Number
p	Pressure
p_0	Atmospheric Pressure
p_{sat}	Saturated Vapor Pressure
Pr	Prandtl Number
Q_{rad}	Radiative Heat Flux
R	Universal Gas Constant
Re	Reynolds Number
Re_{ij}	Reynolds Stresses

$\vec{s}$	Direction (Radiation)
S	Source Term
S_{ij}	Mean Rate-of-Strain Tensor
Sc_{t}	Turbulent Schmidt Number
Sh	Sherwood Number
t	Time
t_{cross}	Particle Eddy Crossing Time
T	Temperature
T_{bp}	Boiling Temperature
T_{vap}	Evaporation Temperature
T_{w}	Gasifier Wall Temperature
u_i	Velocity Magnitude
u_{p}	Particle Velocity
$\vec{v}$	Overall Velocity Vector
V	Volume
w_{char}	Char Mass Fraction in Slurry
x_i	Direction
X_i	Mole Fraction of Species i
Y_i	Mass Fraction of Species i
Y_i^*	Fine Scale Mass Fraction of Species i
Z_i	Mass Fraction of Element i
α	Bell-Evans-Polanyi Factor
δ	Delta Function
ϵ	Total Emissivity
ϵ_{pn}	Emissivity of Particle n
ε	Turbulent Dissipation Rate
ζ	Normally Distributed Random Number
η	Mean Strain
η_{G}	Gasification Efficiency
η_{k}	Kolmogorov Length Scale
θ_{R}	Radiation Temperature
λ	Air-Fuel Ratio
λ	Thermal Conductivity
λ_{eff}	Effective Thermal Conductivity
λ_{t}	Turbulent Thermal Conductivity
μ	Dynamic Viscosity

μ_t	Turbulent Viscosity
ν	Kinematic Viscosity
ν' , ν''	Stoichiometric Coefficient for Reactants, Products
ξ^*	Length Fraction of Fine Structures
ρ	Density
ρ_∞	Density of the Oxidizer Stream
σ	Stefan-Boltzmann Constant
σ_k , σ_ε	k and ε Prandtl Number
σ_p	Equivalent Particle Scattering Coefficient
σ_s	Scattering Coefficient
τ	Time Scale
τ^*	Time Scale of Fine Structures
$\bar{\tau}$	Stress Tensor
χ	Scalar Dissipation Rate
ω_k	Angular Velocity
ΔH_j^0	Enthalpy of Reaction j
ΔS_j^0	Entropy of Reaction j
Δt	Time Step
Φ	Phase Function
Ω'	Solid Angle
$\overline{\Omega_{ij}}$	Mean Rate-of-Rotation Tensor

A.2 Reaction Mechanism

The reaction mechanism for high temperature oxidation of ethylene glycol, used in this thesis, is based on the chemical reaction mechanism developed by Hafner [64]. The original mechanism is simplified using the methods discussed in Chapter 4.

The reaction rates are defined in modified Arrhenius form (Equation 4.8) $k_\mathrm{f} = AT^b \cdot e^{\left(-\frac{E_\mathrm{a}}{RT}\right)}$. The units of the pre-exponential factor A and activation energy E_a are $(\mathrm{cm^3 mol^{-1}})^{\mathrm{n-1}}\mathrm{s^{-1}}$ and kJ/mol, respectively. The rate coefficients of reverse reactions are calculated as discussed in Chapter 4.

The collision efficiencies used are as follows:

M(1) = $[H_2]$ + 6,5$[H_2O]$ + 0,4$[O_2]$ + 0,35[AR] + 0,4$[N_2]$ + 0,75[CO] + 1,5$[CO_2]$ + 3,0[EthGly]
M(2) = $[H_2]$ + 2,55$[H_2O]$ + 0,4$[O_2]$ + 0,15[AR] + 0,4$[N_2]$ + 0,75[CO] + 1,5$[CO_2]$ + 3,0[EthGly]
M(3) = $[H_2]$ + 6,5$[H_2O]$ + 0,4$[O_2]$ + 0,29[AR] + 0,4$[N_2]$ + 0,75[CO] + 1,5$[CO_2]$ + 3,0[EthGly]
M(4) = 2,0$[H_2]$ + 5,0$[H_2O]$ + 2,0[CO] + 3,0$[CO_2]$ + 3,0[EthGly].

#											A	b	E_a
HCOOH Reactions													
1	HCOOH	+	M(1)	→	H_2O	+	CO	+	M(1)		$2.090\cdot10^{14}$	0.0	169.026
2	HCOOH	+	M(1)	→	H_2	+	CO_2	+	M(1)		$1.350\cdot10^{15}$	0.0	253.54
3	HCOOH	+	OH	→	CO_2	+	H_2O	+	H		$2.620\cdot10^{06}$	2.056	3.832
4	HCOOH	+	OH	→	CO	+	H_2O	+	OH		$1.850\cdot10^{07}$	1.5	−4.025
5	HCOOH	+	H	→	CO_2	+	H_2	+	H		$4.240\cdot10^{06}$	2.1	20.367
6	HCOOH	+	H	→	CO	+	H_2	+	OH		$6.060\cdot10^{13}$	−0.35	12.501
7	HCOOH	+	CH_3	→	CO	+	CH_4	+	OH		$3.90\cdot10^{-07}$	5.80	9.204
8	HCOOH	+	HO_2	→	CO	+	H_2O_2	+	OH		$2.40\cdot10^{19}$	−2.20	58.699
9	HCOOH	+	O	→	CO	+	OH	+	OH		$1.770\cdot10^{18}$	−1.90	12.447
CHOCHO Reactions													
10	CHO	+	CHO	⇌	CHOCHO						$1.00\cdot10^{13}$	0.0	0.0
12	CHOCHO			→	CO	+	CO	+	H_2		$4.070\cdot10^{42}$	−8.5	289.847
13	CHOCHO	+	OH	→	CHO	+	CO	+	H_2O		$1.00\cdot10^{13}$	0.0	0.0
14	CHOCHO	+	O	→	CHO	+	CO	+	OH		$7.240\cdot10^{12}$	0.0	8.242
15	CHOCHO	+	H	⇌	CH_2O	+	CHO				$1.00\cdot10^{12}$	0.0	0.0
17	CHOCHO	+	M(4)	⇌	CHO	+	CHO	+	M(4)		$4.270\cdot10^{12}$	0.0	211.72
19	CHOCHO	+	HO_2	→	CHO	+	CO	+	H_2O_2		$1.70\cdot10^{12}$	0.0	44.767
20	CHOCHO	+	CH_3	→	CHO	+	CO	+	CH_4		$1.740\cdot10^{12}$	0.0	35.311
21	CHOCHO	+	O_2	→	CHO	+	CO	+	HO_2		$1.00\cdot10^{14}$	0.0	154.801
HOCHCO Reactions													
22	HOCHCO	+	H	⇌	CH_2OH	+	CO				$2.710\cdot10^{04}$	2.750	4.03

24	HOCHCO	+	O	⇌	HCOOH	+	CO			$3.613 \cdot 10^{11}$	0.0	6.98
26	HOCHCO	+	OH	⇌	CH_2OH	+	CO_2			$6.239 \cdot 10^{11}$	0.0	5.6
28	HOCHCO	+	OH	⇌	HCOOH	+	CHO			$0.337 \cdot 10^{11}$	0.0	4.19
30	HCOOH	+	CH	⇌	HOCHCO	+	H			$9.460 \cdot 10^{13}$	0.0	−2.1
32	HOCHCO	+	M(1)	⇌	CH_2O	+	CO	+	M(1)	$3.00 \cdot 10^{14}$	0.00	298.51
									LOW	$3.60 \cdot 10^{15}$	0.00	249.48
									TROE	0.50	0.0	0.0	0.0
34	HOCHCO	+	O_2	⇌	CO_2	+	HCOOH			$1.00 \cdot 10^{08}$	0.0	−0.05

HOCHCHO Reactions

36	HOCHCHO	+	H	⇌	HOCHCO	+	H_2			$2.00 \cdot 10^{13}$	0.0	3.19
38	HOCHCHO	+	OH	⇌	HOCHCO	+	H_2O			$3.00 \cdot 10^{13}$	0.0	3.19
40	$HOCH_2CHO$+		O_2	⇌	HOCHCHO	+	HO_2			$2.00 \cdot 10^{13}$	0.0	217.79
42	HOCHCHO	+	H	⇌	CHOCHO	+	H_2			$3.00 \cdot 10^{13}$	0.0	8.1
44	HOCHCHO	+	OH	⇌	CHOCHO	+	H_2O			$1.510 \cdot 10^{13}$	0.0	8.1
46	HOCHCHO	+	O_2	⇌	CHOCHO	+	HO_2			$8.430 \cdot 10^{15}$	−1.2	8.1
48	HOCHCHO	+	O_2	⇌	CHOCHO	+	HO_2			$4.820 \cdot 10^{14}$	0.0	28.2
50	HOCHCHO	+	M(4)	⇌	CHOCHO	+	H	+	M(4)	$1.00 \cdot 10^{14}$	0.0	112.77
52	HOCHCHO	+	O	⇌	CHOCHO	+	OH			$1.00 \cdot 10^{14}$	0.0	8.1
54	HOCHCHO	+	H	⇌	$HOCH_2CO$	+	H			$5.00 \cdot 10^{12}$	0.0	1.34
56	HOCHCHO	+	H	⇌	CHO	+	CH_2OH			$5.00 \cdot 10^{13}$	0.0	4.23
58	HOCHCHO			⇌	CO	+	CH_2OH			$1.170 \cdot 10^{43}$	−9.83	187.31
60	HOCHCO	+	M(1) + H	⇌	HOCHCHO	+	M(1)			$3.30 \cdot 10^{14}$	−0.06	32.38
62	HOCHCHO	+	O	⇌	HOCHCO	+	OH			$2.00 \cdot 10^{13}$	0.0	19.93

$HOCH_2CO$ Reactions

64	$HOCH_2CO$	+	H	⇌	HOCHCO	+	H_2			$2.580 \cdot 10^{07}$	1.65	4.95
66	$HOCH_2CO$	+	OH	⇌	HOCHCO	+	H_2O			$4.640 \cdot 10^{11}$	0.15	−6.88
68	$HOCH_2CO$	+	O	⇌	HOCHCO	+	OH			$1.880 \cdot 10^{07}$	1.85	0.75
70	$HOCH_2CO$	+	HO_2	⇌	HOCHCO	+	H_2O_2			$8.20 \cdot 10^{03}$	2.55	38.1
72	$HOCH_2CO$	+	CH_3	⇌	HOCHCO	+	CH_4			$7.280 \cdot 10^{02}$	2.99	26.38
74	C_3H_5OH	+	O	⇌	CH_3	+	$HOCH_2CO$			$5.00 \cdot 10^{12}$	0.0	0.12
76	$HOCH_2CO$	+	H	⇌	CHO	+	CH_2OH			$9.60 \cdot 10^{13}$	0.0	−4.87
78	$HOCH_2CO$	+	O	⇌	CO_2	+	CH_2OH			$1.50 \cdot 10^{14}$	0.0	−4.87
80	$HOCH_2CO$	+	HO_2	→	CO_2 + CH_2OH			+	OH	$3.00 \cdot 10^{13}$	0.0	−4.87
81	$HOCH_2CO$	+	OH	→	CO + CH_2OH			+	OH	$3.00 \cdot 10^{13}$	0.0	−4.87
82	CH_2OH	+	CO+M(1)	⇌	$HOCH_2CO$	+	M(1)			$5.058 \cdot 10^{11}$	0.00	25.89
									LOW	$3.109 \cdot 10^{14}$	0.00	13.5
									TROE	0.50	0.0	0.0	0.0

$HOCH_2CHO$ Reactions

84	$HOCH_2CHO$+		M(1)	⇌	CH_2OH	+	CHO	+	M(1)	$2.20 \cdot 10^{15}$	0.0	348.04
									LOW	$5.10 \cdot 10^{12}$	0.0	136.64
									TROE	0.50	0.0	0.0	0.0
86	$HOCH_2CHO$+		H	⇌	$HOCH_2CO$	+	H_2			$2.047 \cdot 10^{09}$	1.16	12.41

88	$HOCH_2CHO+$	H	$\rightleftharpoons$	HOCHCHO +	H_2	$2.580 \cdot 10^{07}$	1.65	8.01
90	$HOCH_2CHO+$	O	$\rightleftharpoons$	$HOCH_2CO$ +	OH	$1.770 \cdot 10^{18}$	−1.90	14.81
92	$HOCH_2CHO+$	O	$\rightleftharpoons$	HOCHCHO +	OH	$1.880 \cdot 10^{07}$	1.85	3.81
94	$HOCH_2CHO+$	OH	$\rightleftharpoons$	$HOCH_2CO$ +	H_2O	$9.240 \cdot 10^{06}$	1.50	−1.68
96	$HOCH_2CHO+$	OH	$\rightleftharpoons$	HOCHCHO +	H_2O	$4.640 \cdot 10^{11}$	0.15	−3.82
98	$HOCH_2CHO+$	OH	$\rightleftharpoons$	CH_2OH +	HCOOH	$3.00 \cdot 10^{15}$	−1.076	5.24
100	$HOCH_2CHO+$	O_2	$\rightleftharpoons$	$HOCH_2CO$ +	HO_2	$2.00 \cdot 10^{13}$	0.50	175.63
102	$HOCH_2CHO+$	HO_2	$\rightleftharpoons$	$HOCH_2CO$ +	H_2O_2	$2.40 \cdot 10^{19}$	−2.20	61.09
104	$HOCH_2CHO+$	HO_2	$\rightleftharpoons$	HOCHCHO +	H_2O_2	$8.20 \cdot 10^{03}$	2.55	41.16
106	$HOCH_2CHO+$	CH_3	$\rightleftharpoons$	$HOCH_2CO$ +	CH_4	$3.90 \cdot 10^{-07}$	5.80	11.56
108	$HOCH_2CHO+$	CH_3	$\rightleftharpoons$	HOCHCHO +	CH_4	$7.280 \cdot 10^{02}$	2.99	29.44
110	CH_2CH_2OH +	O_2	$\rightleftharpoons$	$HOCH_2CHO+$	OH	$4.90 \cdot 10^{11}$	−0.48	30.13
112	$HOCH_2CO$ +	H + M	$\rightleftharpoons$	$HOCH_2CHO+$	M	$9.60 \cdot 10^{13}$	0.00	−2.35
114	$HOCH_2CHO+$	CHO	$\rightleftharpoons$	$HOCH_2CO$ +	CH_2O	$7.80 \cdot 10^{13}$	0.00	37.67

R−CHOH Reactions

116	R−CHOH +	M	$\rightleftharpoons$	$HOCH_2CHO+$	H +	M	$1.00 \cdot 10^{14}$	0.0	106.68
118	R−CHOH +	H	$\rightleftharpoons$	$HOCH_2CHO+$	H_2		$3.00 \cdot 10^{13}$	0.0	2.01
120	R−CHOH +	H	$\rightleftharpoons$	CH_2OH +	CH_2OH		$3.00 \cdot 10^{13}$	0.0	7.25
122	R−CHOH +	O	$\rightleftharpoons$	$HOCH_2CHO+$	OH		$1.00 \cdot 10^{14}$	0.0	2.01
124	R−CHOH +	OH	$\rightleftharpoons$	$HOCH_2CHO+$	H_2O		$1.510 \cdot 10^{13}$	0.0	2.01
126	R−CHOH +	O_2	$\rightleftharpoons$	$HOCH_2CHO+$	HO_2		$8.432 \cdot 10^{15}$	−1.2	2.01
128	R−CHOH +	O_2	$\rightleftharpoons$	$HOCH_2CHO+$	HO_2		$4.820 \cdot 10^{14}$	0.0	22.11
130	R−CHOH +	HO_2	$\rightleftharpoons$	$HOCH_2CHO+$	OH +	OH	$4.00 \cdot 10^{13}$	0.0	2.01

R−CH_2O Reactions

132	$R-CH_2O$		$\rightleftharpoons$	$HOCH_2CHO+$	H		$2.00 \cdot 10^{14}$	0.0	99.58
134	$R-CH_2O$		$\rightleftharpoons$	CH_2O +	CH_2OH		$1.50 \cdot 10^{15}$	0.0	97.78
136	$R-CH_2O$ +	H	$\rightleftharpoons$	$HOCH_2CHO+$	H_2		$1.00 \cdot 10^{14}$	0.0	2.58
138	$R-CH_2O$ +	H	$\rightleftharpoons$	CH_2OH +	CH_2OH		$3.00 \cdot 10^{13}$	0.0	7.82
140	$R-CH_2O$ +	O	$\rightleftharpoons$	$HOCH_2CHO+$	OH		$1.210 \cdot 10^{14}$	0.0	2.58
142	$R-CH_2O$ +	OH	$\rightleftharpoons$	$HOCH_2CHO+$	H_2O		$1.00 \cdot 10^{14}$	0.0	2.58
144	$R-CH_2O$ +	O_2	$\rightleftharpoons$	$HOCH_2CHO+$	HO_2		$6.00 \cdot 10^{10}$	0.0	9.58
146	$R-CH_2O$ +	CO	$\rightleftharpoons$	CH_2CH_2OH +	CO_2		$4.680 \cdot 10^{02}$	3.16	29.95

EthGly Reactions

148	EthGly +	M(4)	$\rightleftharpoons$	CH_2OH + CH_2OH	+	M(4)	$5.94 \cdot 10^{23}$	−1.68	390.66
						LOW	$3.11 \cdot 10^{85}$	−18.84	482.21
						TROE	0.50	550.0	825.0 6100.0
150	EthGly +	M(4)	$\rightleftharpoons$	CH_2CH_2OH +	OH +	M(4)	$2.50 \cdot 10^{23}$	−1.54	410.55
						LOW	$6.50 \cdot 10^{85}$	−18.81	489.79
						TROE	0.50	300.0	900.0 5000.0
152	EthGly +	M(4)	$\rightleftharpoons$	CH_3CHO +	H_2O +	M(4)	$3.720 \cdot 10^{13}$	0.09	281.99
						LOW	$3.43 \cdot 10^{83}$	−18.85	367.05
						TROE	0.70	350.0	800.0 3800.0

154	EthGly	+	M(4)	⇌	$HOCH_2CHO$	+	H_2	+	M(4)	$1.448 \cdot 10^{12}$	0.10	381.03
									LOW	$8.92 \cdot 10^{87}$	−19.42	493.56
									TROE	0.90	900.0	1100.0	3500.0
156	EthGly	+	H	⇌	R−CHOH	+	H_2			$5.160 \cdot 10^{07}$	1.65	13.56
158	EthGly	+	H	⇌	$R-CH_2O$	+	H_2			$3.00 \cdot 10^{07}$	1.6	13.87
160	EthGly	+	O	⇌	R−CHOH	+	OH			$3.760 \cdot 10^{07}$	1.85	9.36
162	EthGly	+	O	⇌	$R-CH_2O$	+	OH			$3.160 \cdot 10^{07}$	2.0	19.77
164	EthGly	+	OH	⇌	R−CHOH	+	H_2O			$9.280 \cdot 10^{11}$	0.15	1.73
166	EthGly	+	OH	⇌	$R-CH_2O$	+	H_2O			$1.492 \cdot 10^{12}$	0.30	8.0
168	EthGly	+	HO_2	⇌	R−CHOH	+	H_2O_2			$1.640 \cdot 10^{04}$	2.55	46.71
170	EthGly	+	HO_2	⇌	$R-CH_2O$	+	H_2O_2			$5.00 \cdot 10^{12}$	0.0	101.58
172	EthGly	+	CH_3	⇌	R−CHOH	+	CH_4			$1.456 \cdot 10^{03}$	2.99	34.99
174	EthGly	+	CH_3	⇌	$R-CH_2O$	+	CH_4			$2.90 \cdot 10^{02}$	2.99	33.16

Oxyhydrogen and CO/CO_2 System

H_2/O_2 Reactions

176	O_2	+	H	⇌	OH	+	O			$2.650 \cdot 10^{16}$	-0.67	71.3
178	H_2	+	O	⇌	OH	+	H			$3.818 \cdot 10^{12}$	0.0	33.256
180	H_2	+	O	⇌	OH	+	H			$1.025 \cdot 10^{15}$	0.0	80.230
182	H_2	+	OH	⇌	H_2O	+	H			$2.168 \cdot 10^{08}$	1.520	14.466
184	OH	+	OH	⇌	H_2O	+	O			$3.348 \cdot 10^{04}$	2.420	-8.064
186	H	+	H	+	M(1)	⇌	H_2	+	M(1)	$1.015 \cdot 10^{17}$	-0.60	0.0
188	O	+	O	+	M(1)	⇌	O_2	+	M(1)	$5.40 \cdot 10^{13}$	0.0	-7.4
190	H	+	OH	+	M(2)	⇌	H_2O	+	M(2)	$5.560 \cdot 10^{22}$	-2.0	0.0

HO_2Reactions

192	H	+	O_2	+	M(3)	⇌	HO_2	+	M(3)	$1.746 \cdot 10^{17}$	0.0	0.0
									LOW	$2.367 \cdot 10^{19}$	-1.20	0.0
									TROE	0.5	0.0	0.0	0.0
194	HO_2	+	H	⇌	OH	+	OH			$4.457 \cdot 10^{14}$	0.0	5.819
196	HO_2	+	H	⇌	H_2	+	O_2			$1.054 \cdot 10^{14}$	0.0	8.563
198	HO_2	+	H	⇌	H_2O	+	O			$1.445 \cdot 10^{12}$	0.0	0.0
200	HO_2	+	O	⇌	OH	+	O_2			$1.626 \cdot 10^{13}$	0.0	-1.862
202	HO_2	+	OH	⇌	H_2O	+	O_2			$9.275 \cdot 10^{15}$	0.0	73.246

H_2O_2Reactions

204	HO_2	+	HO_2	⇌	H_2O_2	+	O_2			$4.220 \cdot 10^{14}$	0.0	50.140
206	HO_2	+	HO_2	⇌	H_2O_2	+	O_2			$1.325 \cdot 10^{11}$	0.0	-6.820
208	OH	+	OH	+	M(1)	⇌	H_2O_2	+	M(1)	$1.566 \cdot 10^{13}$	0.0	0.0
									LOW	$5.980 \cdot 10^{19}$	-0.8	0.0
									TROE	0.50	0.0	0.0	0.0
210	H_2O_2	+	H	⇌	H_2	+	HO_2			$1.686 \cdot 10^{12}$	0.0	15.713
212	H_2O_2	+	H	⇌	H_2O	+	OH			$1.024 \cdot 10^{13}$	0.0	14.970
214	H_2O_2	+	O	⇌	OH	+	HO_2			$4.216 \cdot 10^{11}$	0.0	16.628

216	H_2O_2	+	O	$\rightleftharpoons$	H_2O	+	O_2			$4.216 \cdot 10^{11}$	0.0	16.628
218	H_2O_2	+	OH	$\rightleftharpoons$	H_2O	+	HO_2			$1.64 \cdot 10^{18}$	0.0	123.047
220	H_2O_2	+	OH	$\rightleftharpoons$	H_2O	+	HO_2			$1.92 \cdot 10^{12}$	0.0	1.787

CO Reactions

222	CO	+	O	+	M(1)	$\rightleftharpoons$	CO_2	+	M(1)	$1.540 \cdot 10^{15}$	0.0	12.560
224	CO	+	OH	$\rightleftharpoons$	CO_2	+	H			$1.05 \cdot 10^{13}$	0.0	66.927
226	CO	+	OH	$\rightleftharpoons$	CO_2	+	H			$9.034 \cdot 10^{11}$	0.0	19.120
228	CO	+	OH	$\rightleftharpoons$	CO_2	+	H			$1.012 \cdot 10^{11}$	0.0	0.249
230	CO	+	HO_2	$\rightleftharpoons$	CO_2	+	OH			$1.50 \cdot 10^{14}$	0.0	98.70
232	CO	+	O_2	$\rightleftharpoons$	CO_2	+	O			$2.50 \cdot 10^{12}$	0.0	200.0

C_1 Oxidation

C Reactions

234	CH	+	H	$\rightleftharpoons$	C	+	H_2			$5.0 \cdot 10^{14}$	0.0	0.0
236	C	+	O_2	$\rightleftharpoons$	CO	+	O			$6.023 \cdot 10^{13}$	0.0	2.66

CH Reactions

238	CH	+	O	$\rightleftharpoons$	CO	+	H			$4.0 \cdot 10^{13}$	0.0	0.0
240	CH	+	OH	$\rightleftharpoons$	CHO	+	H			$3.0 \cdot 10^{13}$	0.0	0.0
242	CH	+	O_2	$\rightleftharpoons$	CHO	+	O			$1.686 \cdot 10^{13}$	0.0	0.0
244	CH	+	CO	+	M(2)	$\rightleftharpoons$	HCCO	+	M(2)	$1.024 \cdot 10^{15}$	-0.4	0.0
									LOW	$3.790 \cdot 10^{00}$	-2.5	0.0
									TROE	0.60 0.0	0.0	0.0
246	CH	+	CO_2	$\rightleftharpoons$	CHO	+	CO			$6.384 \cdot 10^{07}$	1.51	-2.993
248	CH	+	H_2O	$\rightleftharpoons$	CH_2O	+	H			$4.577 \cdot 10^{16}$	-1.42	0.0
250	CH	+	H_2O	$\rightleftharpoons$	$^3CH_2$	+	OH			$4.577 \cdot 10^{16}$	-1.42	0.0

CHO Reactions

252	CHO	+	M(1)	$\rightleftharpoons$	CO	+	H	+	M(1)	$1.860 \cdot 10^{17}$	-1.0	71.13
254	CHO	+	H	$\rightleftharpoons$	CO	+	H_2			$9.034 \cdot 10^{13}$	0.0	0.0
256	CHO	+	O	$\rightleftharpoons$	CO	+	OH			$3.011 \cdot 10^{13}$	0.0	0.0
258	CHO	+	O	$\rightleftharpoons$	CO_2	+	H			$3.011 \cdot 10^{13}$	0.0	0.0
260	CHO	+	OH	$\rightleftharpoons$	CO	+	H_2O			$1.084 \cdot 10^{14}$	0.0	0.0
262	CHO	+	O_2	$\rightleftharpoons$	CO	+	HO_2			$2.710 \cdot 10^{10}$	0.68	-1.962
264	CHO	+	CHO	$\rightleftharpoons$	CH_2O	+	CO			$3.0 \cdot 10^{13}$	0.0	0.0
266	CHO	+	HO_2	$\rightarrow$	CO_2	+	H	+	OH	$3.0 \cdot 10^{13}$	0.0	0.0
267	CHO	+	O_2	$\rightleftharpoons$	CO_2	+	OH			$1.510 \cdot 10^{12}$	0.0	0.0

CH_2 Reactions

269	$^3CH_2$	+	H	$\rightleftharpoons$	CH	+	H_2			$1.204 \cdot 10^{14}$	0.0	0.0
271	$^3CH_2$	+	O	$\rightarrow$	CO	+	H	+	H	$1.228 \cdot 10^{14}$	0.0	2.244
272	$^3CH_2$	+	O	$\rightleftharpoons$	CO	+	H_2			$8.191 \cdot 10^{13}$	0.0	2.244
274	$^3CH_2$	+	O_2	$\rightleftharpoons$	CO	+	OH	+	H	$1.806 \cdot 10^{12}$	0.0	0.0

276	$^3CH_2$	+	O_2	⇌	CO_2	+	H_2			$1.806 \cdot 10^{12}$	0.0	0.0
278	$^3CH_2$	+	$^3CH_2$	⇌	C_2H_2	+	H_2			$1.806 \cdot 10^{14}$	0.0	49.884
280	$^3CH_2$	+	$^3CH_2$	⇌	C_2H_2	+	H	+	H	$1.626 \cdot 10^{15}$	0.0	49.884
282	$^3CH_2$	+	CH_3	⇌	C_2H_4	+	H			$7.227 \cdot 10^{13}$	0.0	0.0
284	$^1CH_2$	+	M(1)	⇌	$^3CH_2$	+	M(1)			$6.023 \cdot 10^{12}$	0.0	0.0
286	$^1CH_2$	+	H_2	⇌	CH_3	+	H			$1.260 \cdot 10^{16}$	-0.56	66.5
288	$^1CH_2$	+	O_2	⇌	CO	+	OH	+	H	$3.10 \cdot 10^{13}$	0.0	0.0
290	$^3CH_2$	+	OH	⇌	H	+	CH_2O			$2.50 \cdot 10^{13}$	0.0	0.0
292	$^3CH_2$	+	CO_2	⇌	CO	+	CH_2O			$1.10 \cdot 10^{11}$	0.0	4.184
294	$^3CH_2$	+	O_2	⇌	O	+	CH_2O			$3.290 \cdot 10^{21}$	-3.3	11.999
296	$^3CH_2$	+	O_2	→	CO_2	+	H	+	H	$3.290 \cdot 10^{21}$	-3.3	11.999
297	$^3CH_2$	+	O_2	⇌	CO	+	H_2O			$7.280 \cdot 10^{19}$	-2.54	7.569
299	$^3CH_2$	+	O_2	⇌	CHO	+	OH			$1.290 \cdot 10^{20}$	-3.3	1.188
301	$^1CH_2$	+	CH_4	⇌	CH_3	+	CH_3			$4.0 \cdot 10^{13}$	0.0	0.0
303	$^1CH_2$	+	C_2H_6	⇌	CH_3	+	C_2H_5			$1.20 \cdot 10^{14}$	0.0	0.0
305	$^1CH_2$	+	O	→	CO	+	H	+	H	$3.0 \cdot 10^{13}$	0.0	0.0
306	$^1CH_2$	+	OH	⇌	CH_2O	+	H			$3.0 \cdot 10^{13}$	0.0	0.0
308	$^1CH_2$	+	H	⇌	CH	+	H_2			$3.0 \cdot 10^{13}$	0.0	0.0
310	$^1CH_2$	+	CO_2	⇌	CH_2O	+	CO			$3.0 \cdot 10^{12}$	0.0	0.0
312	$^1CH_2$	+	CH_2CO	⇌	C_2H_4	+	CO			$1.60 \cdot 10^{14}$	0.0	0.0

CH_2O Reactions

314	CH_2O	+	M(1)	⇌	CHO	+	H	+	M(1)	$4.872 \cdot 10^{15}$	0.0	316.348
316	CH_2O	+	M(1)	⇌	CO	+	H_2	+	M(1)	$2.830 \cdot 10^{15}$	0.0	266.962
318	CH_2O	+	H	⇌	CHO	+	H_2			$2.190 \cdot 10^{08}$	1.77	12.560
320	CH_2O	+	O	⇌	CHO	+	OH			$4.155 \cdot 10^{11}$	0.57	11.556
322	CH_2O	+	OH	⇌	CHO	+	H_2O			$7.20 \cdot 10^{05}$	2.46	-4.06
324	CH_2O	+	HO_2	⇌	CHO	+	H_2O_2			$4.095 \cdot 10^{04}$	2.5	42.734
326	CH_2O	+	O_2	⇌	CHO	+	HO_2			$2.439 \cdot 10^{05}$	2.5	152.562
328	CH_2O	+	CH_3	⇌	CHO	+	CH_4			$3.192 \cdot 10^{01}$	3.36	18.041
330	CH_2O	+	CH	⇌	CH_2CO	+	H			$9.460 \cdot 10^{13}$	0.0	-2.155

CH_2OH Reactions

332	CH_2OH	+	M(1)	⇌	CH_2O	+	H	+	M(1)	$2.80 \cdot 10^{14}$	-0.73	137.306
									LOW	$1.50 \cdot 10^{34}$	-5.39	151.456
									TROE	0.96 67.2	1855.0	7543.0
334	CH_2OH	+	H	⇌	CH_2O	+	H_2			$2.445 \cdot 10^{13}$	0.0	0.0
336	CH_2OH	+	H	⇌	CH_3	+	OH			$1.048 \cdot 10^{13}$	0.0	0.0
338	CH_2OH	+	O_2	⇌	CH_2O	+	HO_2			$2.891 \cdot 10^{16}$	-1.5	0.0
340	CH_2OH	+	O_2	⇌	CH_2O	+	HO_2			$7.230 \cdot 10^{13}$	0.0	14.97

CH_3 Reactions

342	CH_3	+	M(1)	⇌	$^3CH_2$	+	H	+	M(1)	$2.922 \cdot 10^{16}$	0.0	379.0
344	CH_3	+	M(1)	⇌	CH	+	H_2	+	M(1)	$1.892 \cdot 10^{16}$	0.0	355.839
346	CH_3	+	O	⇌	CH_2O	+	H			$6.745 \cdot 10^{13}$	0.0	0.0

348	CH_3	+	OH	→	CH_3O	+	H			$1.204 \cdot 10^{10}$	0.0	58.114
349	CH_3	+	OH	⇌	$^1CH_2$	+	H_2O			$3.0 \cdot 10^{13}$	0.0	11.640
351	CH_3	+	OH	+	M(1)	⇌	CH_3OH	+	M(1)	$4.336 \cdot 10^{15}$	-0.79	0.0
									LOW	$1.098 \cdot 10^{38}$	-6.21	5.578
									TROE	0.25	210	1434.0	0.0
353	CH_3	+	HO_2	⇌	CH_3O	+	OH			$1.80 \cdot 10^{13}$	0.0	0.0
355	CH_3	+	O_2	→	O	+	CH_3O			$4.20 \cdot 10^{13}$	0.0	135.851
356	CH_3	+	CO	+	M(1)	⇌	CH_3CO	+	M(1)	$5.058 \cdot 10^{11}$	0.0	28.77
									LOW	$3.109 \cdot 10^{14}$	0.0	15.88
									TROE	0.50	0.0	0.0	0.0
358	CH_3	+	$^1CH_2$	⇌	C_2H_4	+	H			$7.227 \cdot 10^{13}$	0.0	0.0
360	CH_3	+	CH_3	+	M(1)	⇌	C_2H_6	+	M(1)	$3.613 \cdot 10^{13}$	0.0	0.0
									LOW	$3.627 \cdot 10^{41}$	-7.0	11.60
									TROE	0.62	73.0	1180.0	0.0
362	CH_3	+	O_2	⇌	CH_2O	+	OH			$2.510 \cdot 10^{11}$	0.0	61.295
364	CH_3	+	CH	⇌	C_2H_3	+	H			$3.0 \cdot 10^{13}$	0.0	0.0

CH_3O Reactions

366	CH_3O	+	M(1)	⇌	CH_2O	+	H	+	M(1)	$6.80 \cdot 10^{13}$	0.0	109.49
									LOW	$4.660 \cdot 10^{25}$	-3.0	101.68
									TROE	0.45	0.0	0.0	0.0
368	CH_3O	+	H	→	CH_3	+	OH			$1.626 \cdot 10^{13}$	0.0	2.494
369	CH_3O	+	H	⇌	CH_2O	+	H_2			$3.794 \cdot 10^{13}$	0.0	2.494
371	CH_3O	+	O	→	O_2	+	CH_3			$1.129 \cdot 10^{13}$	0.0	0.0
372	CH_3O	+	O	⇌	OH	+	CH_2O			$3.764 \cdot 10^{12}$	0.0	0.0
374	CH_3O	+	OH	⇌	CH_2O	+	H_2O			$1.810 \cdot 10^{13}$	0.0	0.0
376	CH_3O	+	O_2	⇌	CH_2O	+	HO_2			$2.168 \cdot 10^{10}$	0.0	7.3
378	CH_3O	+	CH_2O	⇌	CH_3OH	+	CHO			$1.150 \cdot 10^{11}$	0.0	5.2
380	CH_3O	+	CO	⇌	CH_3	+	CO_2			$4.680 \cdot 10^{02}$	3.16	22.525

CH_4 Reactions

382	CH_4	+	M(1)	⇌	CH_3	+	H	+	M(1)	$2.80 \cdot 10^{16}$	0.0	439.0
									LOW	$5.50 \cdot 10^{47}$	-8.2	492.180
									TROE	0.0	1350	1.0	7834.0
384	CH_4	+	H	⇌	H_2	+	CH_3			$4.143 \cdot 10^{05}$	2.5	40.115
386	CH_4	+	O	⇌	OH	+	CH_3			$4.396 \cdot 10^{05}$	2.5	27.519
388	CH_4	+	OH	⇌	H_2O	+	CH_3			$1.050 \cdot 10^{06}$	2.18	11.223
390	CH_4	+	HO_2	⇌	H_2O_2	+	CH_3			$4.697 \cdot 10^{04}$	2.5	87.879
392	CH_4	+	CH	⇌	C_2H_4	+	H			$1.325 \cdot 10^{16}$	-0.94	0.241
394	CH_3	+	HO_2	⇌	CH_4	+	O_2			$3.0 \cdot 10^{12}$	0.0	0.0
396	CH_4	+	$^3CH_2$	⇌	CH_3	+	CH_3			$4.0 \cdot 10^{13}$	0.0	0.0

CH_3OH Reactions

398	CH_3OH	+	H	⇌	CH_2OH	+	H_2			$2.746 \cdot 10^{09}$	1.24	18.789
400	CH_3OH	+	H	⇌	CH_3O	+	H_2			$6.866 \cdot 10^{08}$	1.24	18.789

402	CH_3OH	+	O	$\rightleftharpoons$	CH_2OH	+	OH			$1.975 \cdot 10^{13}$	0.0	22.198
404	CH_3OH	+	O	$\rightleftharpoons$	CH_3O	+	OH			$4.938 \cdot 10^{12}$	0.0	22.198
406	CH_3OH	+	OH	$\rightleftharpoons$	CH_2OH	+	H_2O			$5.273 \cdot 10^{06}$	1.92	-1.197
408	CH_3OH	+	OH	$\rightleftharpoons$	CH_3O	+	H_2O			$0.930 \cdot 10^{06}$	1.92	-1.197
410	CH_3OH	+	HO_2	$\rightleftharpoons$	CH_2OH	+	H_2O_2			$0.620 \cdot 10^{13}$	0.0	81.10
412	CH_3OH	+	O_2	$\rightleftharpoons$	HO_2	+	CH_2OH			$2.050 \cdot 10^{13}$	0.0	189.10
414	CH_3OH	+	CH_3	$\rightleftharpoons$	CH_4	+	CH_2OH			$9.937 \cdot 10^{00}$	3.45	33.422
416	CH_3OH	+	CH_3	$\rightleftharpoons$	CH_4	+	CH_3O			$2.017 \cdot 10^{01}$	3.45	33.422
418	CH_3OH	+	CH_3O	$\rightleftharpoons$	CH_2OH	+	CH_3OH			$1.50 \cdot 10^{12}$	0.0	29.30
420	CH_3OH	+	CH_2O	$\rightarrow$	CH_3O	+	CH_3O			$0.153 \cdot 10^{13}$	0.0	333.20

C_2 Oxidation

HCCO Reactions

421	HCCO	+	H	$\rightleftharpoons$	$^3CH_2$	+	CO			$1.060 \cdot 10^{13}$	0.0	0.0
423	HCCO	+	O	$\rightleftharpoons$	CO	+	CO	+	H	$1.250 \cdot 10^{14}$	0.0	0.0
425	HCCO	+	$^3CH_2$	$\rightleftharpoons$	C_2H_3	+	CO			$3.0 \cdot 10^{13}$	0.0	0.0
427	HCCO	+	O_2	$\rightleftharpoons$	CO_2	+	CHO			$2.40 \cdot 10^{11}$	0.0	-3.576
429	HCCO	+	O	$\rightleftharpoons$	CO_2	+	CH			$2.950 \cdot 10^{13}$	0.0	4.66

C_2H_2 Reactions

431	C_2H_2	+	O	$\rightleftharpoons$	$^3CH_2$	+	CO			$1.10 \cdot 10^{08}$	1.4	9.228
433	C_2H_2	+	O	$\rightleftharpoons$	HCCO	+	H			$7.0 \cdot 10^{08}$	1.4	9.228
435	C_2H_2	+	O_2	$\rightleftharpoons$	HCCO	+	OH			$4.0 \cdot 10^{07}$	1.5	126.0
437	C_2H_2	+	OH	$\rightleftharpoons$	CH_2CO	+	H			$2.18 \cdot 10^{-04}$	4.50	-4.187
439	C_2H_2	+	OH	$\rightleftharpoons$	CH_2CO	+	H			$2.0 \cdot 10^{11}$	0.0	0.0

CH_2CO Reactions

441	CH_2CO	+	M(1)	$\rightleftharpoons$	$^3CH_2$	+	CO	+	M(1)	$3.0 \cdot 10^{14}$	0.0	297.179
									LOW	$3.60 \cdot 10^{15}$	0.0	248.152
									TROE	0.50 0.0	0.0	0.0
443	CH_2CO	+	H	$\rightleftharpoons$	CH_3	+	CO			$2.710 \cdot 10^{04}$	2.750	2.989
445	CH_2CO	+	O	$\rightleftharpoons$	CH_2O	+	CO			$3.613 \cdot 10^{11}$	0.0	5.653
447	CH_2CO	+	O	$\rightarrow$	CHO	+	H	+	CO	$1.806 \cdot 10^{11}$	0.0	5.653
448	CH_2CO	+	O	$\rightleftharpoons$	CHO	+	CHO			$1.806 \cdot 10^{11}$	0.0	5.653
450	CH_2CO	+	OH	$\rightleftharpoons$	CH_3	+	CO_2			$6.239 \cdot 10^{11}$	0.0	4.240
452	CH_2CO	+	OH	$\rightleftharpoons$	CH_2O	+	CHO			$0.337 \cdot 10^{11}$	0.0	4.240
454	CH_2CO	+	O	$\rightleftharpoons$	$^3CH_2$	+	CO_2			$1.750 \cdot 10^{12}$	0.0	5.648
456	CH_2CO	+	H	$\rightleftharpoons$	HCCO	+	H_2			$2.0 \cdot 10^{14}$	0.0	33.471
458	CH_2CO	+	O	$\rightleftharpoons$	HCCO	+	OH			$1.0 \cdot 10^{13}$	0.0	33.471
460	CH_2CO	+	OH	$\rightleftharpoons$	HCCO	+	H_2O			$1.0 \cdot 10^{13}$	0.0	8.368
462	CH_2CO	+	OH	$\rightleftharpoons$	CH_2OH	+	CO			$3.730 \cdot 10^{12}$	0.0	-4.238
464	CH_2CO	+	O_2	$\rightleftharpoons$	CO_2	+	CH_2O			$1.0 \cdot 10^{08}$	0.0	0.0

C_2H_3 Reactions

466	C_2H_3	+	M(1)	⇌	C_2H_2	+	H	+ M(1)	$7.80 \cdot 10^{08}$	1.62	155.056
								LOW	$3.237 \cdot 10^{27}$	-3.40	149.818
								TROE	0.35 0.0	0.0	0.0
468	C_2H_3	+	H	⇌	C_2H_2	+	H_2		$4.216 \cdot 10^{13}$	0.0	0.0
470	C_2H_3	+	O	⇌	C_2H_2	+	OH		$3.011 \cdot 10^{13}$	0.0	0.0
472	C_2H_3	+	O	⇌	CH_3	+	CO		$3.011 \cdot 10^{13}$	0.0	0.0
474	C_2H_3	+	O	⇌	CHO	+	$^3CH_2$		$3.011 \cdot 10^{13}$	0.0	0.0
476	C_2H_3	+	OH	⇌	C_2H_2	+	H_2O		$5.0 \cdot 10^{12}$	0.0	0.0
478	C_2H_3	+	O_2	⇌	CH_2O	+	CHO		$9.0 \cdot 10^{12}$	0.0	-0.997
480	C_2H_3	+	O_2	⇌	C_2H_2	+	HO_2		$4.650 \cdot 10^{11}$	0.0	-1.039
482	C_2H_3	+	O_2	⇌	CH_2CHO	+	O		$5.50 \cdot 10^{14}$	-0.61	22.023
484	C_2H_3	+	O	⇌	CH_2CO	+	H		$3.0 \cdot 10^{13}$	0.0	0.0

CH_3CO Reactions

486	CH_3CO	+	H	⇌	CH_2CO	+	H_2		$2.0 \cdot 10^{13}$	0.0	0.0
488	CH_3CO	+	H	⇌	CHO	+	CH_3		$9.60 \cdot 10^{13}$	0.0	0.0
490	CH_3CO	+	O	⇌	CO_2	+	CH_3		$1.50 \cdot 10^{14}$	0.0	0.0
492	CH_3CO	+	HO_2	→	CO_2	+	CH_3	+ OH	$3.0 \cdot 10^{13}$	0.0	0.0
493	CH_3CO	+	OH	→	CO	+	CH_3	+ OH	$3.0 \cdot 10^{13}$	0.0	0.0
494	CH_3CO	+	OH	⇌	CH_2CO	+	H_2O		$1.20 \cdot 10^{13}$	0.0	0.0
496	CH_3CO	+	O	⇌	CH_2CO	+	OH		$2.0 \cdot 10^{13}$	0.0	0.0
498	CH_3CO	+	CH_3	⇌	CH_2CO	+	CH_4		$5.0 \cdot 10^{13}$	0.0	0.0

CH_2CHO Reactions

500	CH_2CHO	+	H	⇌	CH_2CO	+	H_2		$2.0 \cdot 10^{13}$	0.0	0.0
502	CH_2CHO	+	H	⇌	CH_3CO	+	H		$5.0 \cdot 10^{12}$	0.0	0.0
504	CH_2CHO	+	H	⇌	CHO	+	CH_3		$5.0 \cdot 10^{13}$	0.0	0.0
506	CH_2CHO	+	OH	⇌	CHO	+	CH_2OH		$3.010 \cdot 10^{13}$	0.0	0.0
508	CH_2CHO	+	O	⇌	CHO	+	CH_2O		$1.0 \cdot 10^{14}$	0.0	0.0
510	CH_2CHO	+	CH	⇌	CHO	+	C_2H_3		$1.0 \cdot 10^{14}$	0.0	0.0
512	CH_2CHO			⇌	CO	+	CH_3		$1.170 \cdot 10^{43}$	-9.83	183.08
514	CH_2CO + M(1) + H			⇌	CH_2CHO	+	M(1)		$3.30 \cdot 10^{14}$	-0.06	35.57
516	CH_2CHO	+	O	⇌	CH_2CO	+	OH		$2.0 \cdot 10^{13}$	0.0	16.74
518	CH_2CHO	+	OH	⇌	CH_2CO	+	H_2O		$3.0 \cdot 10^{13}$	0.0	0.0
520	CH_2CHO	+	HO_2	→	CH_2O	+	OH	+ CHO	$7.0 \cdot 10^{12}$	0.0	0.0

C_2H_4 Reactions

521	C_2H_4	+	M(1)	⇌	C_2H_2	+	H_2	+ M(1)	$4.50 \cdot 10^{17}$	1.0	327.488
523	C_2H_4	+	M(1)	⇌	C_2H_3	+	H	+ M(1)	$7.399 \cdot 10^{17}$	0.0	404.060
525	C_2H_4	+	H	+	M(1)	→	C_2H_5	+ M(1)	$3.975 \cdot 10^{09}$	1.280	5.40
								LOW	$1.178 \cdot 10^{19}$	0.0	3.20
								TROE	0.76 40.0	1025	0.0
526	C_2H_4	+	H	⇌	C_2H_3	+	H_2		$4.0 \cdot 10^{02}$	3.62	47.140
528	C_2H_4	+	O	⇌	CH_2CHO	+	H		$4.743 \cdot 10^{06}$	1.88	0.764

530	C_2H_4	+	O	⇌	CHO	+	CH_3			$1.020 \cdot 10^{07}$	1.88	0.764
532	C_2H_4	+	O	⇌	CH_2CO	+	H_2			$6.770 \cdot 10^{05}$	1.88	0.764
534	C_2H_4	+	OH	⇌	C_2H_3	+	H_2O			$1.070 \cdot 10^{13}$	0.0	24.9
536	C_2H_4	+	$^1CH_2$	⇌	C_3H_6					$7.240 \cdot 10^{13}$	0.0	0.0
538	C_2H_4	+	CH_3	⇌	C_2H_3	+	CH_4			$6.023 \cdot 10^{07}$	1.56	69.60

CH_3CHO Reactions

540	CH_3CHO	+	M(1)	⇌	CH_3	+	CHO	+	M(1)	$2.20 \cdot 10^{15}$	0.0	342.8
									LOW	$5.10 \cdot 10^{12}$	0.0	131.4
									TROE	0.50 0.0	0.0	0.0
542	CH_3CHO	+	H	⇌	CH_3CO	+	H_2			$2.047 \cdot 10^{09}$	1.16	10.059
544	CH_3CHO	+	H	⇌	CH_2CHO	+	H_2			$1.70 \cdot 10^{09}$	1.16	10.059
546	CH_3CHO	+	OH	⇌	CH_3CO	+	H_2O			$9.240 \cdot 10^{06}$	1.50	-4.028
548	CH_3CHO	+	OH	⇌	CH_2CHO	+	H_2O			$2.023 \cdot 10^{07}$	1.35	-6.584
550	CH_3CHO	+	OH	⇌	CH_3	+	HCOOH			$3.70 \cdot 10^{15}$	-1.076	0.0
552	CH_3CHO	+	O	⇌	CH_3CO	+	OH			$1.770 \cdot 10^{18}$	-1.90	12.456
554	CH_3CHO	+	O	⇌	CH_2CHO	+	OH			$3.720 \cdot 10^{13}$	-0.20	14.888
556	CH_3CHO	+	CH_3	⇌	CH_3CO	+	CH_4			$3.90 \cdot 10^{-07}$	5.80	9.211
558	CH_3CHO	+	CH_3	⇌	CH_2CHO	+	CH_4			$2.450 \cdot 10^{01}$	3.150	23.978
560	CH_3CHO	+	HO_2	⇌	CH_3CO	+	H_2O_2			$2.40 \cdot 10^{19}$	-2.20	58.741
562	CH_3CHO	+	HO_2	⇌	CH_2CHO	+	H_2O_2			$2.320 \cdot 10^{11}$	0.40	62.233
564	CH_3CHO	+	O_2	⇌	CH_3CO	+	HO_2			$2.0 \cdot 10^{13}$	0.50	173.28
566	C_2H_5	+	O_2	⇌	CH_3CHO	+	OH			$4.90 \cdot 10^{11}$	-0.480	34.989
568	CH_2CHO	+	HO_2	⇌	CH_3CHO	+	O_2			$3.0 \cdot 10^{12}$	0.0	0.0
570	CH_3CO	+	H + M	⇌	CH_3CHO	+	M			$9.60 \cdot 10^{13}$	0.0	0.0
572	CH_3CHO	+	CHO	⇌	CH_3CO	+	CH_2O			$7.80 \cdot 10^{13}$	0.0	35.315

C_2H_5 Reactions

574	C_2H_5	+	M(1)	→	C_2H_4	+	H	+	M(1)	$4.10 \cdot 10^{13}$	0.0	166.80
									LOW	$3.654 \cdot 10^{18}$	0.0	139.68
									TROE	0.75 97.0 1379 0.0		
575	C_2H_5	+	H	⇌	CH_3	+	CH_3			$1.0 \cdot 10^{14}$	0.0	0.0
577	C_2H_5	+	O	⇌	CH_2O	+	CH_3			$3.975 \cdot 10^{13}$	0.0	0.0
579	C_2H_5	+	O_2	⇌	C_2H_4	+	HO_2			$2.410 \cdot 10^{10}$	0.0	0.0
581	C_2H_5	+	CH_3	⇌	C_2H_4	+	CH_4			$9.034 \cdot 10^{11}$	0.0	0.0
583	C_2H_5	+	C_2H_5	⇌	C_2H_4	+	C_2H_6			$1.40 \cdot 10^{12}$	0.0	0.0
585	C_2H_5	+	H	⇌	C_2H_4	+	H_2			$1.250 \cdot 10^{14}$	0.0	33.471
587	C_2H_5	+	H	⇌	C_2H_6					$3.0 \cdot 10^{13}$	0.0	0.0
589	C_2H_5	+	OH	⇌	C_2H_4	+	H_2O			$4.0 \cdot 10^{13}$	0.0	0.0
591	C_2H_5	+	HO_2	→	CH_3	+	CH_2O	+	OH	$3.0 \cdot 10^{13}$	0.0	0.0

CH_2CH_2OH Reactions

592	CH_2CH_2OH			⇌	C_2H_4	+	OH			$1.0 \cdot 10^{14}$	0.0	140.0
594	CH_2CH_2OH	+	H	⇌	CH_3CHO	+	H_2			$5.0 \cdot 10^{13}$	0.0	0.0

C_2H_6 Reactions

596	C_2H_6	+	H	$\rightleftharpoons$	C_2H_5	+	H_2		$5.540 \cdot 10^{02}$	3.5	21.62
598	C_2H_6	+	O	$\rightleftharpoons$	C_2H_5	+	OH		$1.0 \cdot 10^{09}$	1.5	24.4
600	C_2H_6	+	OH	$\rightleftharpoons$	C_2H_5	+	H_2O		$9.154 \cdot 10^{06}$	2.0	4.157
602	C_2H_6	+	HO_2	$\rightleftharpoons$	C_2H_5	+	H_2O_2		$1.102 \cdot 10^{05}$	2.5	70.502
604	C_2H_6	+	O_2	$\rightleftharpoons$	C_2H_5	+	HO_2		$7.287 \cdot 10^{05}$	2.5	205.688
606	C_2H_6	+	$^3CH_2$	$\rightleftharpoons$	C_2H_5	+	CH_3		$2.20 \cdot 10^{13}$	0.0	36.3
608	C_2H_6	+	CH_3	$\rightleftharpoons$	C_2H_5	+	CH_4		$5.601 \cdot 10^{10}$	0.0	39.408
610	C_2H_6	+	CH_3	$\rightleftharpoons$	C_2H_5	+	CH_4		$8.432 \cdot 10^{14}$	0.0	93.116
612	C_2H_6	+	CH	$\rightleftharpoons$	C_2H_4	+	CH_3		$1.084 \cdot 10^{14}$	0.0	-1.1
614	C_2H_6	+	M(1)	$\rightleftharpoons$	C_2H_5	+	H	+ M(1)	$8.850 \cdot 10^{20}$	-1.22	427.62
								LOW	$6.920 \cdot 10^{42}$	-6.43	448.55
								TROE	0.50 0.0	0.0	0.0

C_3 Oxidation

C_3H_6 Reactions

616	C_3H_6			$\rightleftharpoons$	C_2H_3	+	CH_3	$3.10 \cdot 10^{21}$	-1.2	408.8
618	C_3H_6	+	O	$\rightleftharpoons$	C_2H_4	+	CH_2O	$5.90 \cdot 10^{13}$	0.0	21.0
620	C_3H_6	+	O	$\rightleftharpoons$	C_2H_5	+	CHO	$3.60 \cdot 10^{12}$	0.0	0.0
622	C_3H_6	+	O	$\rightleftharpoons$	CH_3	+	CH_3CO	$5.0 \cdot 10^{12}$	0.0	2.5
624	C_3H_6	+	OH	$\rightleftharpoons$	C_2H_5	+	CH_2O	$7.90 \cdot 10^{12}$	0.0	0.0
626	C_3H_6	+	OH	$\rightleftharpoons$	CH_3	+	CH_3CHO	$5.10 \cdot 10^{12}$	0.0	0.0
628	C_3H_6	+	H	$\rightleftharpoons$	C_2H_4	+	CH_3	$7.230 \cdot 10^{11}$	0.7	5.447